Adaptive blind restoration for monochrome and hyperspectral images

Fabio El Samrani

COLLEGE DOCTORAL BRETAGNE

MATHS, TELECOMS
INFORMATIQUE, SIGNAL
SYSTEMES, ELECTRONIQUE

Université de Rennes

THESE DE DOCTORAT DE

L'UNIVERSITE DE RENNES 1

ECOLE DOCTORALE N° 601
Mathématiques, Télécommunications, Informatique, Signal, Systèmes, Electronique

Par
Fabio EL SAMRANI

Adaptive blind restoration for monochrome and hyperspectral images

Thèse présentée et soutenue à l'Université de Rennes le 12 Décembre 2023

Unité de recherche : Institut d'Électronique et de Télécommunications de Rennes (UMR CNRS 6164)

Rapporteurs avant soutenance :

Serge REBOUL	Professeur, Université du Littoral Côte d'Opale
Anissa MOKRAOUI	Professeur, Université Sorbonne Paris Nord

Composition du Jury :

Président :	Fabrice MERIAUDEAU	Professeur, Université de Bourgogne
Examinateurs :	Serge REBOUL	Professeur, Université du Littoral Côte d'Opale
	Anissa MOKRAOUI	Professeur, Université Sorbonne Paris Nord
	Aurélia FRAYSSE	Maître de conférences HDR, CentraleSupélec Paris
	Aziz BELMILOUDI	Maître de conférences HDR, INSA Rennes
	Benoit VOZEL	Maître de conférences, Université de Rennes
Dir. de thèse :	Kacem CHEHDI	Professor, Université de Rennes

Table des matières

Acknowledgement

This thesis manuscript signifies three years of dedicated work at the University of Rennes, in collaboration with the Institute of Electronics and Digital Technologies (IETR) and funded by the Doctoral school MATISSE. The accomplishment of this doctoral work would not have been possible without the support of numerous individuals whose generosity and interest were evident in my research.

My sincere appreciation to my thesis director Prof. Kacem CHEHDI for his unwavering support, effective mentorship, and the qualities of patience, rigor, availability, and good humor that guided me throughout this thesis. Your guidance has been essential for the progress of my research.

I thank the entire team "Multicomponent and Multimodal Signal & Image Processing" for welcoming me during the preparation of this thesis, particularly Benoit VOZEL and Josias LEFEVRE for their valuable discussions and advice.

Special thanks go to my friends Simona FAHIM, Tony RACHED, Gabriel EL HACHACH, and Ghady MOUSSA, who shared challenging moments and provided constant support. Your encouragement has been invaluable.

Lastly, I express my deepest gratitude to my family, especially my father Elie and my mother Nisrine, for their persistence and constant support, serving as a continual source of motivation.

Used notations

In this section, we represent the notations used throughout this thesis:

$\boldsymbol{g}$: observed monochrome image formed of $M \times N$ pixels

$\boldsymbol{f}$: original image

$\boldsymbol{PSF}$: Point Spread Function

$\boldsymbol{HSI}$: Hyperspectral image formed of $M \times N$ pixels $\times B$ spectral components

$\boldsymbol{h}$: impulse response (PSF)

$\boldsymbol{n}$: noise

$(\boldsymbol{x}, \boldsymbol{y})$: contentious spatial coordinates

$(\boldsymbol{i}, \boldsymbol{j})$: discreet spatial coordinates

$\boldsymbol{f}(\boldsymbol{i}, \boldsymbol{j})$: the pixel value of the monochrome image f at coordinates (i, j)

$\boldsymbol{f_{lat}}$: latent monochrome image

$\widehat{\boldsymbol{f}}$: restored/ estimated monochrome image

$\widehat{\boldsymbol{h}}$: estimated PSF formed of $k \times k$ pixels

$\boldsymbol{f_E}$: estimated monochrome image from previous step

$\boldsymbol{h_E}$: estimated PSF from previous step

$*$: convolution operator

$\boldsymbol{\alpha}$: regularization parameter related to the PSF cost function

$\boldsymbol{\beta_{lat}}$: regularization parameter related to the latent image cost function

$\boldsymbol{\beta}$: regularization parameter related to the final image restoration

$\boldsymbol{\sigma}$: standard deviation

$\boldsymbol{\nabla}(.)$: gradient operator of $(.)$

$\boldsymbol{\nabla^2}(.)$: second order derivative of $(.)$

$\Delta(.)$: Laplacian operator of $(.)$

$\boldsymbol{D}$: first order derivative operator

$(.)^{\boldsymbol{T}}$: transpose of the matrix $(.)$

$(.)^{\boldsymbol{-1}}$: inverse of the matrix $(.)$

$\boldsymbol{WGCV}$: Weighted Generalized Cross Validation

$\boldsymbol{PSNR}$: Peak-Signal-to-Noise Ratio

$\boldsymbol{SNR}$: Signal-to-Noise Ratio

$\boldsymbol{SSIM}$: Structure Similarity Index Measurement

$\boldsymbol{E(L_1)}$: average L_1 norm by pixel

$\boldsymbol{ML_1}$: mean of L_1 norm

$\boldsymbol{MPSNR}$: mean of PSNR

$\boldsymbol{MSSIM}$: mean of SSIM

$\boldsymbol{MRMSE}$: mean of Root Mean Square Error

$\|.\|_p$: absolute value of the L_p norm

$\boldsymbol{MSE}$: Mean Square Error

$\boldsymbol{KS}$: Kernel Similarity

$\boldsymbol{MRI}$: Magnetic Resonance Image

$\boldsymbol{B18}$: spectral component number 18

CPU : Central Processing Unit

Résumé en français

Les images acquises par les capteurs subissent souvent une dégradation due à plusieurs facteurs. Ces facteurs comprennent le flou délocalisation, le mouvement ou la distorsion atmosphérique. Ces dégradations ont un impact significatif sur la qualité et la précision des images acquises, ce qui rend l'analyse et l'interprétation ultérieures difficiles. Par conséquent, une étape de restauration d'image est nécessaire pour récupérer l'image originale non dégradée.

Dans ce contexte, la restauration d'image présente un challenge considérable lorsque les valeurs des paramètres de régularisation, la PSF (Point Spread Function) et d'autres connaissances *a priori* ne sont pas disponibles. Par conséquent, la conception d'une méthode de restauration d'image fiable, qui se repose uniquement sur l'image dégradée, sans nécessité d'informations préalables, est un problème complexe.

Une méthode de restauration optimale doit répondre à plusieurs objectifs, notamment la restauration efficace tout en préservant les détails de l'image, et être facile à utiliser pour différentes applications. Par exemple, elle devrait éliminer l'ajustement empirique des valeurs des paramètres de régularisation spécifiques à chaque application.

Sur la base des connaissances *a priori* fournies par l'utilisateur, nous avons catégorisé les méthodes de restauration en trois classes :

Classe non aveugle : Dans cette catégorie, le processus de restauration repose sur une connaissance complète de la PSF, y compris la taille du support et les valeurs, qui sont fournies par l'utilisateur en tant que connaissances *a priori*. Cependant, la fixation empirique des valeurs des paramètres de régularisation dans cette classe ne garantit pas une restauration d'image optimisée.

Classe semi-aveugle : Cette classe implique une connaissance partielle de la PSF, où l'utilisateur fournit des informations concernant la taille du support de la PSF et fixe les valeurs des paramètres de régularisation.

Classe aveugle : Les techniques de restauration de cette catégorie reposent uniquement sur l'image observée pour estimer la PSF (taille du support et valeurs), l'image d'origine et les paramètres de régularisation.

La littérature scientifique sur la restauration d'images est assez vaste et de nombreuses méthodes ont été proposées, principalement dans un contexte semi-aveugle plutôt que complètement aveugle. Quoi qu'il en soit, l'objectif ultime de toute méthode de restauration est d'obtenir une image aussi proche que possible de la version originale.

Dans le cadre de cette thèse, nous portons une attention particulière aux deux dernières classes de méthodes. Dans la plupart des cas, les méthodes désignées comme aveugles sont en réalité semi-aveugles, car elles reposent encore sur un minimum d'informations *a priori*. L'objectif final est d'éliminer efficacement cette dépendance en estimant les informations nécessaires. Résoudre ce problème complexe

nécessite le développement d'une approche sans connaissance *a priori*. Deux approches sont couramment utilisées pour ces deux classes :

Approche alternée : Dans cette approche, l'estimation de la PSF et de l'image d'origine se fait de manière alternée.

Approche hybride : Cette approche consiste à estimer alternativement la PSF et une image latente avant de procéder à l'estimation de l'image d'origine.

Les principales raisons de cette situation critique de la restauration aveugle d'images résident dans le compromis crucial à réaliser entre plusieurs objectifs différents (élimination du flou, préservation des textures, amélioration des détails, lissage des régions homogènes) et dans l'ajustement manuel nécessaire des valeurs des paramètres de régularisation correspondant à ces objectifs.

Le modèle standard d'observation d'une image monochrome dégradée est exprimé par l'équation suivante: $g = h * f + n$, où g représente l'image dégradée observée, f l'image d'origine à restaurer, h la PSF considérée comme linéaire et invariante spatialement, et $(h * f)$ l'image floutée. Le bruit n est supposé être additif, indépendant et non corrélé à l'image d'origine f. Ce modèle choisi paraît adéquat pour résoudre le problème que nous visons dans cette thèse, en offrant un équilibre optimal entre la complexité des processus impliqués et la qualité des résultats obtenus.

L'estimation de la PSF et la restauration de l'image d'origine sont réalisées en formulant une fonction coût à minimiser qui intègre à la fois l'image et la PSF. Cette fonction coût est composée du terme de fidélité aux données et de deux termes supplémentaires de régularisation comme suit :

$$C(f,h) = \|g - h * f\|_2^2 + \boldsymbol{\lambda_f} R_f(f) + \boldsymbol{\lambda_h} R_h(h)$$

Où le premier terme désigne la fidélité aux données, R_f représente le terme de régularisation lié à la fonction coût de l'estimation de l'image, et R_h correspond au terme de régularisation lié à la fonction coût de l'estimation de la PSF. λ_f et λ_h sont les paramètres de régularisation associés à $R_f(f)$ et $R_h(h)$, respectivement.

Pour obtenir la solution optimale qui minimise cette fonction coût, il est nécessaire d'estimer les paramètres de régularisation plutôt que de fixer leurs valeurs. Pour l'estimation de *f* et de *h*, la fonction coût peut être décomposée comme suite :

$$C(f) = \|g - h_E * f\|_2^2 + \boldsymbol{\lambda_f} R_f(f)$$

$$C(h) = \|g - h * f_E\|_2^2 + \boldsymbol{\lambda_h} R_h(h)$$

h_E et f_E désignent respectivement la PSF et l'image estimées et sont supposées fixes dans les fonctions coût mentionnées ci-dessus.

En se basant sur le modèle d'observation, les méthodes de restauration, qu'elles soient aveugles, semi-aveugles ou non aveugles, introduisent des termes de régularisation dans le but de remplacer le problème initial mal posé par un problème bien posé. Cela revient à imposer des contraintes supplémentaires sur les caractéristiques souhaitées de l'une ou l'autre des inconnues : l'image originale et la PSF.

L'objectif de cette thèse est donc de développer une méthode de restauration facilement applicable en éliminant la nécessité d'une information préalable et d'un réglage empirique des paramètres. Dans ce cadre, la méthode de restauration hybride aveugle recherchée doit améliorer la qualité de la restauration, en fournissant une solution optimale pour toutes les tâches de restauration d'images, surpassant les approches récentes de l'état de l'art. Pour répondre efficacement à ce problème, cette thèse se concentre sur le développement d'une méthode adaptative aveugle de restauration d'images qui fonctionne sans informations préalables.

La thèse est composée de trois chapitres après une introduction. *Le premier chapitre* est consacré à l'analyse des méthodes de restauration récentes de l'état de l'art. Neuf méthodes récentes classées comme méthodes non neuronales semi-supervisées et une méthode neuronale supervisée sont étudiées et les valeurs fixes des paramètres de régularisation des fonctions de coût utilisées pour optimiser les solutions sont mises en évidence. En outre, une discussion détaillée est menée pour souligner les avantages, les inconvénients et les limites de ces méthodes.

Dans le *deuxième chapitre*, une étude détaillée est menée pour évaluer l'impact des paramètres de régularisation prédéfinis sur la qualité de la restauration d'images. La méthode hybride proposée par Pan et al. a été choisie pour cette étude en raison de ses meilleures performances par rapport aux méthodes évaluées dans notre laboratoire. Divers critères d'évaluation objectifs sont présentés et classés en deux catégories : les critères non aveugles et les critères aveugles. Cette étude vise à démontrer que la qualité de la restauration d'images varie en fonction du choix empirique des valeurs des paramètres de régularisation dans les fonctions coût, conduisant à des résultats sous-optimaux. L'influence du choix empirique de ces valeurs sur les résultats de la restauration est analysée à l'aide de deux images monochromes dégradées par trois fonctions de mouvements différents avec différentes tailles de support de la PSF. Les critères d'évaluation comprennent le PSNR, le SNR, la norme L_1, le MSE et le SSIM. Cette étude souligne l'importance de l'estimation automatique des valeurs des paramètres de régularisation qui peuvent s'adapter à différents types de flou et à chaque image dégradée, plutôt que de s'appuyer sur des valeurs fixes définies par l'utilisateur.

Le *troisième chapitre* est consacré à la méthode de restauration adaptative aveugle développée et explore plusieurs améliorations qui optimisent les résultats de la restauration tout en minimisant les connaissances préalables requises. La méthode proposée peut être appliquée à la restauration d'images monochromes, multispectrales et hyperspectrales. Pour le traitement des images hyperspectrales, deux stratégies de restauration sont proposées : la première consiste à former des groupes de composantes spectrales fortement corrélées à l'aide d'une méthode de partitionnement non supervisée développée au laboratoire. Pour chaque groupe ainsi formé, une composante spectrale exemplaire est sélectionnée pour le représenter, et l'estimation de la PSF est effectuée en utilisant uniquement ces composantes exemplaires. Ensuite, la PSF estimée de chaque groupe est utilisée pour restaurer toutes les composantes spectrales au sein du groupe désigné. Pour la deuxième stratégie, l'estimation de la PSF la plus précise parmi les PSF obtenues dans le cadre de la première stratégie est sélectionnée à l'aide du critère de la norme L_1 de l'erreur d'estimation entre la composante exemplaire de l'image dégradée observée et son estimé de chaque groupe. La PSF sélectionnée est ensuite utilisée pour restaurer toutes les composantes spectrales de l'image hyperspectrale. La seconde stratégie permet une meilleure restauration de l'image que la première.

Les évaluations menées sur diverses bases de données d'images démontrent la supériorité de la méthode de restauration adaptative aveugle que nous proposons par rapport à onze méthodes non-neuronales et neuronales supervisées/semi-supervisées de l'état de l'art. Pour évaluer les résultats de restauration, nous avons sélectionné plusieurs critères, notamment le PSNR, le SSIM, le RMSE et la norme L_1de l'erreur d'estimation.

Cette supériorité s'étend aux images monochromes, multispectrales et hyperspectrales dégradées avec différentes fonctions floues (mouvement et délocalisation) et tailles de support. Pour l'évaluation des images hyperspectrales, nous avons également observé localement les signatures spectrales.

En conclusion, la méthode proposée répond efficacement aux objectifs fixés. Elle permet une application facile grâce à sa nature aveugle tout en optimisant les résultats de la restauration sans nécessiter de réglage empirique des paramètres. Les résultats de l'évaluation ont démontré son efficacité par rapport aux principales méthodes existantes de l'état de l'art comparées. Elle peut s'appliquer pour restaurer des images monochromes, multispectrales et hyperspectrales.

General introduction

Image restoration is a technique used to improve image quality by removing degradation caused by blur and noise. This process enables better analysis and interpretation of the image's information content. It is applied in numerous application fields such as medicine, civil and military safety, environment, using various data types like monochrome, multispectral, hyperspectral (HSI), and MRI.

A hyperspectral image (HSI) is a 3-D image captured using multiple spectral components spanning from the visible to near-infrared spectrum [1][2][3][4]. It consists of hundreds of narrow and consecutive components, allowing for accurate material identification and finding applications in fields such as military, agriculture, and mineralogy. Unlike conventional RGB or grayscale images, each pixel in an HSI contains a continuous spectrum, enhancing pixel differentiation [5][6]. This unique characteristic has led to the extensive use of HSIs in various computer vision tasks, including target detection [5], change detection [7], scene classification [8][9][10], and object tracking [11].

We are interested in the reliability and applicability of the optimized restoration methods, specifically blind or semi-blind, to automatically and accurately performing image deburring using the observed image. Despite the availability of a large number of methods, selecting a suitable technique and effectively adjusting its parameters to achieve meaningful results for a specific application remains a challenging task for users.

An optimal restoration method must jointly meet multiple objectives, including effective deblurring while preserving image details, and being user-friendly for various applications. For instance, it should eliminate the need for tedious empirical adjustment of the regularization parameter values specific for each application.

Based on the prior information introduced by the user, we have categorized the restoration methods into three classes:

Non-blind class: Within this category, the restoration process relies on complete knowledge of the point spread function (PSF), including support size and values, which are provided by the user as prior knowledge. However, the empirical fixing of regularization parameter values in this class does not guarantee optimized image restoration.

Semi-blind class: This class involves partial knowledge of the PSF, where the user provides information regarding the PSF's support size and fixes the regularization parameters accordingly.

Blind class: The restoration techniques in this category solely rely on the observed image to estimate the PSF (support size and values), the original image, and the regularization parameters.

The scientific literature on blind restoration of digital images is quite extensive, and numerous methods proposed, mostly in a semi-blind context rather than a fully blind one. In any case, the ultimate goal of any restoration method is to obtain an image that is as close as possible to the ideal image.

In the scope of this thesis, we pay particular attention to the last two classes of methods. In most cases, so-called blind methods are actually semi-blind, as they still rely on a minimum amount of a priori information. The final objective is to effectively eliminate this reliance by estimating the required information. Solving this complex problem requires the development of an approach with no a priori knowledge. Two approaches are commonly used for these two classes:

Alternated approach: In this approach, the estimation of the point spread function (PSF) and the original image occurs consecutively.

Hybrid approach: This approach involves alternately estimating the PSF and a latent image before proceeding to estimate the original image.

The main reasons leading to this critical situation of blind image restoration lie in the crucial compromise that needs to be made among several different objectives (blur elimination, texture preservation, detail enhancement, smoothing of homogeneous regions) and the necessary manual adjustment of regularization parameters corresponding to these objectives.

Despite the large number of available methods, it is difficult for a user to choose a specific method that achieves meaningful results for a target application. Furthermore, several drawbacks arise from the difficulty faced by the user in formalizing adequate values for the regularization parameters weighting the regularization terms in the cost functions. These parameters must be defined according to the characteristics expected from the solutions sought and meet the convergence requirements.

- **Observation model**

The standard observation model used for a monochrome degraded image is as follows:

$$g = h * f + n \tag{0.1}$$

In this model, g represents the observed degraded image, f is the original image to be restore, h is the PSF (Point Spread Function) considered as linear and spatially invariant, and $(h * f)$ is the blurred image. The noise n is assumed additive, independent, and non-correlated with the original image f.

The selected model should enable us to achieve the best compromise between the complexity of the implemented processes and the quality of the results obtained.

- **Discussion on the problematic**

Based only on the observed image, the challenging goal of blind restoration of a degraded image is to effectively estimate the degradation function and restore the original image.

In case of a total blind restoration approach, no prior information about the original image and the degradation is available, making the problem difficult. However, in practice, to partially mitigate the difficulties, the PSF is generally modeled as a linearly invariant operator.

In particular, the two properties mentioned above are often considered for multi- and hyper-spectral images [12], especially in those acquired by remote sensing systems (mounted on satellite, airborne, or more recently drone platforms) [13][14].

Hyperspectral images are subject to degradation from observation noise [15][16][17], and they can also be affected by blur [18]. Various factors contribute to the blur in hyperspectral images, such as lens imperfections, defocusing, atmospheric or air turbulence, relative motion between the sensor and the scene, or even sensor degradation occurring after the acquisition platform's deployment.

Note that the spatial invariance of the PSF is a property imposed on the blur in each spectral component to simplify the problem compared to the more general assumption of a spatially varying blur impulse response [13].

Another characteristic of hyperspectral images is that the spectral signature and the corresponding signal-to-noise ratio in each spectral component are known to vary along the spectral dimensions [16][19]. Therefore, it is essential that, at the output of the restoration phase, the original spectral signature of the imaged content is recovered at each spatial position.

Consequently, the estimation of the PSF and the restoration of the original image are accomplished by formulating a cost function that incorporates both the image and the PSF. This cost function consists of the following components:

$$C(f,h) = \|g - h * f\|_2^2 + \boldsymbol{\lambda_f} R_f(f) + \boldsymbol{\lambda_h} R_h(h) \tag{0.2}$$

Where the first term denotes data fidelity, R_f represents the regularization term related to the cost function of image estimation, and R_h corresponds to the regularization term associated with the cost function of PSF estimation. λ_f and λ_h are the regularization parameters associated with $R_f(f)$ and $R_h(h)$, respectively.

The objective of the cost function (0.2) is to estimate the original image f. To obtain the optimal solution that minimizes the cost function (0.2), it is also necessary to estimate the regularization parameters λ_f and λ_h instead of fixing their values. The cost function (0.2) can be solved using the half quadratic splitting technique and expressed as equations (0.3) and (0.4).

$$C(f) = \|g - h_E * f\|_2^2 + \boldsymbol{\lambda_f} R_f(f) \tag{0.3}$$

$$C(h) = \|g - h * f_E\|_2^2 + \boldsymbol{\lambda_h} R_h(h) \tag{0.4}$$

In equations (0.3) and (0.4), h_E and f_E represent the estimated PSF and image from the previous iteration, respectively. Additionally, they are supposed to be fixed.

- **Conclusion**

Based on the observation model, restoration methods, whether blind, semi-blind, or non-blind, introduce regularization terms with the objective of transforming the ill-posed initial problem with a well-posed problem, this is equivalent to imposing additional constraints on the desired characteristics of either one or both unknowns: the original mage and the PSF.

In practice, this results in the addition of extra regularization terms to the usual data fidelity term as shown in equation (0.2). Each of these terms is weighted by an associated regularization parameter to adjust its relative weight in the overall objective function to be optimized. The goal is to achieve the closest

approximation to the solution of the initial problem while ensuring facilitated convergence of the cost function.

The compromise often encountered in practice is to settle for an acceptable approximation of the true unknown solution. However, some of these methods, when finely tuned, can achieve quite impressive results according to well-known standard evaluation criteria such as Structure Similarity Index Measurement (SSIM) or Peak-Signal-to-Noise Ratio (PSNR).

However, it's important to highlight several drawbacks related to unresolved issues. Among them, we can mention the difficulty of formulating appropriate regularization terms concerning the expected characteristics of the desired solutions on one hand, and the convergence requirements on the other hand. Additionally, there is also the potential instability of the resulting method, convergence to local minima, manual or non-automatic adjustment of the optimal values of the involved regularization parameters, and sensitivity to the choice of initialization for different unknown variables (original image, PSF).

Therefore, in the scope of this thesis, we are interested in the ability and applicability of the blind restoration methods to operate automatically, efficiently and with no manual adjustment for the restoration of monochrome and hyperspectral images.

- **Structure of the thesis**

This thesis manuscript consists of three chapters. The first chapter is dedicated to the state-of-the-art, providing an overview of the existing research in the field. In the second chapter, an assessment is conducted to evaluate the influence of manual adjustment of the regularization parameters on the image restoration quality. Finally, the third chapter outlines different proposals to enhance the final quality of the restoration. The following paragraphs provide a detailed overview of the content in each of the three chapters. Lastly, to conclude the entirety of the analyses and work conducted in this thesis, this document ends with a general conclusion and outlines prospects for future research.

- **Detailed content of each chapter**

Chapter 1: state of the art: analysis of the recent methods

The objective of this first chapter is to present the methods developed in the literature for solving the posed restoration problem. Among these methods, we have selected those that require a minimum amount of prior knowledge (semi-blind) and/or utilize neural networks, as there are no truly blind methods in reality. A representative set of nine proposed methods in the literature has been chosen. These methods are all based on the same observation model, which is identical to the one selected in (0.1). However, they require prior knowledge such as the PSF support size, the values of regularization parameters, the number of layers, learning rate, and more.

Chapter 2: Influence of the regularization parameters over the restoration quality

In the second chapter, our aim was to evaluate the influence of manually adjusting the regularization parameters for the original method proposed by Pan et al and selected by Zhang Mo in her previous thesis. To conduct this study, a database of monochrome images was utilized. Before conducting the comparative study, we provided a reminder regarding the evaluation criteria used to assess the quality of restored images. Subsequently, the assessment of restored image quality for different regularization parameter

values was performed using several evaluation metrics such as PSNR, SSIM, MSE, and the L_1 norm of the estimation error.

The study initially demonstrated that the fixed regularization parameter values in the original method are not optimal. Furthermore, this evaluation emphasized the importance of estimating these regularization parameter values instead of manually fixing them, as it ensures optimal image restoration quality.

Chapter 3: Developed blind method

In this chapter, we focus on the developed approach, which is based on the same principles as the PAN method. The first section provides a comprehensive overview of the various steps involved in the proposed method. It emphasizes the properties and characteristics of the selected solutions for PSF and latent image estimation, as well as the final image restoration.

Moving on to the second section, we focus on the enhancements proposed to improve the restoration results of the original image while minimizing the required prior knowledge. These modifications aim to optimize the method by utilizing a noiseless observation model.

The third represents the proposed strategies to restore a full hyperspectral image by blindly selecting a exemplar spectral component to represent highly correlated spectral components groups in order to reduce the number of spectral components used for the PSF estimation.

In the fourth section, we present a series of tests conducted to evaluate the performance of the proposed blind method. These tests demonstrate its superiority not only over the original method but also over recent methods proposed in the literature. The proposed method is validated using diverse databases containing monochrome, multicomponent, and hyperspectral images.

Overall, this chapter covers the development and evaluation of the proposed approach, showcasing its effectiveness and advancements over existing methods.

Chapter 1: State-of-the-art

1. Introduction

In this chapter, we analyze recent and representative methods from the literature to provide a deeper understanding of their principles, advantages, drawbacks, and limitations in the context of our study. These methods are considered semi-blind because they rely on prior knowledge, including the support size of the Point Spread Function (PSF), the values of regularization parameters that weight the regularization terms in the cost functions, the number of layers consisting the network architecture in the case of a CNN, the predefined training sets, etc.

To better represent the state-of-the-art methods, we have identified two distinct approaches for image restoration commonly used to restore degraded images based on their optimization principles. The first approach is an alternate method in which the point spread function and the original image are estimated consecutively. The second approach is a hybrid method, where the PSF is estimated first using an alternate method with an intermediate image, and the estimated PSF is then used to restore the final image.

For this study, we have selected nine methods, each of which uses regularization terms in their cost function, weighted by regularization parameters, to estimate the original component and the PSF (component by component).

In the following paragraphs, we will briefly describe these nine methods. The description will highlight their underlying principles, the corresponding set of parameters to be adjusted by the user, and the recommended values for these parameters by the method authors.

2. Alternated approach

In our analysis, we have selected three methods belonging to the alternate approach namely Alternative Direction Method of Multipliers (ADMM) [20], Sroubek [23], and Ren [24]. For each of these methods, we will describe their principle and practical implementation conditions.

Method 1: Alternating Direction Method of Multipliers

The method described in [20] can be considered as an extension of the standard method [21], which employs the Alternating Direction Method of Multipliers (ADMM) technique. The goal is to benefit from the fast convergence speed of this efficient optimization tool under non-smooth convex regularization. The ADMM technique involves breaking down the original challenging optimization problem into simpler sub-problems that can be easily solved using, for instance, a fast Fourier transform or wavelets if the observational operator can be assumed in a circulant version, or by utilizing proximal operators.

The method presented in [20] uses a slightly different cost function than that in [21] and is optimized according to the image f and PSF h as shown in (1).

$$C(f,h) = \frac{1}{2}\|g - h * f\|_2^2 + \boldsymbol{\lambda}\sum_i \left(\|F_i(f)\|_q\right)^q + \iota_{s+}(h) \quad (1)$$

This method differs from the standard method in [21] in terms of the specific choice of a non-convex and non-smooth regularization term, denoted as $L_{1/2}$, defined as $L_{1/2}(.) = \|.\|_{1/2}^{1/2}$ and related to the image estimation f. This particular choice of the parsimony parameter $q = \frac{1}{2}$ allows us to benefit from an analytical solution that can be expressed and solved by an iterative thresholding algorithm [22], leading to a faster solution.

The operator $F(.)$ is an edge detection operator in the four cardinal directions (Sobel operator), and i representd the i^{th} pixel in the edge image. The regularization term related to the PSF estimation is represented a function indicator, $\iota_{s+}(.)$, for a set of filters (PSFs) with positive input on a given support (L_1 norm of the positive PSFs).

The default sequence proposed for the regularization parameter λ related to the PSF estimation is different from that defined by the author in [21], which is based on standard gradient descent. In this case, the initial value of λ is considered to be equal to ½, and the ratio of the geometric progression is $\frac{1}{r}$ with $r \geq 1.5$.

Method 2: Sroubek

The second method, proposed by Sroubek et al. [23], follows the same regularization approach as the previously described method. The estimation of the original image component is achieved through the use of an isotropic regularization term (total variation with L_2 norm), which is chosen to acquire a solution with a sparse distribution of the image gradient, as shown in (2).

$$\begin{aligned} C(f) &= \frac{\boldsymbol{\gamma}}{2}\|g - h_E * f\|^2 + R_f \\ \text{With } R_f &= \sum_i \sqrt{\left(\nabla_x f(i)\right)^2 + \left(\nabla_y f(i)\right)^2} \end{aligned} \tag{2}$$

The regularization parameter γ is inversely proportional to the noise variance, and R_f represents the regularization term related to the image estimation.

To achieve the balance between complexity and precision in the PSF estimation, the authors in [23] defined a regularization term that ensures the positivity property of the PSF (penalizing negative values) and the parsimony of its coefficients (by calculating the L_1 norm of positive PSFs), as shown in (3).

$$\begin{aligned} C(h) &= \frac{\boldsymbol{\gamma}}{2}\|g - h * f_E\|^2 + R_h \\ \text{With } R_h &= \sum_i \psi\big(h(i)\big), \qquad \psi(\varsigma) = \begin{cases} \varsigma & if\ \varsigma \geq 0 \\ +\infty & otherwise \end{cases} \end{aligned} \tag{3}$$

This method applies an alternate minimization of the global function with respect to the original image and the PSF. The two updated steps involve a specialized function $L\big(f, v_x, v_y\big)$ and $L(h, w)$, shown in (4) and (5) respectively. This is achieved by using the technique of variable separation to substitute either the derivatives in the horizontal and vertical directions of the unknowns located in the regularization term of

type TV, or simply the unknown PSF in the corresponding regularization term. An augmented Lagrangian method (ALM) is used to transform the constrained problem into an unconstrained one.

$$L(f, v_x, v_y) = \frac{\gamma}{2}\|g - h_E * f\|^2 + R_f(v_x, v_y) + \frac{\alpha}{2}\|D_x f - v_x - a_x\|^2 + \frac{\alpha}{2}\|D_y f - v_y - a_y\|^2 \quad (4)$$

$$L(h, w) = \frac{\gamma}{2}\|g - h * f_E\|^2 + \psi(w) + \frac{\beta}{2}\|h - w - b\|^2 \quad (5)$$

With $v_x = D_x f$, $v_y = D_y f$ and a_x, a_y, b are the variables introduced by the augmented Lagrangian method.

The two updating steps for estimating either the original image or the PSF are solved with an iterative algorithm. The number of iterations of the main loop and the two update stages are limited (less than ten) to avoid local minima.

Method 3: Ren

This method [24], conducted by Dongwei Ren et al., connects Maximum A Posterior (MAP) and deep models by proposing two generative networks for modeling clean images and PSF, respectively. The approach adopts an asymmetric autoencoder and a fully connected network (FCN) to detect the structure of the clear image and the PSF, respectively. Moreover, a SoftMax function is applied at the output of the FCN to ensure the PSF constraints.

Inspired by the Deep Image Prior network [25], the authors used an image generator network $\mathcal{G}_f$, which is an asymmetric autoencoder with skip connections, to capture the statistical properties of the underlying clean image. However, $\mathcal{G}_f$ is not well-suited to characterizing the prior of the PSF. To address this, the authors suggested the use of a fully-connected network (FCN) called $\mathcal{G}_h$ for modeling the prior of the PSF. The SoftMax nonlinearity is applied to the output layer of $\mathcal{G}_h$ to ensure that the PSF satisfies non-negativity and equality constraints.

By fixing the network structures ($\mathcal{G}_f$ and $\mathcal{G}_h$) and inputs (z_f and z_h) sampled from a uniform distribution, they have formulated a deconvolution neural optimization problem on the network parameters of $\mathcal{G}_f$ and $\mathcal{G}_h$ as follows:

$$\min_{(\mathcal{G}_f, \mathcal{G}_h)} \left\|\mathcal{G}_h(z_h) * \mathcal{G}_f(z_f) - g\right\|^2 + \boldsymbol{\lambda}\, TV\left(\mathcal{G}_f(z_f)\right) \qquad s.t.\, 0 \le \left(\mathcal{G}_f(z_f)\right)_i \le 1\,, \forall i \quad (6)$$

$$\left(\mathcal{G}_h(z_h)\right)_j \ge 0, \sum_j \left(\mathcal{G}_h(z_h)\right)_j = 1, \forall j$$

$TV\left(\mathcal{G}_f(z_f)\right)$ is the regularization term used to capture image priors. λ is the regularization parameter for the image prior that is controlled by the noise level.

However, certain parameters such as the number of layers in the deep neural network, the learning rate used during training, and the regularization parameter used to balance the data fidelity term and the regularization term in the cost function, must be set by the user.

For the experiments conducted in [24], four empirically fixed parameters by the user: the number of layers set to 5, the learning rate is set to 0.01 and decreases by 0.5 at the iteration 2000, 3000, and 4000, and the regularization parameter $\lambda = 10^{-6}$ is imposed to improve the robustness in handling blurred images.

3. Hybrid approach

In contrast to previous alternating methods, the approaches introduced in this section first estimate the PSF, often using the image contours extracted from an estimated intermediate (latent) image or the degraded image. The advantage of this approach is that the maximum a posteriori formulation no longer fails when the estimation concerns $(h, \nabla f)$, with ∇f representing the gradient of the original image [49]. Once the PSF is well estimated, it is injected into the final restoration process to estimate the original image. These methods are called Pan, Haoyuan, Zhou, Huang, Zhang, and Ge. For these methods, we will explain their principles, as well as the practical conditions for implementation.

Method 4: PAN

Pan et al. [26][27] proposed a method that suggests detecting, selecting, and using sufficiently salient edges in an image to achieve a more precise PSF estimation. Although edges in a degraded image can provide relevant information for PSF estimation, not all edges are useful for this purpose. Only salient contours with large amplitude values of the L_2 norm of the gradient can positively impact and improve the precision of the PSF estimation. Conversely, lower amplitude contours, small details, and rich textures can deteriorate the PSF estimation, leading to decreased precision, noise, or poor estimation. Such content in the degraded component can severely weaken the accuracy of the PSF estimation, particularly for blur with large support values. A deconvolved degraded component with a PSF estimated from all contours without distinction is likely to have an unacceptable level of residual blurring and severe artifacts.

Therefore, the selection of appropriate structures in a degraded component to support the estimation of the PSF is of utmost importance for obtaining an acceptable restoration result. Pan et al. achieved this objective by implementing an alternating multi-scale estimation of an intermediate latent image and the PSF before proceeding with the final image restoration using the estimated PSF.

Given the current version of the latent image, the estimation of the Point Spread Function (PSF) is obtained by detecting, selecting, and efficiently using sufficiently salient contours in the intermediate latent image. To achieve this objective, the latent image is decomposed into two components: one being structural and the other textural. This is done by optimizing an appropriate energy function that involves the L_2 norm of the gradient amplitude of the structural component. It separates the main useful structures from the harmful fine-scale details and the noise grouped together within the texture component. The texture is removed using an adaptive total variation regularization term. Next, the main structures retained, which are essentially the edges, are improved by shock filtering, and the salient edges are selected. Finally, the PSF estimation is carried out only based on the salient edges, with an a priori constraint of parsimony and continuity.

Then, given the current estimation of the PSF, the estimation of the intermediate latent image is updated by imposing that the gradient of the current unknown is sufficiently close to those of the salient contours previously selected. This update is accomplished by using low-rank before imposing a denoising effect on the current estimate.

Therefore, this method involves considering a pyramidal multi-resolution image and iteratively estimating the PSF and an intermediate latent image, which is initialized by the observed image. The estimation of the PSF is based on the adequate selection of sufficiently contrasting and salient contours in the current intermediate latent image, and this selection process involves three steps.

Firstly, the current latent image is decomposed into two components, one being structural and the other textural, using an adaptive isotropic total variation $TV - L_2$ regularization term when no a priori knowledge on the texture is available. To improve the decomposition, the weight on the fidelity term of the current latent image is increased.

Secondly, the structural component is improved and enhanced by shock filtering.

Lastly, the salient edges with large values of L_2 norm of the gradient are selected by thresholding the enhanced structural component, $(\widetilde{I_s})$. The threshold is initially set to ensure that a minimum number of $0.5 \times \sqrt{n_i . n_k}$ pixels participate in the estimation of the PSF in each of the sectors, where n_i and n_k denote the total number of pixels in the image and the PSF, respectively, with $n_i = M \times N$ and $n_k = k \times k$. Its value is then regularly reduced as the iterations progress.

At each scale, the current intermediate latent image, f_{lat}, is first divided into a structural component containing the main edges, denoted as I_s, and a texture component defined as its complementary part, denoted I_t, simply calculated by $I_t = I - I_s$. This is achieved by minimizing the cost function (7) [28]:

$$C(I_s) = \sum_x \|\nabla I_s\|_2 + \frac{1}{2\theta\omega(x)}\left(I_s(x) - I(x)\right)^2 \tag{7}$$

Here θ is an adjustment parameter, and $\omega(x) = e^{\left(-r(x)\right)^{0.8}}$, where $r(x) = \frac{\left\|\sum_{y\in\Re_h(x)} \nabla g(y)\right\|_2}{\sum_{y\in\Re_h(x)}\|\nabla g(y)\|_2 + 0.5}$ with $\Re_h(x)$ is a window of size 5×5 centred at x to ensure the spatial adaptivity.

The enhanced structural component obtained by shock filtering [29] is given by:

$$\frac{\partial \widetilde{I_s}}{\partial t} = -sign\left(\Delta \widetilde{I_s}\right) \times \left\|\nabla \widetilde{I_s}\right\|_2 \tag{8}$$

Finally, the salient edges are obtained by using the equation (9).

$$\nabla S = \nabla \widetilde{I_S} \odot H\left(\left\|\nabla \widetilde{I_S}\right\|_2, tr\right), \text{ with } H\left(\left\|\nabla \widetilde{I_S}\right\|_2, tr\right) = \begin{cases} 1, & if \left\|\nabla \widetilde{I_s}\right\|_2 \geq tr \\ 0, & otherwise \end{cases} \tag{9}$$

The operator $\odot$ denotes element-wise multiplication, and tr denotes a threshold applied to the norm of the gradient of the current version of the structural component after shock filtering.

Following the three previous steps, the PSF is estimated using a priori Hyper Laplacian. The corresponding cost function (10) is optimized using an iterative reweighted least squares (IRLS) constrained method [30] given by:

$$C(h) = \|\nabla S * h - \nabla g\|_2^2 + \alpha\|h\|_{0.5}^{0.5} \quad \text{With } h(x) \geq 0,\ \sum_x h(x) = 1 \tag{10}$$

α represents the regularization parameter related to the PSF estimation. Once, the new version of the PSF (h) is estimated, the intermediate latent image is updated by solving an anisotropic total variation term (11), using an IRLS method.

$$C(f_{lat}) = \lambda\|f_{lat} * h_E - g\|_2^2 + \|\nabla f_{lat}\|_1 \tag{11}$$

where λ is a regularization parameter related to the latent image estimation noting that $\beta = \frac{1}{\lambda}$. Finally, the the original final image is estimated as follows:

$$C(f) = \|h_E * f - g\|_2^2 + \beta\left(e^{-\|\nabla_x S\|_{0.8}} \times \|\nabla_x f\|_1 + e^{-\|\nabla_y S\|_{0.8}} \times \left\|\nabla_y f\right\|_1\right) \tag{12}$$

Where β is a regularization parameter related to the final image restoration.

The authors of [26][27] have fixed the regularization parameters related to the PSF and the latent image estimation as $\alpha = 0.01$ and $\beta = 0.005$, respectively. Subsequently, following the PSF estimation phase, the regularization parameter related to the final image restoration is also fixed at $\beta = 0.003$, as per their report.

Method 5: Haoyuan

In this study [31], Yang et al. proposed a deblurring method based on sparse optimization. The method utilizes an image prior based on nonzero measurement in the image gradient domain and introduces an analytical solution without requiring additional searching iterations during optimization. First, the proposed method estimates the PSF using an alternating scheme and a half-quadratic optimization algorithm. Next, the latent sharp image is estimated using a non-blind deconvolution algorithm with priors based on the hyper-Laplacian distribution.

The joint cost function proposed in [31], denoted by $C(f, h)$, is formulated as follows:

$$C(f, h) = \|g - h * f\|_2^2 + \boldsymbol{\lambda_f} R_f + \boldsymbol{\lambda_h} R_h \tag{13}$$

Here, R_f and R_h represent the image and PSF regularization terms, respectively, and λ_f and λ_h correspond to their respective weights.

$$R_f = \sum_{i \in \Omega}\left(1 - \delta(|\nabla_1 f_i| + |\nabla_2 f_i| + |\nabla_3 f_i| + |\nabla_4 f_i|)\right) \quad \text{With } \delta(m) = \begin{cases} 0\ if\ m \neq 0 \\ 1\ if\ m = 0 \end{cases} \tag{14}$$

R_f is obtained from the nonzero measurements of the i^{th} element in the gradient image domain in four orientations, which are stored in lexicographic order [32]. Specifically, the pixel values of the gradient image domain are arranged in a vector using raster scan order, where pixels are scanned one by one from left to right and line by line. The gradient operator ∇_n, where $n \in \{1, 2, 3, 4\}$, corresponds to each orientation of $\left\{0, \frac{\pi}{2}, \frac{\pi}{4}, \frac{3\pi}{4}\right\}$.

Equation (14) essentially counts nonzero values in the four directions of the gradient image. An evaluation based on the histogram representation of an original image and its blurred image revealed that the pixel intensity is more concentrated in the blurred image, indicating that the blurred image has a higher sparsity. By assessing the nonzero values, it was confirmed that their intensity is significantly higher than that in the original image.

The joint cost function in Equation (13) is solved using an alternating scheme, where the PSF is estimated first, then the latent sharp image is acquired. Equation (13) is divided into two subproblems: one for the PSF estimation (15) and the other for the latent image estimation (16). These subproblems are then solved alternately as follows:

$$\hat{h} = \arg\min_{h}(\|g - h * f_E\|_2^2 + \boldsymbol{\lambda_h} R_h) \tag{15}$$

$$\hat{f} = \arg\min_{\mathrm{f}}\left(\|g - h_E * f\|_2^2 + \boldsymbol{\lambda_f} R_f\right) \tag{16}$$

To avoid local minima during PSF estimation, the authors of [32] employ a coarse-to-fine scheme using the image pyramid technique, generating the target image from coarse-to-fine levels.

Non-blind deconvolution algorithms can be applied with the estimated PSF to restore the final image. To further enhance the restoration result, sparse representation techniques can be utilized, that was inspired by the previously deployed PSF estimation method. Specifically, a hyper-Laplacian distribution-based prior is incorporated into the cost function as a regularization term. The cost function is formulated as follows:

$$C(f) = \|g - h_E * f\|_2^2 + \boldsymbol{\lambda_f} \left\|\left(\nabla_x f, \nabla_y f\right)\right\|_p \tag{17}$$

Here, p is derived from the hyper Laplacian model and serves as a constraint term in a quasi-norm form. $\nabla_x f$ and $\nabla_y f$ denote the horizontal and vertical image gradients, respectively. The cost function is solved using half-quadratic penalty method, similar to the solution of equation (16).

Furthermore, the weights of the image and the PSF priors, namely λ_f and λ_h, were empirically selected through experimental evaluation of the proposed method. The authors conducted experiments on various test images and evaluated the performance of the proposed method under different weight combinations of λ_f and λ_h. After examining the results, they concluded that the values of $\lambda_f = 0.2$ and $\lambda_h = 0.8$ offered the best trade-off between image quality and computational efficiency.

Method 6: Zhou

In [33], L. Zhou et al. proposed a new approach to restoring degraded images by combining two techniques: fractional-order total variation [34] and self-similarity features [35]. The total variation measures the amount of variation in an image, while fractional-order total variation extends this concept to fractional derivatives, which can capture complex image structures. Self-similarity features, refer to the inherent repeating patterns present in an image. The cost function used in [33] is given as follows:

$$C(f,h) = \|h * f - g\|_1 + \boldsymbol{\alpha_1}\|\nabla^r f\|_1 + \boldsymbol{\alpha_2}\|\nabla^2 h\|_2^2 + \boldsymbol{\lambda}\,\sigma_N^2\left(f^t \sum_{i,u} f\right) \tag{18}$$

Here, g is the degraded image, f and h represent the original image and the PSF respectively. While $\alpha_1, \alpha_2,$ and λ are their respective regularization parameters. σ_N^2 represents the noise variance of the observed blurry image. ∇^r denotes the r-order derivative, where r is a decimal number. $\sum_{i,u}\hat{f}$ denotes the patch-based Fractional Brownian Motion (FBM) [35] covariance matrix with Hurst parameter u and patch i. The cost function (18) is resolved using half-quadratic regularization.

The optimization of the proposed method is solved using iterative minimization, by splitting (18) into two cost functions: (19) and (20) for the image and PSF estimation, respectively, as shown below:

$$C(f) = \|h_E * f - g\|_1 + \boldsymbol{\alpha_1}\|\nabla^r f\|_1 + \boldsymbol{\lambda}\,\sigma_N^2\left(f^t \sum_{i,u} f\right) \tag{19}$$

$$C(h) = \|h * f_E - g\|_1 + \boldsymbol{\alpha_2}\|\nabla^2 h\|_2^2 \tag{20}$$

These two cost functions (19) and (20) are solved by setting their partial derivative with respect to f and h to zero, respectively.

In terms of the implementation details, α_1 is inversely proportional to the observed image noise, while α_2 is set to 1.4, λ is set to 0.25, and the decimal order r is set to 1.5. The evaluation conducted in [33] demonstrated that the proposed method effectively restored fine details and preserve edges compared to other state-of-the-art methods. However, the values of the regularization parameters in (18) were determined experimentally through multiple tests to balance the regularization terms. As a result, the proposed approach is not a blind image restoration technique as the regularization parameter values are subjectively fixed.

Method 7: Ge

Xianyu Ge et al. [36] propose a novel algorithm for image restoration based on projected alternating minimization (PAM) that incorporates a nonlinear channel (NLC) regularization term based on the dark channel [37] shown in equation (21) and bright channel [38] shown in equation (22).

$$C_d(f)_i = \min_{j\in\Phi(i)}(\min f(j)) \tag{21}$$

$$C_b(f)_i = \max_{j\in\Phi(i)}(\max f(j)) \tag{22}$$

These channels, $C_d(f)_i$ and $C_b(f)_i$, represent the dark and bright channels, respectively, of a grayscale image f at a location i. $\Phi(\mathrm{i})$ refers to a local image patch, and j denotes the position within this patch.

According to [38][39], clean images have dark channel pixels that are not greater than their blurred versions, whereas the bright channel pixels have the opposite impact. The authors in [36] defined the NLC as a ratio between the dark channel and the bright channel represented in (23).

$$C_{nl}(f)_i = \frac{C_d(f)_i}{C_b(f)_i} \tag{23}$$

The cost function adopted in this proposed method is expressed as follows:

$$C(f,h) = \|h * h - g\|_2^2 + \boldsymbol{\alpha} \|C_{nl}(f)\|_1 + \boldsymbol{\beta} \|\nabla f\|_0 + \boldsymbol{\gamma} \|h\|_2^2 \tag{24}$$

Here, the parameters α, β, and γ are the regularization parameter that balance the regularization terms related to the image and PSF, respectively. The first term in this cost function is the fidelity term, and the second term is the non-linear channel. The third term was introduced in [40] for edge preservation, and the fourth term is the regularization term related to the PSF estimation.

To solve the cost function in (24), a projected alternating minimization (PAM) [41] is used to alternately estimate the PSF and the original image. Therefore, (24) is divided into two cost functions one for the image restoration and the other for the PSF estimation shown in equations (25) and (26), respectively.

$$C(f) = \|h_E * f - g\|_2^2 + \boldsymbol{\alpha} \left\| \frac{C_d(f)}{C_b(f_E)} \right\|_1 + \boldsymbol{\beta} \|\nabla f\|_0 \tag{25}$$

$$C(h) = \|h * f_E - g\|_2^2 + \boldsymbol{\gamma} \|h\|_2^2 \tag{26}$$

Where f_E is the latent image estimated in the previous iteration.

A coarse-to-fine approach is used to estimate the PSF, using a pyramidal model with a fixed down-sampling factor $\frac{\sqrt{2}}{2}$. The regularization parameters that balance the NLC prior and the image regularization term are fixed $\alpha = \beta = 0.004$. The regularization parameter related to the PSF estimation is predefined by the user, set to $\gamma = 2$. The NLC patch size is fixed to 35×35.

Method 8: Huang

Liqing Huang et al. proposed in [42] a method based on combining convolutional neural network (CNN) and PSF estimation module. The proposed method consists of two main stages: PSF estimation and image restoration.

The first stage of the proposed method involves identifying the type of blur and estimating of the corresponding PSF. The blur kernel is a mathematical representation of the blur introduced in the image due to various factors like camera motion or out-of-focus imaging. To estimate the PSF, the proposed method utilizes a PSF estimation module in a patch-based manner. The module is based on a deep learning architecture, including a convolutional neural network (CNN) and a regression layer. The CNN takes a

patch of the blurred image as input and generates a set of features, which are then fed to the regression layer to estimate the PSF. Additionally, to determine the support size of the PSF, the authors proposed computing the normalized logarithm of the Fourier transform of a degraded image and producing a binary transform matrix using an edge function, as described in equations (27) and (28), respectively. The method estimates the support parameter of Gaussian and uniform blur kernels by calculating the number of feature lines in the binary feature matrix, where each feature line has a pixel value of 1. The article discusses recognizing the feature lines in each row and column using a positive integer number (e.g., half of the image size). When the number of pixel values equal to 1 exceeds this positive integer, they consider this row or column to be a feature line.

$$(\log(|Y|))_{normalized} = \frac{\log(|Y|) - \log(|Y_{min}|)}{\log(|Y_{max}|) - \log(|Y_{min}|)} \tag{27}$$

$$J = edge((\log(|Y|))_{normalized}) \tag{28}$$

After estimating the PSF support size, Huang et al. proposed a PSF type identification method that uses a dictionary learning-based approach. The method combines the logarithmic power spectrum [43], log-Gabor filter [44], and feature similarity index [45] to identify the best structural similarity between observed and dictionary images. The dictionary library contains original images and PSFs, and the proposed algorithm computes the gradient magnitude and phase correspondence matrix of the images. Finally, the algorithm uses the feature similarity index (FSIM) to identify the best structural similarity between observed and dictionary images.

In the second stage, the proposed method restores the image using the estimated PSF. To achieve this, the method utilizes a CNN-based image restoration module that takes the input blurred image and the estimated PSF and produces the restored image. The image restoration module is based on a deep learning architecture that employs a CNN with skip connections. These skip connections help to preserve the image details and reduce artifacts. The cost function used in [42] is as follows:

$$C(f) = \|h_E * f - g\|_2^2 + \boldsymbol{\lambda}\, \Phi(f) \tag{29}$$

Where $\Phi(f)$ is the regularization term and $\lambda > 0$ is the regularization parameter. Subsequently, the solution of (29) is used as an input to the CNN to minimize the loss function of the residual image, given by:

$$l(\Theta) = \frac{1}{2N} \sum_{i=1} \|\mathrm{Z}_\Theta(g_i) - (g_i - f_i)\|_2^2 \tag{30}$$

Here, g_i and f_i represent the blur and the restored patch pairs. Z_Θ represents the image generator network, and Θ denotes the network parameter optimized using ADAM [46].

The proposed CNN-based method requires predefined parameters, including the patch size of 64×64 for both PSF and image restoration phases. The network architecture of the PSF estimation phase consists of 15 convolutional layers and a regression layer, while that of the image restoration phase includes 16 convolutional layers with skip connection. The CNN-based approach is trained using stochastic gradient descent (SGD) with a batch size of 16, a momentum of 0.9, and weight decay of 0.0001. The learning rate

is initialized to 0.001 and reduced by a factor of 10 after 100 epochs, with a total of 200 epochs for training. It should be noted that these parameter values are specific to the training dataset used.

Method 9: Zhang

Lei Zhang et al. proposed in [47] a method for hyperspectral image super-resolution restoration that uses a deep learning approach. The proposed method aims to enhance the spatial resolution of a hyperspectral image by learning a mapping function from a low-resolution hyperspectral image to a high-resolution hyperspectral image.

The method consists of two main stages: a deep feature extraction stage and a deep regression stage. In the first stage, a convolutional neural network (CNN) is used to extract deep features from the low-resolution hyperspectral image. These features are then fed into a fully connected layer that maps them capturing the underlying spatial and spectral information of the input image. The output of this stage is a set of high-dimensional features. In the second stage, another CNN is used to regress the high-resolution hyperspectral image from the high-dimensional features obtained in the first stage. The network is trained in a supervised manner using a dataset of paired low and high resolution hyperspectral images.

A 3-D hyperspectral image is transformed into a 2-D matrix **Z**, where each column of this matrix represents a spectrum vector of a pixel. The correlation between the matrix **Z** with an HR MSI **X** and an LR HSI **Y** is formulated as follows:

$$X = PZ, \qquad Y = ZH \tag{31}$$

Where X and Y are the HR MSI and the LR HSI, respectively. P and H are the degradation function in the spectral and spatial domains.

The proposed cost function for the deep framework is formulated as follows:

$$C(\theta, P, H) = \|X - PZ\|^2 + \|Y - (ZH)\downarrow_s\|^2 + \boldsymbol{\lambda}\,(\|H\|_2^2 + \|P\|_2^2) \tag{32}$$
$$\text{s.t. } Z = \mathcal{F}_{\Theta}(E)$$

λ is the regularization parameter that weights the PSF regularization term in both spatial and spectral domains, $\downarrow_s$ indicates the downsampling with a scaling factor of s, and $\mathcal{F}_{\Theta}(.)$ is the image generator network for the latent image $\boldsymbol{Z}$, and $\boldsymbol{E}$ is the precomputed code for the input of $\mathcal{F}_{\Theta}$.

The proposed image generator network is developed to model image $\boldsymbol{Z}$ by highlighting the image-specific statistics based on images $\boldsymbol{X}$ and $\boldsymbol{Y}$. To accomplish this, two up-sampling subnetworks $g_{\theta_h}^h$ and $g_{\theta_p}^p$ were trained to increase the spatial resolution of $\boldsymbol{Y}$ and the spectral resolution of $\boldsymbol{X}$, respectively, to match a latent HSI $\boldsymbol{Z}$.

The Paired image patches $\{\hat{x}_i, x_i\}$ and $\{\hat{x}_i, y_i\}$ are collected from the input HR MSI **X** and LR HSI **Y** to train the subnetworks. The paired patches were generated from **X** and **Y** using a predefined degeneration H' in the spatial domain. The patches $\hat{x}_i$ and x_i were used to train $g_{\theta_h}^h$, while the patches $\hat{x}_i$ and y_i were used to train $g_{\theta_p}^p$ as follows:

$$C(\theta_h) = \frac{1}{N_h}\sum_{i=1}\mathcal{L}(x_i, x_i'), \qquad \text{s.t. } x_i' = g_{\theta_h}^{h}(\hat{x}_i) \tag{33}$$

$$C(\theta_p) = \frac{1}{N_p}\sum_{i=1}\mathcal{L}(y_i, y_i'), \qquad \text{s.t. } y_i' = g_{\theta_p}^{p}(\hat{x}_i) \tag{34}$$

The number of training pairs used for training $g_{\theta_h}^{h}$ and $g_{\theta_p}^{p}$ is N_h and N_p, respectively. $\mathcal{L}(.)$ represents the L_1 norm loss.

Finally, the image-dependent code $\boldsymbol{E}$ is as follows:

$$E = \alpha g_{\theta_h}^{h}(X) + (1-\alpha) g_{\theta_p}^{p}(Y) \tag{35}$$

Where α is a predefined regulation parameter for the two sub-networks.

The method proposed by L. Zhang et al requires fixing certain parameters, including the learning rate of the used ADAM optimizer [46] fixed at 0.001, along with the two regularization parameters $\lambda = 0.0005$ and $\alpha = 0.8$. These fixed parameters make the method parametric and non-blind, relying on subjective parameter choices for image restoration.

4. Conclusion

In this chapter, we have focused on nine image restoration methods, highlighting their distinctive characteristics. These methods adopt regularization terms that preserve the sparsity of edges in the image and incorporate specific constraints on the PSF, such as being non-negative and summing up to one. The selection of these nine methods represents a variety of implementation and regularization term formalization found in the literature for image restoration and PSF estimation.

These methods either perform alternating minimization of the multi-term cost function with respect to both the original image and PSF (which are assumed to be spatially invariant) or minimize a specific cost function for either the original component or PSF in a hybrid approach. Additionally, some methods use an image pyramid with different detail resolutions to avoid local minima.

In general, the objective of all nine analyzed methods is to achieve a solution with a sparse distribution of edges in the original image, and each method utilizes its own cost function formulation to accomplish this goal. However, for a user, it can be challenging to choose a specific method that yields meaningful results for a target application.

Furthermore, several drawbacks related to PSF estimation and image restoration arise due to the difficulty of formalizing adequate values for the parameters weighting the regularization terms. These parameter values significantly influence the restoration quality and, therefore, must be defined according to the expected characteristics of the sought solutions and meet the convergence requirements.

The main reason for this critical situation is that the restoration step must jointly meet multiple objectives, such as deblurring with texture and detail preservation, while also allowing user exploration for various application domains. For instance, the manual tuning of the regularization parameter values used in the

optimization functions is a complex process that does not guarantee reliable and relevant processing to meets these objectives.

To facilitate the application of a restoration method when the prior knowledge is limited or non-existent, an adaptive and optimized blind method is the most appropriate solution. Based on a study by M. Zhang et al [48][49], conducted objectively and subjectively to assess the estimation accuracy of the impulse response of the blur and the original image, we will evaluate the influence of the regularization parameters related to the PSF and original image estimation for [26]. This evaluation aims to demonstrate the importance of automatic estimation of these regularization parameters.

Chapter 2: Influence of the regularization parameters over the restoration quality

1. Introduction

In this chapter, a study is conducted to assess the influence of the predefined regularization parameter values in PAN's method [26] on the image restoration quality. The aim of this study is to demonstrate that automatically estimating the regularization parameter values related to the PSF estimation and the original image restoration is preferable to fixing them manually by the user. Automatic estimation of the regularization parameters provides adaptive values for different blur types, specific for each degraded image.

PAN method [26] was selected for a comparative study [48][49] among five semi-blind methods [20][21][23][26][50], conducted on a dataset of monochrome, multi-component, and hyperspectral images. These images were degraded by a defocus PSF with a support of 5x5 and 9x9. The evaluation criterion used was the L_1 norm of the estimation error. The results showed that the ranking of the methods depends on the PSF support, image type, and noise level. The method proposed by Pan et al. [26] performed the best overall, followed by ADMM [21], while Sroubek [23] had the worst performance. A complementary study showed that the ranking was similar for a linear motion degradation. Therefore, we performed an evaluation for the predefined regularization parameters in the method proposed in [26].

Before presenting the results of this study, we will review the main evaluation criteria and specify those used subsequently.

2. Evaluation criteria

In this section, we are interested in the main evaluation criteria used in the state-of-the-art, as describe in Chapter 1. Various objective metrics can be employed to reveal information about the nature and magnitude of the distortions, as well as the distribution of the errors. Multiple objective criteria exist for assessing the quality of both the estimated PSF $(\hat{h})$ and the restored image $(\hat{f})$. A restoration method is considered superior to another if it maximizes or minimizes a specific criterion.

When evaluating the quality of a restored image, subjective criteria can be linked to the characteristics of the human visual system [51]. A subjective evaluation of image quality requires conducting psycho-visual experiments, where panel of observers measures image quality under specific and identical environmental conditions. The established measurements allow for an estimation of the actual perceived quality. However, implementing such evaluations remains time-consuming and challenging.

As a result, objective quality evaluation has been proposed as an alternative solution, aiming to replacing subjective evaluation with a measurement tool that is correlated with human visual perception [51]. Objective criteria can be classified into two categories: non-blind (with reference) and blind (without reference) criteria. Non-blind criteria require complete knowledge of the original image, the PSF, or information about statistical noise parameters. They can be used regardless of the type of degradation. In contrast, blind criteria only utilize the degraded image as the available data. The main criteria for evaluating the image restoration quality or PSF are listed in the following subsection.

2.1. Non Blind criteria

To evaluate the quality of different restoration algorithms, several evaluation criteria have been defined, many of which can also be used to assess the quality of the estimated PSF. While some of these criteria are commonly employed, others are used less frequently.

- **Mean Bias and Variance of the estimation error**

The mean bias and variance of the estimation error are among the most commonly used metrics in estimation.

$$\text{Mean bias:} \quad E\left(f - \hat{f}\right)$$

$$\text{Variance:} \quad Var\left(f - \hat{f}\right)$$

- **L_1-norm of the estimation error**

This measure provides the actual overall difference between the original and restored images by calculating the direct sum of the absolute value of the error at each pixel over the entire image support. It is considered a reliable criterion, applicable regardless of whether the image is normalized or not.

$$\left\|f - \hat{f}\right\|_1 = \sum_i \sum_j \left|f(i,j) - \hat{f}(i,j)\right|$$

(i,j) is the position of each pixel in the original (f) and the restored $\left(\hat{f}\right)$ image.

- **Sum of Squared Difference (SSD)**

SSD, also known as the L_2 norm of the estimation error, measures the overall difference between the original and restored image by computing the square root of the sum of squared differences between corresponding pixels in the two images over the entire support of the image. This metric is also referred to as the Euclidean norm or the Root Mean Square (RMS) norm.

$$\left\|f - \hat{f}\right\|_2^2 = \sqrt{\left(\sum_i \sum_j \left|f(i,j) - \hat{f}(i,j)\right|^2\right)}$$

The summation is performed over the entire support of the image.

- **Mean Square Error (MSE)**

MSE is used to measure the quality of a restored image by computing the average of the squared differences between corresponding pixels in the original and restored images over the entire image support.

$$MSE = \frac{\sum_i \sum_j \left| f(i,j) - \hat{f}(i,j) \right|^2}{M \times N}$$

Where *M* and *N* represent the number of rows and columns of the image, respectively. This criterion was used by Sroubek [23] and Haoyuan [31] to evaluate the quality of restored images.

- **Normalized Squared Error (NSE)**

NSE is the normalized version of the MSE developed in [31].

$$NSE = \frac{\sum_i \sum_j \left| f(i,j) - \hat{f}(i,j) \right|^2}{\sum_i \sum_j |f(i,j)|^2}$$

- **Root Mean Square Error (RMSE)**

RMSE is another variation of the MSE. It is computed by taking the square root of the average of the squared differences between corresponding pixels in the original and restored images, over the entire support of the image. Deployed by Zhang et al. [47] to evaluate the obtained restored images.

$$RMSE = \sqrt{\frac{\sum_i \sum_j \left| f(i,j) - \hat{f}(i,j) \right|^2}{M \times N}}$$

- **Peak Signal to Noise Ratio (PSNR)**

PSNR is a commonly used metric for evaluating the quality of the restored image. It is defined as the ratio of the square of the maximum possible pixel value of the image to the mean squared error (MSE) between the original and restored images, expressed in decibels (dB) [52]. A higher PSNR value indicates a better quality restoration.

$$PSNR = 10 \times \log_{10} \left(\frac{(\max D)^2}{MSE} \right)$$

Where *D* is the full range pixel values (for 8-bit images *D*=255 and MSE is the mean squared error between the original and restored images.

- **Structure Similarity Index Measurement (SSIM)**

This criterion consists of three terms that allow detecting the changes in luminance $l(f, \hat{f})$, contrast $c(f, \hat{f})$, and local structure $s(f, \hat{f})$ between the original and restored image versions [53].

$$SSIM(f, \hat{f}) = l(f, \hat{f}) \times c(f, \hat{f}) \times s(f, \hat{f})$$

The two images are analyzed through a sliding window or decomposed into blocks of the same size. The three terms are then calculated in each of the windows or blocks and are defined as follows:

$$l(f,\hat{f}) = \frac{(2\mu_f\mu_{\hat{f}} + c1)}{(\mu_f^2 + \mu_{\hat{f}}^2 + c1)}$$

$$c(f,\hat{f}) = \frac{(2\sigma_f\sigma_{\hat{f}} + c2)}{(\sigma_f^2 + \sigma_{\hat{f}}^2 + c2)}$$

$$s(f,\hat{f}) = \frac{\sigma_{f\hat{f}}^2 + c_3}{\sigma_f\sigma_{\hat{f}} + c_3}$$

The constants C_1, C_2, and C_3 ensure the stability of the measurement in homogeneous areas. $C_1 = (0.01 \times L)^2$, $C_2 = (0.03 \times L)^2$, and $C_3 = \frac{C_2}{2}$, where $L = 2^{\#\, bits\ per\ pixel} - 1$. μ is the mean level, and σ is the standard deviation of the luminance in the analysis window ($\sigma_{f\hat{f}}^2$ represents the covariance between f and $\hat{f}$).

- **Signal to Noise Ratio (SNR)**

This metric measures the ratio of the image power to the noise power. It quantifies the level of the desired image relative to the background noise.

$$SNR = 10 \times \log_{10}\left(\frac{\sum_{i=1}^{N} f^2}{\left\|f - \hat{f}\right\|^2}\right)$$

Higher SNR values indicate a stronger restored image and better quality.

- **Improved Signal to Noise Ratio (ISNR)**

The authors proposed in [21] a new criterion for evaluating the quality of the restored image based on the signal-to-noise ratio, used by Huang et al. [42], defined as:

$$ISNR = 10 \times \log_{10}\left(\frac{\|f - g\|^2}{\left\|f - \hat{f}\right\|^2}\right)$$

- **Gradient Magnitude Similarity Deviation (GMSD)**

The quality of the image can be evaluated using the global variation of the local gradient [54]. The deviation of the gradient amplitude similarity between the original and estimated images is therefore introduced. The images are divided into P blocks of the same size. The gradient of the image in the horizontal and vertical directions is calculated using the Prewitt filter, such as:

$$h_x = \begin{bmatrix} 1/3 & 0 & -1/3 \\ 1/3 & 0 & -1/3 \\ 1/3 & 0 & -1/3 \end{bmatrix} \qquad h_y = \begin{bmatrix} 1/3 & 1/3 & 1/3 \\ 0 & 0 & 0 \\ -1/3 & -1/3 & -1/3 \end{bmatrix}$$

The amplitudes of the gradients of the original image and the estimated image on the i^{th} block is given by:

$$m_f(i) = \sqrt{(f * h_x)^2(i) + \left(f * h_y\right)^2(i)}$$

$$m_{\hat{f}}(i) = \sqrt{\left(\hat{f} * h_x\right)^2(i) + \left(\hat{f} * h_y\right)^2(i)}$$

The similarity of the amplitude of gradients (GMS) between the original and estimated image is expressed as follows:

$$GMS(i) = \frac{2m_f(i)m_{\hat{f}}(i) + c}{m_f^2(i) + m_{\hat{f}}^2(i) + c}$$

Where c is a positive constant ensuring stability [54].

GMS only provides the local quality measure of the image. The global measure is obtained by averaging over the number of blocks.

$$GMSM = \frac{1}{P}\sum_{i=1}^{P} GMS(i)$$

Based on the idea that the variation of local quality in an image can reflect the overall quality of the image, the standard deviation of GMS is proposed as a final measure, such that:

$$GMSD = \sqrt{\frac{1}{P}\sum_{i=1}^{P}\left(GMS(i) - GMSM(i)\right)^2}$$

GMSD and GMS metrics are used by Huang et al. [42] to evaluate their proposed restoration method. The smaller the value of GMSD, the better the quality of the image.

- **Error ratio**

The Error ratio, also called SSD ratio, compares the square of the L_2 norm of the difference between the restored image and the ground truth image using the estimated PSF to the square of the L_2 norm of the difference between the image restored using the ground truth PSF and the ground truth image. It was first introduced by A. Levin [55] and subsequently used in [24][26][50][56][57][58].

$$Er = \frac{\left\|\hat{f}_r - f_{GT}\right\|_2^2}{\left\|\hat{f}_t - f_{GT}\right\|_2^2}$$

Here, $\hat{f}_r$ represents the restored image obtained using the estimated PSF, $\hat{f}_t$ represents the restored image obtained using the ground truth PSF, and f_{GT} represents the ground truth image.

➢ **Kernel Similarity (KS)**

The kernel similarity metric proposed in [59] and used by [60] is based on the normalized correlation coefficient between the estimated and ground truth PSF.

$$KS(h,\hat{h}) = \max_{\gamma} \frac{\sum_{\gamma} h(\gamma).\hat{h}(\tau+\gamma)}{\|h\|_2.\left\|\hat{h}\right\|_2}$$

The kernel similarity involves formula involves the known PSF h, the estimated PSF $\hat{h}$, the element coordinates τ, and the possible shift γ between the two PSFs.

2.2. Blind criteria

In practical and operational scenarios, measures without references are highly desirable as they enable quality assessment without any prior information about the original image. In this subsection, we will introduce the most frequently employed criteria.

➢ **The estimation error of the observation**

This criterion measures the difference between the degraded image and its estimated one. It quantifies how accurately the restoration method is able to estimate the PSF and restore the original image from the degraded observations.

$$\left\|g - \hat{h} * \hat{f}\right\|_p$$

Here L denotes the L_P norm. $\hat{h}$ and $\hat{f}$ denotes the estimated PSF and the restored image, respectively. Therefore, $\hat{h} * \hat{f}$ represents the estimated degraded image $\hat{g}$.

➢ **Whiteness measures**

The authors propose in [61] three evaluation criteria based on the whiteness measurement of the degraded image. The residual image (i.e., $g - \hat{h} * \hat{f}$) is first centered and reduced:

$$r = \frac{Ir - \overline{Ir}}{\sigma_r}$$

Where Ir is the residual image not normalized and $\overline{Ir}$ its mean value and σ_r its standard deviation. The first measure is based on the opposite of the estimated auto-covariance energy:

$$R(r) = -\sum_{\substack{(a_1,a_2)=(-U,-U) \\ (a_1,a_2)\neq(0,0)}}^{(U,U)} \left(R_{rr}(a_1,a_2)\right)^2$$

The purpose of introducing the minus sign is to make this measurement larger when the residual error is whiter. In the case of a white image, its autocovariance follows a Dirac distribution at zero. Typically, the autocovariance pattern shows a significant decrease regarding the original image [61].

Therefore, the authors of [61] suggest weighting the values of the estimated autocovariance with a Gaussian for the second measurement in order to give more weight to the values close to the origin in the previous measurement.

$$RG(r) = -C \sum_{\substack{(a_1,a_2)=(-U,-U) \\ (a_1,a_2)\neq(0,0)}}^{(U,U)} W(a_1,a_2)\big(R_{rr}(a_1,a_2)\big)^2$$

Where $U = 4$, $C > 1$ and $W(a_1,a_2)$ is the weighting matrix:

$$W(a_1,a_2) = \exp\big(-1.25(a_1^2 + a_2^2)\big)$$

Given that the autocorrelation of a white process is represented by a delta function, a white signal exhibits a uniform power spectral density. In order to evaluate this flatness, they suggested to quantify its Shannon entropy after normalization. It is important to note that a flat distribution achieves maximum entropy.

$$H(r) = -\sum_{(w,v)} \widetilde{S_{rr}}(w,v) \log \widetilde{S_{rr}}(w,v)$$

Where $\widetilde{S_{rr}}(w,v) = \frac{S_{rr}(w,v)}{\sum_{w',v'} S_{rr}(w',v')}$ and $S_{rr}(w,v)$ is the power spectral density of r at the frequency (w,v).

In all three cases, the residual image is not always spatially invariant. Hence, the authors suggest computing a local whiteness measure. The auto-covariance estimation is performed on blocks $b \times b$ measuring 9x9 with a 5-pixel overlap in both horizontal and vertical directions. Whiteness measurements are referred to as R_b, RG_b, and H_b. To obtain the overall measurement for each case, the local measurements are averaged solely for the blocks entirely contained within the image.

2.3. Conclusion

To assess restoration methods, various criteria are used to evaluate the estimation error. When evaluating the method performance, the choice of a criterion can significantly impact the preference for one method over another. While a method may be evaluated and validated by its authors using a specific criterion, it may receive a lower ranking when compared to another method that employs a different criterion. The search for reliable evaluation criteria is crucial in objectively determining method performance. One notable criterion is the L_1 norm of the estimation error, which gives a direct measurement without altering the difference between the restored image and its original version. Moreover, this criterion can be applied with and without reference.

3. Evaluation of PAN's method

The method proposed by PAN [26] was selected by a previous comparison study made by Zhang et al. [48]. In this section we are interested in evaluating the choice of the fixed regularization parameters related to the estimation of the PSF (α) and the latent image (β_{lat}) and the final image restoration (β).

In Table 1, we represent the cost functions used by PAN [26] to estimate the Point Spread function (PSF), the latent image f_{lat} and restore the final image. The regularization parameters α, β_{lat} and β are associated with the cost function used for PSF estimation, latent image estimation, and final image restoration, respectively.

Usage	Cost function	
PSF estimation	$C(h) = \| \nabla g - h * \nabla S \|_2^2 + \boldsymbol{\alpha} \| h \|_{0.5}^{0.5}$	(36)
Latent image estimation	$C(f_{lat}) = \| g - h_E * f_{lat} \|_2^2 + \boldsymbol{\beta_{lat}} \| \nabla f_{lat} \|_1$	(37)
Final image restoration	$C(f) = \| g - h_E * f \|_2^2 + \boldsymbol{\beta} \left(e^{-\|\nabla_x S\|_{0.8}} \times \|\nabla_x f\|_1 + e^{-\|\nabla_y S\|_{0.8}} \times \|\nabla_y f\|_1 \right)$	(38)

Table 1: Cost functions used by PAN [26] related to the estimation of the PSF, latent image and final image restoration

According to PAN's method, the regularization parameters α, β_{lat}, and β related to the estimation of the PSF, latent image and the final image restoration, respectively. These regularization parameters are empirically fixed to $(\alpha, \beta_{lat}, \beta) = (0.01, 0.005, 0.003)$ after a series of tests conducted by Pan et al.

Initially, the empirical choice of regularization parameters was assessed, emphasizing the complexity of determining manually the most suitable values for these regularization parameters. Additionally, the influence of each regularization parameter was individually evaluated to gain insights into their respective effects on image restoration quality.

Therefore, in the following we have evaluated the empirical choice of the regularization parameters fixed in the method developed by Pan et al [26]. Then an evaluation was conducted to assess the influence of each regularization parameter over the image restoration quality by first analyzing the influence of the regularization parameter α on image restoration quality while keeping the values of β_{lat} and β fixed. This allowed for a thorough examination of the specific impact of α on the restoration process. Similarly, the influence of the regularization parameter β_{lat} was investigated by fixing the values of α and β, enabling an isolated assessment of the effect of β_{lat} on the restoration quality. Furthermore, the influence of the regularization parameter β was examined while keeping α and β_{lat} fixed, shedding light on the specific contribution of β to the restoration process.

All these evaluations were conducted using two monochrome images "Bridge" and "Photo" artificially degraded by 3 different motion PSFs of different support sizes $13 \times 13, 19 \times 19$, and 23×23 from the dataset [62] shown in Table 2.

Furthermore, for each series of tests, the evaluation was conducted based on four evaluation criteria: Peak Signal to Noise Ratio (PSNR), Signal to Noise Ratio (SNR), Structure Similarity Index Measure (SSIM), the L_1 norm of the estimation error, and $E(L_1)$ the mean of the L_1 norm.

Monochrome images	Bridge		Photo
			
PSF	13 × 13	19 × 19	23 × 23
			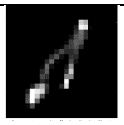

Table 2 : The two monochrome images in the evaluations and the three motion PSFs used to artificially degraded the images.

3.1. Evaluating the empirical choice of the regularization parameters fixed by PAN

The first evaluation aims to assess the fixed values of the regularization parameters α, β_{lat}, and β chosen by PAN. For this evaluation, ten different combinations of the regularization parameters were randomly selected from the range of $]0, 1]$. This assessment was performed on two monochrome images, namely "Bridge" and "Photo," using three different Point Spread Functions (PSFs) of sizes $13 \times 13, 19 \times 19$, and 23×23 from Table 2. The Test 1 – PAN, in Table 3, denotes the results using the chosen values for the regularization parameter in Pan's method $(\alpha, \beta_{lat}, \beta) = (0.01, 0.005, 0.003)$.

3.1.1. Evaluation using PSF of support size 13×13

In this subsection, we degraded the two monochrome images using a PSF of size 13×13 and restored them using ten different combinations for the regularization parameters α, β_{lat}, and β. The evaluation of the restored images based on the L_1 norm and SSIM is shown in Table 3.

Test	L_1 norm	SSIM	$\boldsymbol{\alpha}$	$\boldsymbol{\beta_{lat}}$	$\boldsymbol{\beta}$
« Bridge »					
Test 1 -PAN	3862.49	0.7175	0.01	0.005	0.003
Test 2	4402.19	0.5146	1	1	1
Test 3	**3108.20**	**0.8058**	**0.001**	**0.05**	**0.03**
Test 4	4259.14	0.5664	0.5	0.01	0.7
Test 5	3999.04	0.6035	0.5	0.5	0.5
Test 6	3660.91	0.6629	0.058	0.4	0.25
Test 7	3472.34	0.7024	0.75	0.3333	0.1429
Test 8	3270.76	0.7524	0.04	0.2	0.072
Test 9	3966.53	0.6115	0.9	0.001	0.4
Test 10	3979.53	0.6105	0.05	0.004	0.002
« Photo »					
Test 1 -PAN	1131.44	0.9356	0.01	0.005	0.003

Test 2	3251.25	0.6725	1	1	1
Test 3	1430.55	0.8738	0.001	0.05	0.03
Test 4	2861.10	0.7032	0.5	0.01	0.7
Test 5	2496.96	0.7343	0.5	0.5	0.5
Test 6	2035.28	0.7782	0.058	0.4	0.25
Test 7	1749.17	0.8134	0.75	0.3333	0.1429
Test 8	1541.09	0.8431	0.04	0.2	0.072
Test 9	2314.89	0.7561	0.9	0.001	0.4
Test 10	**1124.93**	**0.9360**	**0.05**	**0.004**	**0.002**

Table 3: Results of the evaluation criteria chosen for ten different combinations of the regularization parameters for PSF support size 13×13 using PAN's algorithm

As observed in Table 3, we noticed that for the "Bridge" image, we found a combination of regularization parameters that yielded superior results compared to those fixed by Pan et al. in terms of L_1 norm and SSIM. This particular combination, referred to as test 3 and denoted as $(\alpha, \beta_{lat}, \beta) = (0.001, 0.05, 0.03)$, achieved better outcomes. For example, using Pan's parameter values, we obtained an L_1norm of 3862.49 and an SSIM of 0.7175 dB. On the other hand, using the combination from test 3, the performance is improved, resulted in an L_1norm of 3108.2 and an SSIM of 0.8058 dB.

Furthermore, for the "Photo" image, the combination suggested in test 10 of Table 3, $(\alpha, \beta_{lat}, \beta) = (0.05, 0.004, 0.002)$, outperformed the proposed combination by Pan et al., $(\alpha, \beta_{lat}, \beta) = (0.01, 0.005, 0.003)$, based on the evaluation criteria used in this study. Upon examining the results in Table 3, we can see that using Pan's parameter values for the restoration of the "Photo" image yielded an L_1norm of 1131.44 and an SSIM of 0.9356 dB. Conversely, when employing the parameter values from test 10, we obtained an L_1norm of 1124.93 and SSIM of 0.9360 dB. In this case, performance is enhanced.

Comparisons using other selected evaluation criteria (PSNR, SNR, $E(L_1)$ norm, and MSE) yielded the same results obtained above, see appendix.

Table 4 shows a visual comparison, in addition to numerical evaluation, between the original images ("Bridge" and "Photo") and the restored images the restoration was performed using specific regularization parameters set for Test 1 – PAN, Test 2 (worst results), and Test 3 (best result) form the "Bridge" image and Test 2 (worst result), Test 10 (best result) for the "Photo" image. We can notice that there is not much difference when evaluating visually the restoration results for both images.

	Original image	Restored image		
		Test 1 – PAN	Test 2	Test 3
“ Bridge”				
		Test 1 – PAN	Test 2	Test 10
“ Photo”				

Table 4: visual comparison between the original images (“Bridge” and “Photo”) and the restored images the restoration was performed using specific regularization parameters set for Test 1 – PAN, Test 2 and Test 3 form the “Bridge” image and Test 2 and Test 10 for the “Photo” image degraded by the PSF od support size 13×13.

Figures 1-3 represent the plot of the variation of the PSNR, SNR, $E(L_1)$ norm, and SSIM for both “Bridge” and “Photo” images.

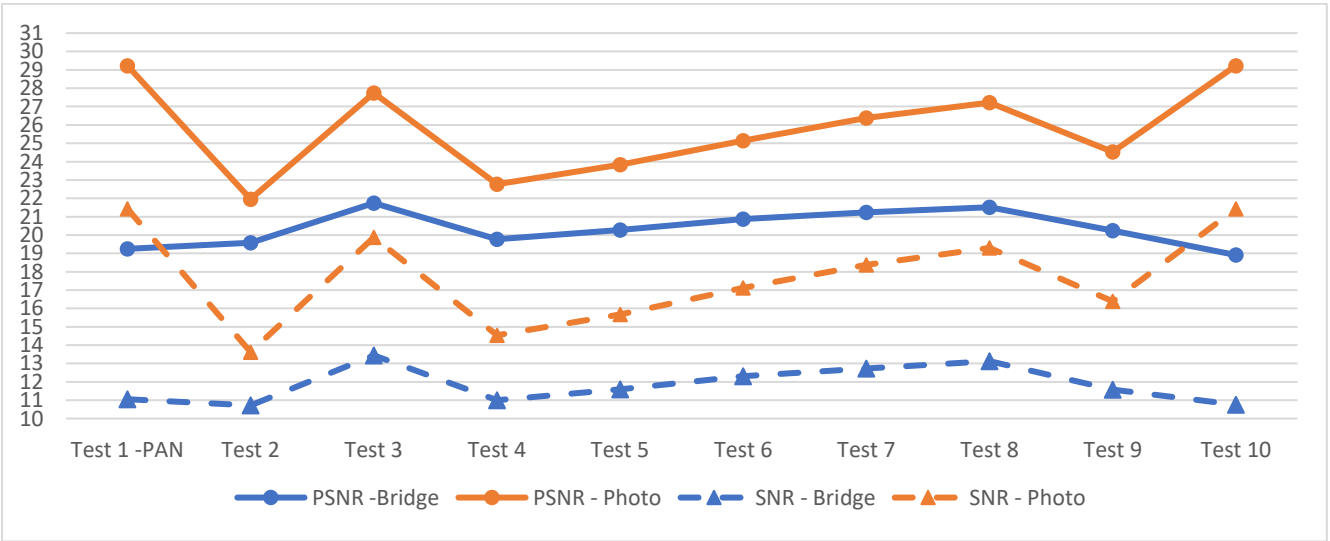

Figure 1: PSNR and SNR variation using ten different regularization parameters combinations for the "Bridge" and "Photo" images, with PSF support size 13×13

Figure 2: $E(L_1)$ norm variation using ten different regularization parameters combinations for the "Bridge" and "Photo" images, with PSF support size 13×13

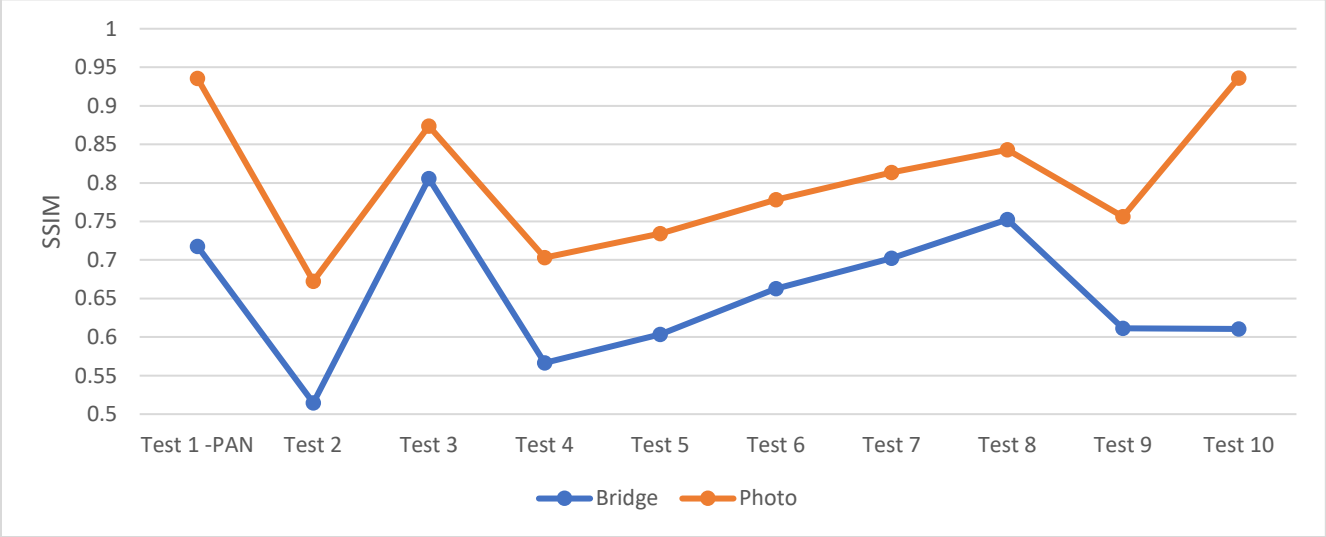

Figure 3: SSIM variation using ten different regularization parameters combinations for the "Bridge" and "Photo" images, with PSF support size 13×13

Based on Table 3, Table 4, and Figures 1-3, we can observe that when applying the same degradation function (PSF of support size 13×13) to two different monochrome images, the combination of regularization parameters that yielded the best result for the "Bridge" image, as shown in Table 3, differs from the one that produced the best result for the "Photo" image.

The results obtained for the PSF of support size 19×19 and 23×23 confirm the results shown for the PSF of support size 13×13. The details are these bigger PSFs are shown in Appendix.

3.1.2. Conclusion

In this section, a series of tests were conducted on Pan's algorithm, utilizing ten random combinations of the regularization parameters α, β_{lat}, and β. These parameters are associated with the estimation of the PSF, latent image, and final image restoration, respectively. The tests involved two monochrome images and three PSFs with different support sizes. The quality of image restoration using these parameter combinations was assessed by calculating the metrics of PSNR, SNR, $E(L_1)$ norm, L_1 norm, MSE, and SSIM.

As a result, it was observed that certain combinations of regularization parameters outperformed the fixed values proposed by Pan et al., based on the aforementioned evaluation metrics. This suggests that the fixed values are not optimal and do not yield optimal image restoration quality. The specific parameter combinations yielding better results based on a manual adjustment are presented in Table 5.

PSF size	Test	PSNR	SNR	$E(L_1)$ norm	L_1 norm	MSE	SSIM	$\boldsymbol{\alpha}$	$\boldsymbol{\beta_{lat}}$	$\boldsymbol{\beta}$
"Bridge"										
13 × 13	Test 3	21.7414	13.4455	0.0478	3108.20	0.0048	0.8058	**0.001**	**0.05**	**0.03**
19 × 19	Test 1	21.0529	12.8807	0.0498	3238.25	0.0056	0.8257	**0.01**	**0.005**	**0.003**
23 × 23	Test 9	17.4117	8.3865	0.0895	5819.74	0.0129	0.4388	**0.9**	**0.001**	**0.4**
"Photo"										
13 × 13	Test 10	29.2307	21.4301	0.0173	1124.93	0.0009	0.9360	**0.05**	**0.004**	**0.002**
19 × 19	Test 10	27.6787	19.9342	0.0205	1333.01	0.0013	0.9012	**0.05**	**0.004**	**0.002**
23 × 23	Test 6	20.4484	12.2344	0.0548	3563.37	0.0071	0.6331	**0.058**	**0.4**	**0.25**

Table 5: Summary of the tests achieved for the two monochrome images using three different PSFs of different support sizes

3.2. Evaluating the influence of each regularization parameter over the image restoration quality

In this section, we evaluated the influence of each regularization parameter α, β_{lat}, and β over the image restoration quality. For these evaluations, we used the same evaluation criteria mentioned before: PSNR, SNR, SSIM, $E(L_1)$ norm, L_1 norm, and MSE.

To evaluate each parameter alone, we need to fix two parameters and varying the other with a step size of 0.05. We took the regularization parameter values from Table 5 which yielded better results than the others.

Additionally, for this evaluation, we have used the image "Bridge" and "Photo" with the same PSFs used before (13 × 13, 19 × 19, and 23 × 23).

3.2.1. Evaluation using PSF of support size 13x13

Here, we are evaluating the influence of the regularization parameters α, β_{lat}, and β over the image restoration quality using a PSF of support size 13 × 13 for two image "Bridge" and "Photo".

3.2.1.1. *Evaluating the influence of the regularization parameter α over the restoration quality by fixing β_{lat} and β*

To evaluate the influence of the regularization parameter α related to the PSF estimation, we fixed β_{lat} and β , then varied α within the range $]0, 1]$ with a step size of 0.05.

Table 6 demonstrates the impact of the regularization parameter α on the PSF of support size 13×13 using five evaluation metrics. For the "Bridge" image, $\beta_{lat} = 0.05$ and $\beta = 0.03$ are fixed, whereas for the "Photo" image, $\beta_{lat} = 0.004$ and $\beta = 0.002$.

Test	L_1 norm	SSIM	$\boldsymbol{\alpha}$
« Bridge »			
Test 1	3108.20	**0.8058**	0.001
Test 2	3127.70	0.8027	0.05
Test 3	3127.70	0.8024	0.1
Test 4	**3108.20**	0.8054	**0.15**
Test 5	3127.70	0.8001	0.2
Test 6	3134.21	0.7999	0.25
Test 7	3134.21	0.7975	0.3
Test 8	3147.21	0.7944	0.35
Test 9	3153.71	0.7931	0.4
Test 10	3173.22	0.7885	0.45
Test 11	3173.22	0.7875	0.5
Test 12	3179.72	0.7857	0.55
Test 13	3186.23	0.7833	0.6
Test 14	3199.23	0.7811	0.65
Test 15	3212.24	0.7785	0.7
Test 16	3218.74	0.7763	0.75
Test 17	3225.24	0.7752	0.8
Test 18	3225.24	0.7735	0.85
Test 19	3238.25	0.7716	0.9
Test 20	3244.75	0.7691	0.95
Test 21	3257.75	0.7670	0.99
	« Photo »		
Test 1	1189.96	0.9345	0.001
Test 2	1111.93	0.9396	0.05
Test 3	1085.92	0.9405	0.1
Test 4	1072.91	0.9408	0.15
Test 5	1059.91	0.9409	0.2
Test 6	**1053.41**	**0.9414**	**0.25**
Test 7	1059.91	0.9397	0.3
Test 8	1059.91	0.9392	0.35
Test 9	1098.92	0.9351	0.4
Test 10	1105.43	0.9332	0.45
Test 11	1157.45	0.9277	0.5

Test 12	1124.93	0.9307	0.55
Test 13	1215.97	0.9207	0.6
Test 14	1254.98	0.9161	0.65
Test 15	1326.51	0.9074	0.7
Test 16	1248.48	0.9156	0.75
Test 17	1320.01	0.9066	0.8
Test 18	1521.59	0.8817	0.85
Test 19	1424.05	0.8933	0.9
Test 20	1417.55	0.8935	0.95
Test 21	1645.13	0.8629	0.99

Table 6 : The effect of the regularization parameter α using the PSF of support size 13×13, where β_{lat}=0.05 and β=0.03 are fixed for the image "Bridge" and for the "photo" image $\beta_{lat} = 0.004$ and $\beta = 0.002$, while α increase by a step size of 0.05

Looking at Table 6, we observed that for the "Bridge" image, the combination $[\boldsymbol{\alpha}, \beta_{lat}, \beta] = [\mathbf{0.15}, 0.05, 0.03]$ yielded in the highest restored image quality among all 21 tests conducted. This particular combination outperformed the combination $(\alpha, \beta_{lat}, \beta) = (0.001, 0.05, 0.03)$ from Table 5 in terms of PSNR, SNR, $E(L_1)$ norm and MSE, except for the SSIM metric. On the other hand, for the "Photo" image, the highest values for all evaluation metrics were obtained with $\alpha = 0.25$, denoted in Test 6. The combination $(\alpha, \beta_{lat}, \beta) = (0.25, 0.004, 0.002)$ performed better than the result presented in Table 5. To see the results of the other selected evaluation criteria, refer to Appendix.

A graphical representation depicting the impact of the regularization parameter α on image restoration quality is shown in Figures 4-5. The combination $(\alpha, \beta_{lat}, \beta) = (\boldsymbol{\alpha}, 0.05, 0.3)$ and $(\alpha, \beta_{lat}, \beta) = (\boldsymbol{\alpha}, 0.004, 0.002)$ were used for the "Bridge" and "Photo" images, respectively.

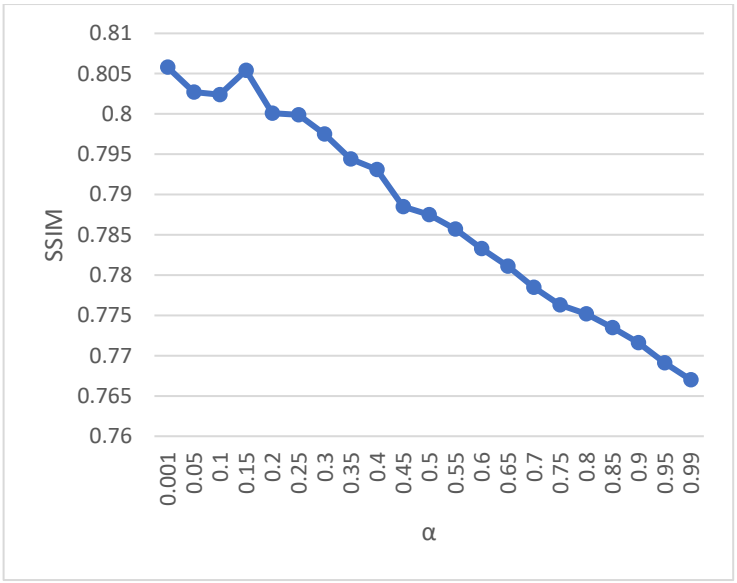

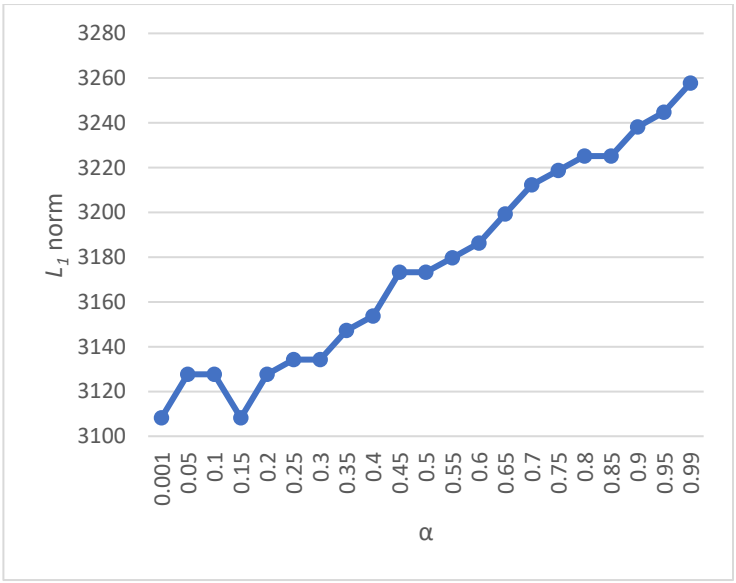

Figure 4: The effect of the regularization parameter α over the SSIM (left), L_1 norm (right) for the "Bridge" image using a PSF of support size 13x13 and fixing β_{lat}=0.05 and $\beta = 0.03$

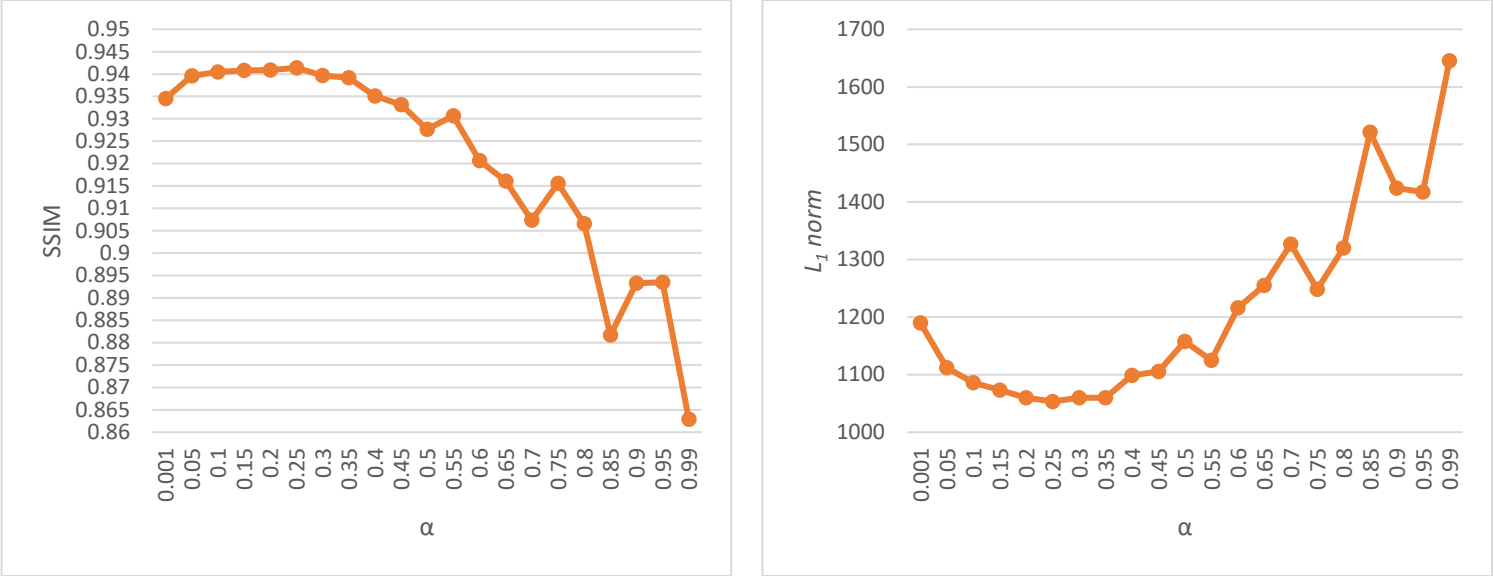

Figure 5: The effect of the regularization parameter α over the SSIM (left), and L_1 norm (right) for the "Photo" image using a PSF of support size 13x13 and fixing $\beta_{lat} = 0.004$ and $\beta = 0.002$

3.2.1.2. *Evaluating the influence of the regularization parameter β_{lat} over the restoration quality by fixing α and β*

In this subsection, we conducted an evaluation to assess the impact of the regularization parameter related to the latent image, β_{lat}, on the quality of the image restoration. To achieve this, we varied the value of β_{lat} within the range]0.1], using a step size 0.05. Additionally, we maintained the value of β as it was fixed in the previous subsection, with a value of 0.03 for the "Bridge" image and 0.002 for the "Photo" image. The fixed values of α are set to the values found in the previous subsection that provided better performance than Table 5. For the "Bridge" image, the fixed value of α was set to 0.15, while for the "Photo" image, α was set to 0.25.

Table 7 shows the results of the conducted evaluation based on five metrics L_1 norm and SSIM.

Test	L_1 norm	SSIM	β_{lat}
« Bridge »			
Test 1	3725.93	0.7050	0.001
Test 2	3108.20	0.8054	0.05
Test 3	3166.72	0.7936	0.1
Test 4	3179.72	0.7906	0.15
Test 5	3101.69	0.8019	0.2
Test 6	3134.21	0.7972	0.25
Test 7	3108.20	0.8004	0.3
Test 8	**3036.67**	**0.8099**	**0.35**
Test 9	3069.18	0.8048	0.4
Test 10	3108.20	0.7991	0.45
Test 11	3101.69	0.8007	0.5
Test 12	3101.69	0.7999	0.55

Test 13	3101.69	0.7999	0.6
Test 14	3121.20	0.7971	0.65
Test 15	3114.70	0.7985	0.7
Test 16	3127.70	0.7962	0.75
Test 17	3140.71	0.7949	0.8
Test 18	3127.70	0.7959	0.85
Test 19	3140.71	0.7947	0.9
Test 20	3121.20	0.7978	0.95
Test 21	3114.70	0.7985	0.99
« Photo »			
Test 1	**942.86**	**0.9492**	**0.001**
Test 2	1313.51	0.9192	0.05
Test 3	1450.06	0.9057	0.1
Test 4	1359.02	0.9148	0.15
Test 5	1326.51	0.9187	0.2
Test 6	1346.02	0.9174	0.25
Test 7	1359.02	0.9168	0.3
Test 8	1352.52	0.9180	0.35
Test 9	1437.05	0.9096	0.4
Test 10	1424.05	0.9111	0.45
Test 11	1508.58	0.9035	0.5
Test 12	1463.06	0.9074	0.55
Test 13	1528.09	0.9012	0.6
Test 14	1547.60	0.8994	0.65
Test 15	1567.10	0.8974	0.7
Test 16	1593.11	0.8951	0.75
Test 17	1606.12	0.8937	0.8
Test 18	1651.64	0.8898	0.85
Test 19	1677.65	0.8877	0.9
Test 20	1664.64	0.8891	0.95
Test 21	1658.14	0.8895	0.99

Table 7: The effect of the regularization parameter β_{lat} using the PSF of support size 13×13, where α=0.15 and β=0.03 are fixed for the image "Bridge" and for the "photo" image $\alpha = 0.25$ and $\beta = 0.002$, while β_{lat} increase by a step size of 0.05

By examining the results presented in Table 7, we can observe that for the "Bridge" image, the combination $[\alpha, \beta_{lat}, \beta] = [0.15, 0.35, 0.03]$ yielded a PSNR value of 0.8099 dB and an L_1 norm value of 3036.67 In comparison, the previous combination $[\alpha, \beta_{lat}, \beta] = [0.15,0.05,0.03]$ resulted in a SSIM value of 0.8054 dB and L_1 norm values of 3108.2. These findings indicate that the new combination led to superior restoration quality compared to the previous one.

Regarding the "Photo" image, it can be observed that the combination $(\alpha, \beta_{lat}, \beta) = (0.25,0.001,0.002)$ yielded an L_1 norm value of 942.86 and an SSIM value of 0.9492 dB. In contrast, the previous combination $(\alpha, \beta_{lat}, \beta) = (0.25,0.004,0.02)$ resulted in an L_1 norm value of 1054.41 dB and SSIM value of 0.9414 dB. Therefore, the new combination demonstrated better restoration quality than the previous one.

In addition to that, the other selected evaluation criteria confirm the results obtained above and presented in the Appendix.

Figures 6-7 illustrate the influence of the regularization parameter β_{lat} on the quality of image restoration. The combination $(\alpha, \beta_{lat}, \beta) = (0.15, \boldsymbol{\beta_{lat}}, 0.03)$ was used for the "Bridge" image, while $(\alpha, \boldsymbol{\beta_{lat}}, \beta) = (0.25, \boldsymbol{\beta_{lat}}, 0.002)$ was employed for the "Photo" image. Providing a visual insight into how different values of α impact the restoration quality for each respective image.

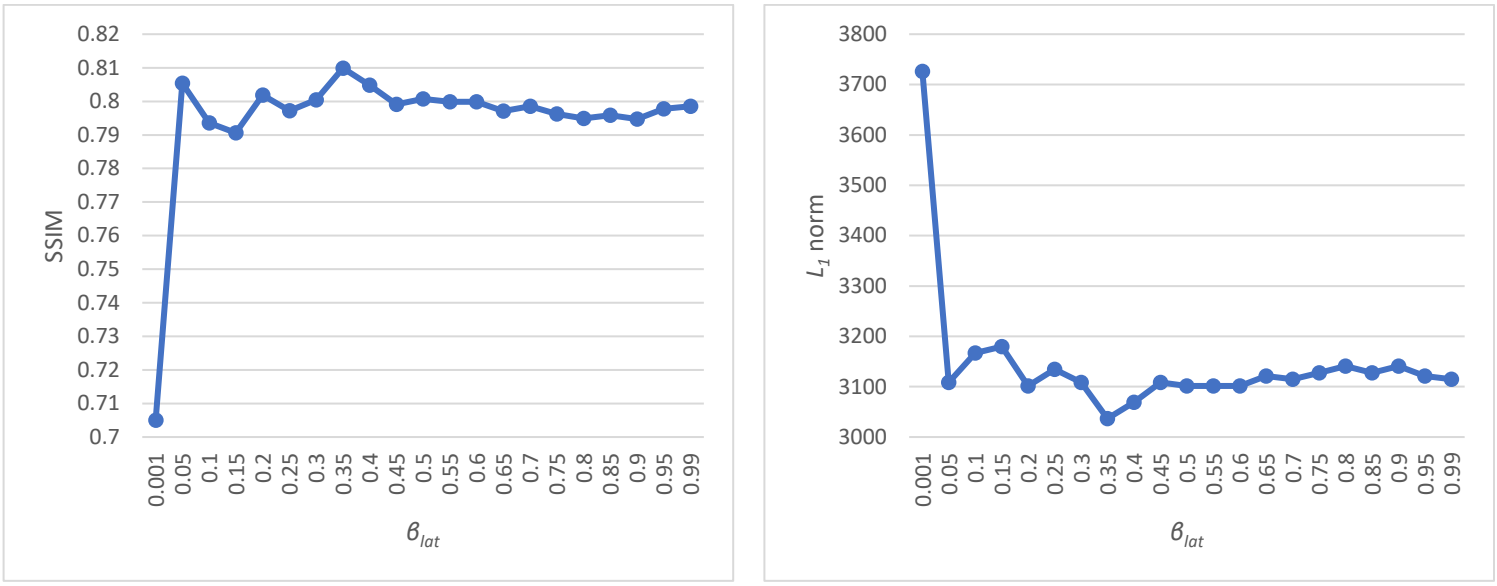

Figure 6: The effect of the regularization parameter α over the SSIM (left), and L_1 norm (right) for the "Bridge" image using a PSF of support size 13x13 and fixing $\alpha = 0.15$ and $\beta = 0.03$

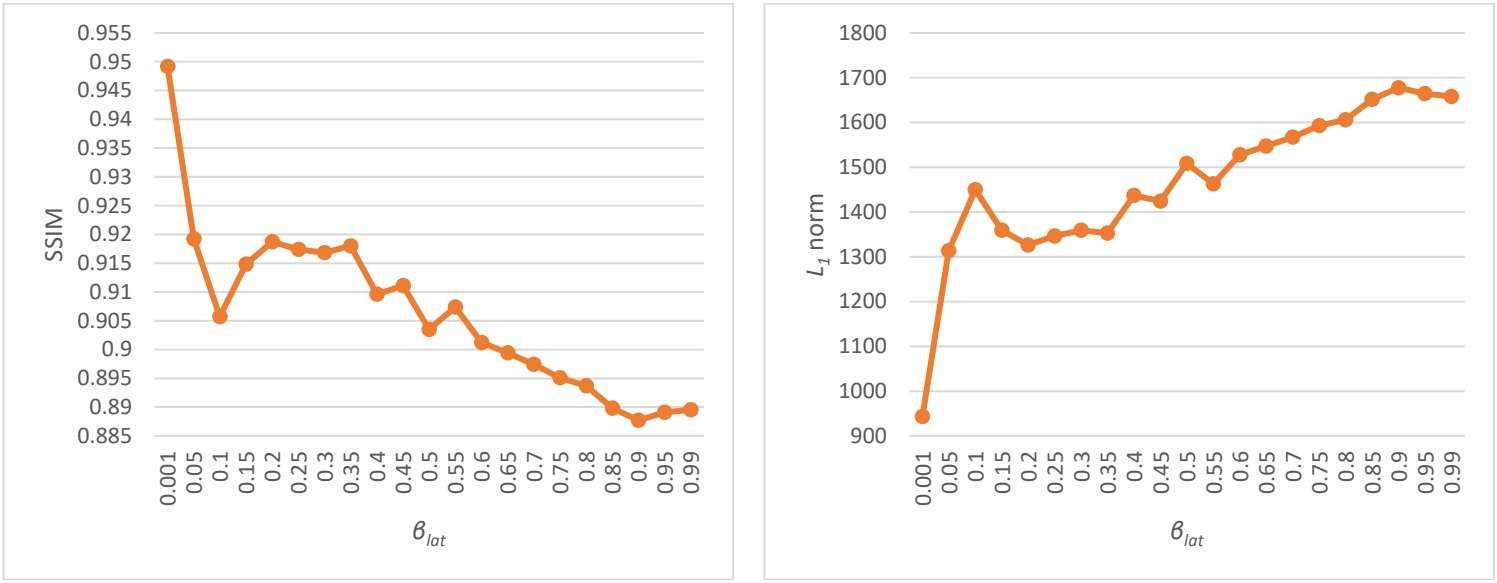

Figure 7 The effect of the regularization parameter α over the SSIM (left), and L_1 norm (right) for the "Photo" image using a PSF of support size 13x13 and fixing $\alpha = 0.25$ and $\beta = 0.002$

3.2.1.3. *Evaluating the influence of the regularization parameter β over the restoration quality by fixing β_{lat} and α*

After finding the value of α and β_{lat} that gave the best restoration quality based on the series of testes conducted in section 3.2.1.1. and 3.2.1.2. for both monochrome images "Bridge" and "Photo", we fixed these values to evaluate the influence of the regularization parameter β on the restoration quality of both images. For the restoration of the "Bridge" image, we fixed $\alpha = 0.15$ and $\beta_{lat} = 0.35$, while for the "Photo" image, $\alpha = 0.25$ and $\beta_{lat} = 0.001$. β varies in both cases in the rang]0,1] with a step size 0.05.

Table 8 presents the evaluation results obtained by varying the value of β for both the "Bridge" and "Photo" images. This table provides a comprehensive overview of the performance and quality achieved in the restoration process as β was systematically adjusted.

Test	L_1 norm	SSIM	$\boldsymbol{\beta}$
« Bridge »			
Test 1	3361.79	0.8215	0.001
Test 2	**3127.70**	**0.8267**	**0.05**
Test 3	3296.77	0.7371	0.1
Test 4	3433.32	0.7074	0.15
Test 5	3537.36	0.6848	0.2
Test 6	3634.90	0.6663	0.25
Test 7	3719.43	0.6507	0.3
Test 8	3797.46	0.6370	0.35
Test 9	3868.99	0.6250	0.4
Test 10	3934.01	0.6142	0.45
Test 11	3992.54	0.6046	0.5
Test 12	4044.56	0.5958	0.55
Test 13	4096.58	0.5877	0.6
Test 14	4142.09	0.5803	0.65
Test 15	4187.61	0.5734	0.7
Test 16	4226.63	0.5671	0.75
Test 17	4265.64	0.5611	0.8
Test 18	4304.66	0.5555	0.85
Test 19	4337.17	0.5503	0.9
Test 20	4369.68	0.5454	0.95
Test 21	4402.19	0.5416	0.99
« Photo »			
Test 1	**981.88**	**0.9504**	**0.001**
Test 2	1326.51	0.8684	0.05
Test 3	1554.10	0.8369	0.1
Test 4	1716.66	0.8160	0.15
Test 5	1859.72	0.7999	0.2
Test 6	1983.26	0.7865	0.25
Test 7	2093.81	0.7748	0.3
Test 8	2197.85	0.7644	0.35

Test 9	2295.38	0.7550	0.4
Test 10	2386.42	0.7462	0.45
Test 11	2477.45	0.7382	0.5
Test 12	2555.48	0.7306	0.55
Test 13	2640.02	0.7235	0.6
Test 14	2711.54	0.7168	0.65
Test 15	2789.57	0.7105	0.7
Test 16	2854.60	0.7044	0.75
Test 17	2926.13	0.6987	0.8
Test 18	2991.15	0.6932	0.85
Test 19	3056.18	0.6879	0.9
Test 20	3121.20	0.6829	0.95
Test 21	3166.72	0.6790	0.99

Table 8 : The effect of the regularization parameter β using the PSF of support size 13×13, where α=0.15 and β_{lat}=0.35 are fixed for the image "Bridge" and for the "photo" image $\alpha = 0.25$ and $\beta_{lat} = 0.001$, while β increase by a step size of 0.05

Upon analyzing the results presented in Table 8, it is evident that for the "Bridge" image, the combination $(\alpha, \beta_{lat}, \beta) = (0.15,0.35,0.05)$ yielded the best result among the 21 tests conducted. When comparing it with the previous combination $(\alpha, \beta_{lat}, \beta) = (0.15,0.35,0.03)$, we obtained better results with this latter. For example, the combination $(\alpha, \beta_{lat}, \beta) = (0.15,0.35,0.05)$ gave an SSIM value of 0.8267 dB and L_1 norm value of 3127.70. Conversely, the previous combination $(\alpha, \beta_{lat}, \beta) = (0.15,0.35,0.03)$ resulted in an SSIM value of 0.8099 dB and L_1 norm value of 3036.67. Therefore, the best combination remains the previous one $(\alpha, \beta_{lat}, \beta) = (0.15,0.35,0.03)$.

Regarding the "Photo" image, it can be observed that the combination $(\alpha, \beta_{lat}, \beta) = (0.25,0.001,0.001)$ yielded an SSIM value of 0.9492 dB and an L_1 norm value of 942.86. In contrast, the previous combination $(\alpha, \beta_{lat}, \beta) = (0.25,0.001,0.002)$ yielded an SSIM value of 0.9504 dB and an L_1 norm value of 981.88. Therefore, the previous combination demonstrated better restoration quality than the current one.

Furthermore, Figures 8-9 visually illustrate the impact of the regularization parameter β on the image restoration quality.

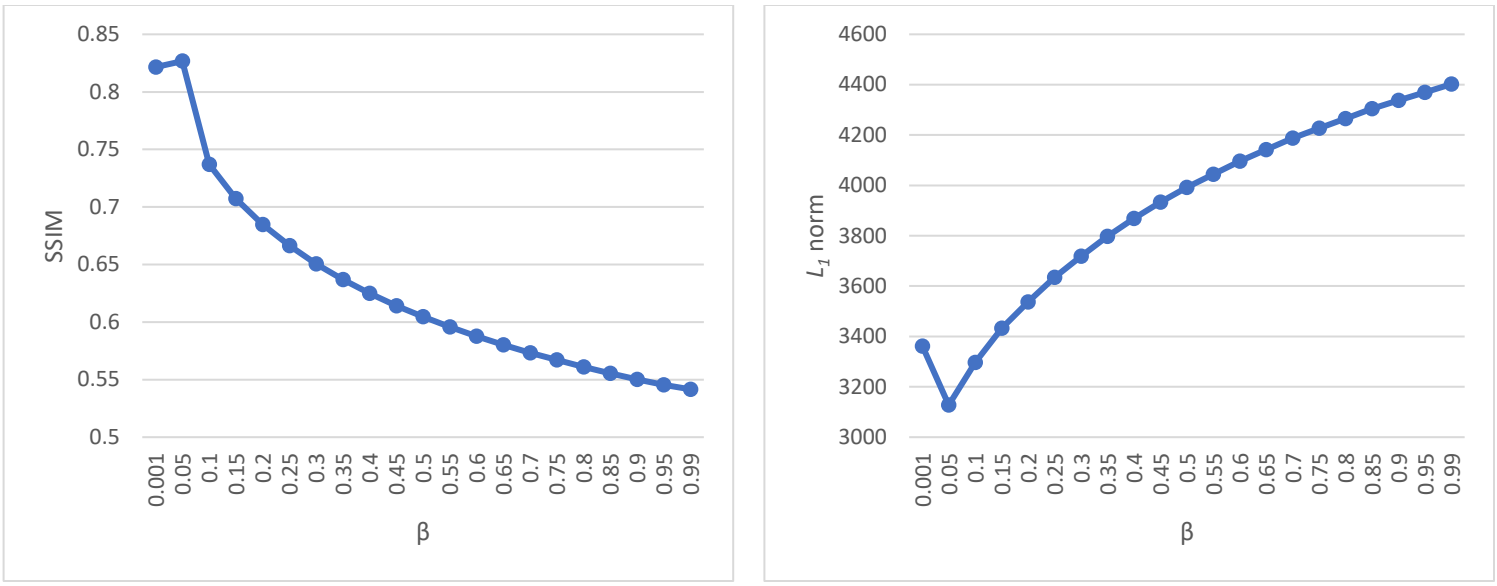

Figure 8: The effect of the regularization parameter β over the SSIM (left), and L_1 norm (right) for the "Bridge" image using a PSF of support size 13x13 and fixing $\alpha = 0.15$ and $\beta_{lat} = 0.35$

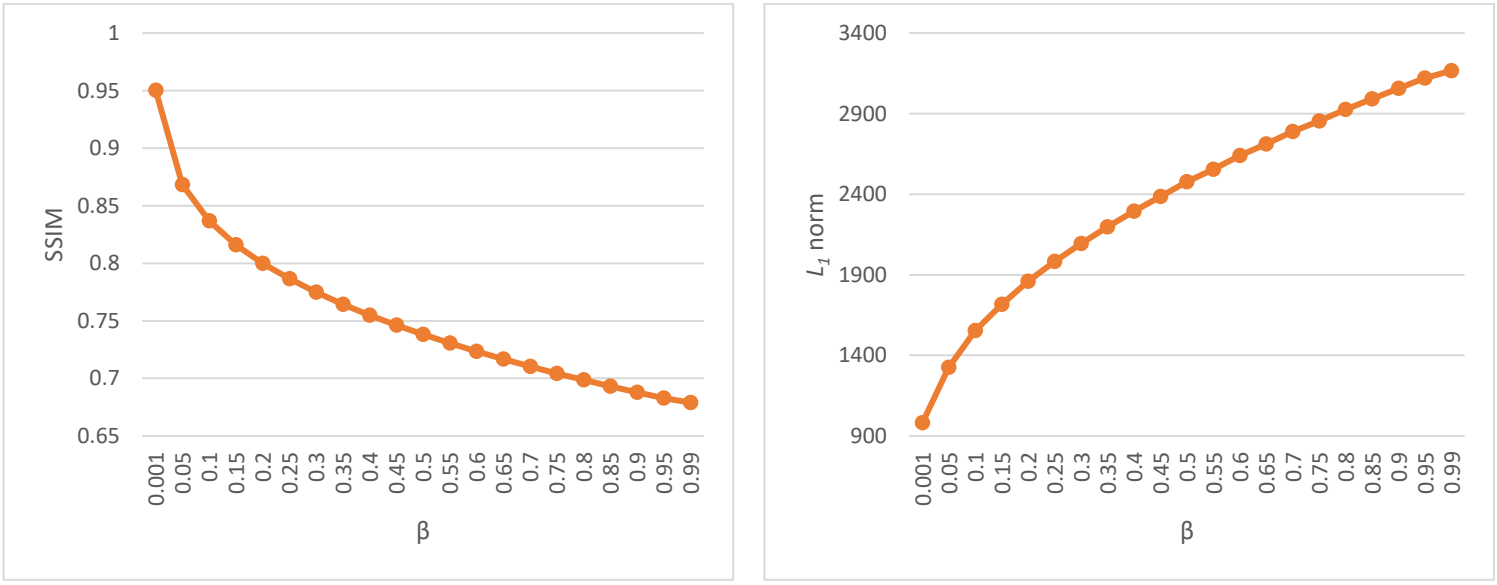

Figure 9: The effect of the regularization parameter β over the SSIM (left), and L_1 norm (right) for the "Photo" image using a PSF of support size 13x13 and fixing $\alpha = 0.25$ and $\beta_{lat} = 0.001$

After separately evaluations of the influence of each regularization parameter value α, β_{lat}, and β, related to the estimation of the PSF, latent image, and final image restoration, respectively, we have found the combinations $(\alpha, \beta_{lat}, \beta) = (0.15,0.35,0.03)$ and $(\alpha, \beta_{lat}, \beta) = (0.25,0.001,0.001)$ for the "Bridge" and "Photo" images, respectively, resulting in superior restoration quality compared to the fixed parameters used by Pan et al. $(\alpha, \beta_{lat}, \beta) = (0.01,0.005,0.003)$. These evaluations were conducted on two monochrome images, "Bridge" and "Photo", which were artificially degraded by a PSF with a support size of 13×13.

The results of the evaluation using the PSF of support size 19×19 and 23×23 confirm the same outcome as the PSF of support size 13×13. These results are shown in Appendix.

4. Conclusion

In conclusion, the evaluation of restoration methods involves the use of various criteria to assess the estimation error. The choice of a criterion can significantly impact the preference for one method over another, highlighting the importance of reliable evaluation criteria for objective performance assessment. The L_1 norm emerges as a notable criterion that provides a direct measurement of the difference between the restored image and the original, applicable both with and without reference.

Furthermore, the evaluation of Pan's algorithm using different combinations of regularization parameters revealed that certain parameter combinations outperformed the fixed values proposed by Pan et al. This indicates that the fixed values are suboptimal and do not yield the highest image restoration quality. Through the analysis of metrics such as PSNR, SNR, L_1 norm, MSE, and SSIM, it becomes evident that fine-tuning of parameters can lead to improved restoration outcomes.

Moreover, a comprehensive analysis of the influence of each regularization parameter over the restoration quality was conducted in order to find experimentally an optimal combination that yields the optimal solution. Table 9 shows the best combination found in this chapter that gave the highest restoration quality for both monochrome images used and degraded by three different PSF of different support sizes $(13 \times 13, 19 \times 19, 23 \times 23)$.

Table 10 presents a comparison between the restored "Bridge" and "Photo" images using the regularization parameter values found in Table 9, and the restored images using the fixed values of PAN. When examining the results for both images with the PSF of support size 13×13 in Table 10, it is evident that the newly combined parameter values result in higher visual quality for both "Bridges" and "Photo" images compared to PAN's combination.

Images	PSF size	Regularization parameters		
		$\boldsymbol{\alpha}$	$\boldsymbol{\beta_{lat}}$	$\boldsymbol{\beta}$
Bridge	13×13	0.15	0.35	0.03
	19×19	0.001	0.005	0.003
	23×23	0.4	0.1	0.35
Photo	13×13	0.25	0.001	0.002
	19×19	0.05	0.004	0.002
	23×23	0.001	0.4	0.05

Table 9: The best combination of regularization parameters found specific for each image degraded by each PSF

Image	Restored image (new combination)	Restored image (PAN's combination
13 × 13		
"Bridge"		
"Photo"		
19 × 19		
"Bridge"		
"Photo"		
23 × 13		

"Bridge"		
"Photo"		

Table 10: visual comparison between the restored "Bridge" and "Photo" images using PAN's combination and the new better combination for the three PSFs sizes used 13×13, 19×19, *and* 23×23

As depicted in Table 9, each image and PSF combination shows a specific set of parameters that result in superior restoration quality. Conversely, the fixed combination proposed by PAN et al $(\alpha, \beta_{lat}, \beta) = (0.01, 0.005, 0.003)$ is applied to any PSF and image, leading to a suboptimal solution.

Moreover, experimentally determining the optimal combination for achieving the highest restoration quality is a daunting task, as it requires testing an enormous number of possible combinations, to cover the range of each regularization parameter. Consequently, such a task becomes nearly impossible to accomplish within a reasonable timeframe

Hence, to find the optimal combination, an automatic estimation of the regularization parameter values is necessary to achieve convergence of the cost functions associated with the PSF, latent image, and final image restoration. This topic will be explored in detail in the upcoming chapter.

List of tables

List of figures

Chapter 3: Developed blind method

1. Introduction

Based on the comparative study made by Mo Zhang et al. [48], the selected semi blind hybrid method proposed by Pan et al. relies on prior knowledge such as regularization parameter values, the number of iterations, the PSF support size, and more. Following the study conducted in the previous chapter over the proposed method by Pan et al., we highlighted on the influence of the regularization parameter α, β_{lat}, and β related to the estimation of the PSF, latent image and final image restoration, respectively, on the quality of the image restoration. We also emphasized the variability in the performance of this method based on the image to be restored, the support size of the degradation function and the choice of the regularization parameter values. All of these challenges make it more difficult to appropriately choose a combination yielding the optimal result. This difficulty is further amplified by the empirical and manual selection of the regularization parameter values.

In order to address these limitations and drawbacks, this chapter focuses on the development of a blind restoration method that eliminates the need for any prior knowledge. The goal is to design an approach that can restore images without relying on explicit information about regularization parameters, or specific characteristics of the degradation function.

By developing a blind restoration method, we aim to overcome the inherent challenges associated with traditional restoration techniques. These challenges include the reliance on pre-defined parameters, the variability in performance based on image types, and the subjective nature of regularization parameter selection. These difficulties make the selection of an appropriate restoration method a more complicated task.

To tackle these issues, our objective is to develop a method that can autonomously restore images by leveraging inherent structures and patterns within the image itself. By developing a blind restoration approach, we aim to reduce the reliance on empirical choices and facilitate the restoration process.

Before presenting the proposed solutions to achieve this objective, we first highlight the challenges inherent to the problem of blind restoration.

The Challenges of Blind restoration

Our objective is to estimate both the PSF (h) and the original image (f) only from the observation image (g), without any prior knowledge. To minimize the reliance on prior knowledge, we propose to developing a blind restoration method where the only required prior information is the PSF support size.

To achieve our goal, we will decompose the restoration problem into two sub-problems: first, the estimation of the PSF, and then the estimation of the original image, as suggested in most of the hybrid methods such as PAN [26] and Krishnan [50]. The estimation of the PSF is performed alternately by exploiting the edges of a latent image. Subsequently, the estimated PSF is used for restoring the desired original image. This method is defined as a hybrid approach.

By adopting this approach, we aim to minimize the prior knowledge required for blind restoration and focus on estimating both the PSF and the original image from the observed data only. This allows for a more reliable and robust restoration method that can adapt to different image characteristics and eliminate the need for explicit prior information except the PSF support size.

This chapter is divided into four sections. Given that the proposed method is based on the same principles as the PAN method (referred to as the original method throughout the manuscript), the first section provides a comprehensive overview of its various steps, highlighting the properties and characteristics of the selected solutions for the PSF and latent image estimation as well as the final image restoration.

The second section specifies the different enhancements proposed to the original method in order to improve the restoration results of the original monochrome image while reducing the required prior knowledge. It is assumed that the PSF support size is known, along with a noiseless observation model.

The third section denotes the two strategies proposed to restore a full hyperspectral image based on the developed blind method for monochrome images.

The fourth section represents the series of tests conducted to evaluated the performance of the proposed blind method proving its superiority over the original method as well as the recent proposed methods in the literature. These evaluations are conducted on diverse databases consisting of monochrome, multicomponent, and hyperspectral images. To degrade the images, different blur functions with different support sizes are employed.

2. Principle of the original method

In the comparative study [48] conducted by Zhang et al., the hybrid method developed by PAN et al. [26] yielded the most promising results. Implementing this method allows for accurate estimation of both the PSF and the latent image using regularized cost functions. In the context of this thesis, we pursued a similar approach, but with a primary objective of developing a blind method with improved performance compared to existing ones.

Additionally, the evaluation conducted in Chapter 2, pointed out the suboptimality of the manual fixation of the regularization parameter values $\alpha, \beta_{lat},$ and β related to the estimation of the PSF, the latent image, as well as the final image restoration, respectively. This emphasizes the importance of the automatic tuning of these parameters. Therefore, we first recall the principle of this semi-blind method.

In the method proposed in [26], it is assumed that the observation model is noise-free ($g = h * f$). This multi-scale method estimates the PSF and an intermediate latent image, f_{lat}, alternately. The estimated PSF is then used for restoring the original image. Table 11, provides a summary of the two main steps, namely the estimation of the PSF and the original image, and specifies the different empirical a priori knowledge set by the user.

The PSF is estimated by minimizing a cost function with three terms. The first two terms correspond to data fidelity in the horizontal and vertical gradient spaces, respectively, while the third term is based on

the sparsity assumption of the PSF. The latent image is estimated by minimizing a cost function with two terms.

<table>
<tr>
<td>

- **Alternated step: estimation of h and f_{lat}:**
  - **Structural and textural components separation:**

$$\frac{\mathbf{1}}{\mathbf{2}\ni_{s,t} \times e^{-\|r\|^{0.8}}} \times \|\boldsymbol{I_s} - \boldsymbol{f_{lat}}\|_2^2 + \|\boldsymbol{\nabla I_s}\|_2$$

where I_s is the structural part of f_{lat} and $r = \frac{\|\sum_\delta \nabla g\|_2}{\sum_\delta \|\nabla g\|_2 + 0.5}$ with δ a window of size 5×5.

$\ni_{s,t}$: regularization parameter for the separation of the structural components.

  - **Structural component I_s:**

$$\frac{\partial \widetilde{I_s}}{\partial t} = -sign(\Delta \widetilde{I_s}) \times \left\|\nabla \widetilde{I_s}\right\|_2$$

t : chock filter parameter.

$$C(h) = \frac{1}{2}\|h * \nabla_x S - \nabla_x g\|_2^2 + \frac{1}{2}\left\|h * \nabla_y S - \nabla_y g\right\|_2^2 + \alpha\|h\|_{0.5}^{0.5}$$

With h≥ 0 and $\sum_{i,j} h(i,j) = 1$

Where $\nabla_i S$ corresponds to the major edges (horizontal and vertical) of the structural part with $\nabla S = \nabla \widetilde{I_s}\,|_\vartheta$ for a threshold value $\boldsymbol{\vartheta}$

$\boldsymbol{\alpha}$: regularization parameter related to h with a fixed value of 0.01

$$C(f_{lat}) = \|h_E * f_{lat} - g\|_2^2 + \beta\|\nabla f_{lat}\|_1$$

β : regularization parameter associated with f_{lat} with a fixed value of 0.005

- PSF size (21x21)
- Scale number: 5 *
- $\alpha = 0.01$
- $\beta = 0.005$
- $\ni_{s,t} = 1$ for the first iteration and then $\ni_{s,t} = \frac{\ni_{s,t}}{1.1}$
- $t = 1$ at the first iteration then $t = \frac{t}{1.1}$
- Edge selection threshold (*its value is initially estimated form the degraded image and changes with every iteration*): $\vartheta = \frac{\vartheta}{1.1}$
- Choosing the solution at the 5th iteration for the estimation of h and f_{lat}

- **Final step: estimation of the original image f**

$$C(f) = \|h_E * f - g\|_2^2 + \kappa \times \left(e^{-\|\nabla_x S\|_{0.8}} \times \|\nabla_x f\|_1 + e^{-\|\nabla_y S\|_{0.8}} \times \left\|\nabla_y f\right\|_1\right)$$

κ: regularization parameter related to the original image restoration

</td>
<td>9 prior knowledge information (8 for the alternated step and 1 for the final step)</td>
</tr>
<tr>
<td colspan="2">* The number of scales depends on the support size of the PSF (for a PSF of size 21×21, we have 5 scales)</td>
</tr>
</table>

Table 11: Parameter values and number of iterations empirically fixed in the original method.

3. Developed Blind Method for monochrome images

In this section, we propose a method to solve the complex problem of blind monochrome image restoration where there is no prior information available about the original monochrome image, blur, or regularization parameter values.

Based on a study by Zhang et al. [48][49], the proposed blind method is considered a hybrid approach that follows the same principles as the semi-blind method proposed by Pan et al. [26] with an adaptive selection step for regularization parameter values. To develop a method with the same principle while improving the restoration quality, various solutions are proposed related to the estimation of the PSF and the latent image also for the final image restoration.

3.1. Proposed solution for the PSF and latent image estimation

To reduce the number of prior known information and avoid the manual tuning of the regularization parameters while optimizing the results, four steps are introduced for the PSF and the latent image estimation illustrated in Figure 10:

a) Defining the number of scales
b) Separating the structural and textural components
c) Estimating the regularization parameter α and the PSF
d) Estimating the regularization parameter β_{lat} and the latent image

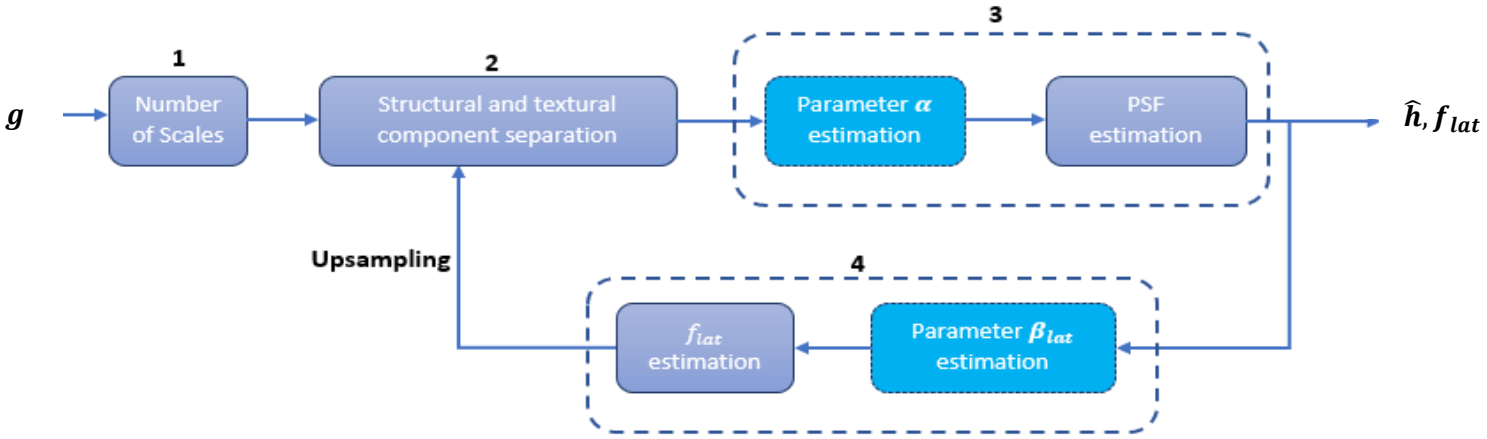

Figure 10: Flowchart of the PSF, latent image and regularization parameters estimation

3.1.1. Definition of the number of scales

The estimation of the PSF (Point Spread Function) and the latent image is performed following a multi-scale pyramidal model, starting from the coarsest scale and progressing to the finest scale (also known as full scale). At the coarsest scale the PSF support size, assumed to be square, is defined as $e_{1_h} = L_{1_h} \times L_{1_h}$ as for the latent image $e_{1_f} = L_{1_f} \times H_{1_f}$.

Having the PSF support size of $K \times K$ pixels and the image of size $M \times N$ pixels, the PSF size at the current i^{th} scale is defined as $L_{i_h} \times L_{i_h}$.

$$L_{(i+1)h} = L_{ih} + 2 \tag{39}$$

As for the latent image at the i^{th} scale, its size is equal to $e_{1_f} = L_{1_f} \times H_{1_f}$ where:

$$L_{(i+1)f} = integer\ part\left[M \times \frac{L_{(i+1)h}}{K}\right] \tag{40}$$

$$H_{(i+1)f} = integer\ part\left[N \times \frac{L_{(i+1)h}}{K}\right] \tag{41}$$

The sizes of the coarsest scales e_{1_h} and e_{1_f} are determined to be half of the sizes of the PSF and degraded image at full scale, respectively.

3.1.2. Separation of the structural and textural components of an image

To estimate the PSF and the latent image, the separation of the structural (edges) and textural components (textured and flat regions) of an image is a necessary step. Recalling the model for the structural and textural components separation:

$$\min_{I_s} \frac{1}{2\ \ni_{s,t} \times e^{-\|r\|^{0.8}}} \times \|I_s - f_{lat}\|_2^2 + \|\nabla I_s\|_2 \tag{42}$$

$\ni_{s,t}$ denotes the regularization parameter for the separation of the structural and textural components.

To mitigate the impact of the staircase effect in the structural component on the PSF estimation, the value of the regularization parameter needs to be large in smooth areas and small near the edges. Therefore, in (42) an adjustment parameter $e^{-\|r\|^{0.8}}$ is introduced, where $r(i)$ is defined as follows:

$$r(i) = \frac{\left\|\sum_{z \in W_q(i)} \nabla f_{lat}(z)\right\|_2}{\sum_{z \in W_q(i)} \|\nabla f_{lat}(z)\|_2 + 0.5} \tag{43}$$

$W_q(i)$ is a window of size $q \times q$ centered at pixel i. The divider consists of two parts: the first one indicates how strong the image structure is in a window $W_q(i)$. The second part is the added 0.5 value to prevent producing a large value in flat areas of the image.

Following the separation phase, a shock filter (44) is applied to refine the previously obtained edges.

$$\frac{\partial \widetilde{I_s}}{\partial t} = -sign\left(\Delta \widetilde{I_s}\right) \times \left\|\nabla \widetilde{I_s}\right\|_2 \tag{44}$$

$\widetilde{I_s} = \widetilde{I_s}(x, y, t)$ is the enhanced structural component, $sign(.)$ is the sign function, Δ is the Laplacian operator and t is a scalar regularization parameter related to the shock filter.

With $\nabla \widetilde{I_s}(x, y) = \left(\frac{\partial \widetilde{I_s}}{\partial x}\right)^2 \times \frac{\partial^2 \widetilde{I_s}}{\partial x^2} + 2 \times \left(\frac{\partial^2 \widetilde{I_s}}{\partial x \partial y}\right) \times \frac{\partial \widetilde{I_s}}{\partial x} \times \frac{\partial \widetilde{I_s}}{\partial y} + \left(\frac{\partial \widetilde{I_s}}{\partial y}\right)^2 \times \frac{\partial^2 \widetilde{I_s}}{\partial y^2}$

In the original method [26], the authors update three regularization parameters:

i) The regularization parameter related to the structural and textural components separation, $\ni_{s,t}$
ii) The regularization parameter related to the cock filter to enhance the structural component, I_s
iii) The edge selection threshold, ϑ

For these three regularization parameters, the reduction factor is fixed to 1.1. Additionally, the number of iterations for selecting the estimated PSF and the latent image is empirically fixed to 5 iterations.

In the thesis of Mo Zhang [49], a series of tests were conducted, showing the following drawbacks:

i) The evolution of the regularization parameters $\ni_{s,t}, t$, and ϑ, chosen by the authors, does not guarantee the convergence of the algorithm
ii) Fixing the number of iterations to 5 for selecting the estimation results yields to a suboptimal solution.

To resolve the problem mentioned in i), we propose to handle the decreasing evolution of the values of the two parameters $\ni_{s,t}$ and t differently at each scale, and the edge selecting threshold of the latent image. The values of $\ni_{s,t}$ and t are determined at the beginning of each scale and remain constant throughout all iterations. However, at the full scale, they vary during the first five iterations to extract relevant contours and then remain constant thereafter.

The initialization value for the regularization parameter $\ni_{s,t}$ and t is fixed at 1. To eliminate the fixed decreasing ratio for these parameters, the updating values is ensured by a scale factor fac_{ech} as follows:

$$\ni_{s,t_{i+1}} = \frac{\ni_{s,t_i}}{fac_{ech}} \quad , \quad t_{i+1} = \frac{t_i}{fac_{ech}} \quad , \quad fac_{ech} = \frac{L_{(i+1)h} \times L_{(i+1)h}}{L_{ih} \times L_{ih}}$$

At the full scale, the values of these two regularization parameters are updated for the first five iterations as follows:

$$\ni_{s,t_{nb+1}} = \frac{\ni_{s,t_{nb}}}{fac_{ech}} \quad , \quad t_{nb+1} = \frac{t_{nb}}{fac_{ech}}$$

Where nb corresponds to the number of iterations.

As for the edge selecting threshold ϑ, estimated at each iteration, and determined by: first the edges of $\widetilde{I_s}$ are classified into eight groups based on the eight orientations instead of four. Then, for each group, the magnitude of the edges is calculated, and only the top 1% of edges with the highest magnitude are retained. Finally, the estimated threshold value is determined as the lowest value among the retained edges.

Furthermore, to improve the original method, we propose a blind stopping criterion to ensure a better estimation of the PSF and the latent image. Defining a blind stopping criterion can only rely on the available data. In our case, the only available data is the observed image and its estimation. Since the L_1 norm provides a direct and untransformed estimation error (direct sum over each pixel), we prioritize it over the L_1 norm of the estimation error. Therefore, the optimal solution is the one that minimizes $\|g - h * f_{lat}\|_1$.

3.1.3. Estimation of the regularization parameter α and the PSF

In this subsection, we are looking to estimate the regularization parameter α related to the estimation of the PSF. The objective here is to determine the value of α at each iteration.

After introducing the separation of the structural and textural components to extract the most significant edges, from which the PSF estimation is derived, a pyramidal multiscale approach, as suggested in [26] is being implemented. The approach involves minimizing the cost function (45) related to the PSF at each scale.

$$C(h) = \frac{1}{2}\left[\|h \times \nabla_x S - \nabla_x g\|_2^2 + \left\|h \times \nabla_y S - \nabla_y g\right\|_2^2\right] + \hat{\boldsymbol{\alpha}} \|h\|_{0.5}^{0.5} \quad (45)$$

Where $\nabla_x S$ and $\nabla_y S$ represent the horizontal and vertical salient edges, respectively, after the post-processing of f_{lat} .

The "Generalized Cross Validation" (GCV) approach allows the estimation of the regularization parameter α without prior known information. It exists a variant known as "Weighted Generalized Cross Validation" (WGCV), proposed in [63] as an enhancement to the GCV approach. Both of these approaches were developed for Tikhonov-type regularization (L_2 norm), noting that the cost function used in the original approach [26] for the PSF estimation is of hyper-Laplacian-type ($L_{1/2}$ norm).

In the previous thesis of Zhang Mo [49], the choice of the hyper-Laplacian-type regularization was justified. An analysis to evaluate the effectiveness of applying GCV and WGCV for estimating the regularization parameter α was also conducted in [49]. This analysis justified the utilization of the WGCV approach, which is seen as minimizing the sum of prediction errors. The PSF cost function used for the WGCV is as follows :

$$C(h) = \frac{1}{2}\|h_E \times \nabla_x S - \nabla_x g\|_2^2 + \hat{\alpha}_x \|h_E\|_2^2 + \frac{1}{2}\left\|h_E \times \nabla_y S - \nabla_y g\right\|_2^2 + \hat{\alpha}_y \|h_E\|_2^2 \quad (46)$$

Considering $\{[\nabla_i g]_L - [h_E \times \nabla_i S]_L\}^2$ as the error prediction at the L^{th} component of the gradients in the horizontal and vertical directions. To calculate the values of $\alpha_x$and α_y, we need to estimate the PSF (h) by minimizing the following:

$$C(h) = \sum_{L=1}^{m^2} \frac{1}{2}\left\|F_j \times ([\nabla_i g]_l - [h_E \times \nabla_i S]_L)\right\|_2^2 + \hat{\boldsymbol{\alpha}}_{\boldsymbol{i}} \times \|h_E\|_2^2 \quad (47)$$

m^2 is the size of the enhanced and thresholded structural components $\nabla_i S$. The authors of [63] proposed, to partially preserve the observation $[\nabla_i g\,]_L$, a diagonal matrix $F_j = diag\left(1,1,\dots 1,\sqrt{(1-\omega)},1,\dots,1\right)$ with $\omega \in [0,1]$. Therefore, the corresponding model for the estimation of the regularization parameter α_i is the one that minimizes the WGCV criteria [63]:

$$WGCV(\alpha_i) = \frac{m^2 \left\| \left(I - \nabla_i S \times A_{\alpha_i}\right) \times \nabla_i g \right\|_2^2}{trace\left(I - \omega \times \nabla_i S \times A_{\alpha_i}\right)^2} \quad (48)$$

I is the identity matrix, and A_{α_i} is the linear operator for deriving the solution $\widehat{\boldsymbol{h}}$ in case of Tikhonov-type regularization: $A_{\alpha_i} \times \nabla_i g = h_E \leftrightarrow A_{\alpha_i} = [(\nabla_i S)^T \times \nabla_i S + \alpha_i I]^{-1} \times (\nabla_i S)^T$. To solve equation (48), the authors in [63] propose to apply a preliminary iterative algorithm called "Lanczos bidiagonalization" [64] to the matrix $\nabla_i S$, and perform a Singular Value Decomposition (SVD) on the obtained diagonal matrix.

When $\omega = 1$, the WGCV cost function is reduced to the GCV cost function.

For the k^{th} iteration the weight ω_k is predicted by averaging all the previously estimated weights as follows:

$$\widehat{\omega}_k = \frac{1}{k} \sum_{j=1}^{k} \widehat{\omega}_j$$

Where $\widehat{\omega}_j$ is calculated by solving: $\frac{\partial WGCV(\widehat{\alpha}_i)}{\partial \omega_k} = 0$

Since the estimation of α_x and α_y considers only the data fidelity term $\left(\|h_E \times \nabla_x S - \nabla_x g\|_2^2 \; or \; \left\|h_E \times \nabla_y S - \nabla_y g\right\|_2^2\right)$, the final estimation of the parameter α is determined by averaging $\hat{\alpha}_x$ and $\hat{\alpha}_y$. The estimated value of α is then used in the cost function (45) for PSF estimation (where η = 0.5). After establishing value $\hat{\alpha}$, the PSF is calculated using the cost function (45), and the solution is as follows:

$$\hat{h} = \left(\nabla_x S^T \nabla_x S + \nabla_y S^T \nabla_y S + \left(\frac{\hat{\alpha} \times I}{2 \max\left(\left|\hat{h}\right|^{1,5}, \tau\right)} \right) \right)^{-1} \times \left(\nabla_x S^T \nabla_x g + \nabla_y S^T \nabla_y g \right) \quad (49)$$

τ represents the solution constraint to avoid dividing by zero. The value of this threshold corresponds to the average value of $\left|\hat{h}\right|$.

- **Algorithm for the estimation of the regularization parameter α and the PSF**

The following algorithms are implemented to estimate the regularization parameter α associated with the cost function of the PSF(Algorithm 1), along with the estimation of the PSF (Algorithm 2).

Algorithm 1

Input: k =1, $\omega_1 = 1$, $i_{save} = 1$;
Output: $\hat{\alpha}$
For $i = x, y$
  While $k \leq 800$
    $\hat{\alpha}_{i,k} = \arg\min_{\alpha_i} WGCV(\alpha_i)$
    If $\left\| \frac{WGCV(\hat{\alpha}_{i,k}) - WGCV(\hat{\alpha}_{i,k-1})}{WGCV(\hat{\alpha}_{i,1})} \right\|_1 \leq e^{-5}$ & k > 1
      $i_{save} = i_{save} + 1$
      If $i_{save} \geq 5$
        Return $\hat{\alpha}_{i,k}$
      End if
    End if
  End while
End for
$\hat{\alpha} = \frac{\hat{\alpha}_x + \hat{\alpha}_y}{2}$

Algorithm 2

Input: $\hat{\alpha}, \nabla_x S, \nabla_y S, \nabla_x g$ and $\nabla_y g$
Output: $\hat{h}$
$\hat{h}_1 = \left(\nabla_x S^T \nabla_x S + \nabla_y S^T \nabla_y S\right)^{-1} \times \left(\nabla_x S^T \nabla_x g + \nabla_y S^T \nabla_y g\right)$
For $i_{ext} = 1{:}2$
  $\hat{h} = \left(\nabla_x S^T \nabla_x S + \nabla_y S^T \nabla_y S + \left(\frac{\alpha \times I}{2 \max\left(|\hat{h}_1|^{1,5}, \tau\right)}\right)\right)^{-1} \times \left(\nabla_x S^T \nabla_x g + \nabla_y S^T \nabla_y g\right)$
  $\hat{h}_1 = \hat{h}$
End for
$\hat{h}(\hat{h} < 0) = 0$
$\hat{h} = \frac{\hat{h}}{\sum \hat{h}(i,j)}$

3.1.4. Estimation of the regularization parameter β_{lat} and f_{lat}

In this subsection, we will now focus on estimating the regularization parameter β_{lat} associated with the regularization term of the latent image in the cost function (37).

$$C(f_{lat}) = \| g - h_E * f_{\text{lat}} \|_2^2 + \beta_{lat} \| \nabla f_{lat} \|_1$$

The value of $\beta_{lat} \in]0,1[$.

The estimation of β_{lat} involves estimating the parameter λ (given that $\beta_{lat} = \frac{1}{\lambda}$) according to the relationship established in [65]. Once the value of λ is determined, it is integrated into the cost function (37) for the estimation of f_{lat}.

We first define $(\lambda_k)_{(i,j)}$ as the approximation of the regularization parameter λ for each pixel (i,j) at each iteration k. The local variation of $\hat{f}_{lat}$ at (i,j) is defined by the average filter proposed in [65][66]:

$$S_{i,j}^{v} = \frac{1}{v \times v} \times \sum\nolimits_{s,t \in \Omega_{i,j}^{v}} [g(s,t) - h_E * f_{lat}(s,t)]^2 \tag{50}$$

where $v \times v$ is the window size and $\Omega_{i,j}^{v} = \left\{(s+i, t+j), -\frac{v-1}{2} \leq s,t \leq \frac{v+1}{2}\right\}$.

With the definition provided above, the estimation of the regularization parameter λ, as outlined in [66] and evaluated in Zhang Mo's thesis [49], is as follows:

$$\left(\hat{\lambda}_{k+1}\right)_{i,j} = \frac{1}{v \times v} \times \sum_{s,t \in S_{i,j}^{v}} \left(\tilde{\lambda}_{k+1}\right)_{s,t} \tag{51}$$

With $\left(\tilde{\lambda}_{k+1}\right)_{i,j} = 2 \times \left[\left(\hat{\lambda}_k\right)_{i,j} + \rho_k \times \max\left(\left(S_{i,j}^{v} - \sigma\right), 0\right)\right]$

Here, the multiplication by 2 accelerates the convergence speed, and since the process of updating the value of λ is iterative, the value of λ_0 is initialized as the degraded image. $\sigma = e^{-10}$, and ρ_k is set to $\|\lambda_k\|_\infty$ to maintain the same scale order.

At the full scale, f_{lat} is initialized with the blurred image. Then, the intermediate image is estimated, and $\hat{\lambda}$ is recalculated based on the latent image. The recalculated $\hat{\lambda}$ is used as input for the next scale.

The stopping criteria is when the variation of $\|g - h * f_{lat}\|_2^2$ between two consecutive iterations is less than a threshold ($Th = 10^{-3}$).

$$\left\|g - h_{k-1} * f_{lat_{k-1}}\right\|_2^2 - \left\|g - h_k * f_{lat_k}\right\|_2^2 \leq Th \tag{52}$$

After determining the update relationship of the parameter λ, we will incorporate it into the implementation process of the algorithm for estimating the latent image f_{lat}.

In the coarsest scale, the parameter λ is initialized using the degraded image

For the estimation of f_{lat}, we need to minimize the cost function (37). First, the initialization of f_{lat} is set to the degraded image. Following the same algorithm proposed in [26], the optimality condition is when $\nabla C(f_{lat}) = 0$. Meanwhile, the regularization term $\| \nabla f_{lat} \|_1$ is undifferentiable when ∇f_{lat} is null. Therefore, the approximation of $\nabla[\| \nabla f_{lat} \|_1]$ at the iteration k is as follows:

$$\nabla_{f_{lat}}[\| \nabla f_{lat,k} \|_1] \approx \left[\frac{\nabla_x I}{\max(|\nabla_x f_{lat,k-1}|, \tau_x)} + \frac{\nabla_y I}{\max(|\nabla_y f_{lat,k-1}|, \tau_y)}\right] \times f_{lat,k}$$

k represents the iteration number, I is the identity matrix, while τ_x and τ_y represent, respectively, the desired solution accuracy in the x and y directions to prevent the dividing by zero. Instead of setting a low value as proposed in [26], the values of τ_x and τ_y are determined by averaging the absolute value of $\nabla_x f_{lat,k-1}$ and $\nabla_y f_{lat,k-1}$, respectively. As a result, the equation $\nabla C(f_{lat}) = 0$ is equivalent to:

$$f_{lat,k} = \left[h_{E_k}^T \times h_{E_k} + \beta_{lat,k-1}\left(\frac{\nabla_x \times I}{\max(|\nabla_x f_{lat,k-1}|, \tau_x)} + \frac{\nabla_y \times I}{\max(|\nabla_y f_{lat,k-1}|, \tau_y)}\right)\right]^{-1} \times (h_{E_k}^T g) \quad (53)$$

- **Algorithm for the estimation of the regularization parameter β_{lat} and the latent image f_{lat}**

The overall algorithm for estimating the latent image f_{lat}, considering the adaptive estimation of the regularization parameter λ of the k^{th} iteration in the current scale is as follows:

Algorithm 3

Input: $g, \hat{\lambda}_{k-1}, f_{lat,k-1}$, and h_{E_k}

Output: $f_{lat,k}, \hat{\lambda}_k$

For $i_{ext} = 1:2$

$$f_{lat,k} = \left[h_{E_k}^T \times h_{E_k} + \beta_{lat,k-1}\left(\frac{\nabla_x \times I}{\max(|\nabla_x f_{lat,k-1}|, \tau_x)} + \frac{\nabla_y \times I}{\max(|\nabla_y f_{lat,k-1}|, \tau_y)}\right)\right]^{-1} \times (h_{E_k}^T g)$$

If $\left\|g - h_{E_{k-1}} * f_{lat_{k-1}}\right\|_2^2 - \left\|g - h_{E_k} * f_{lat_k}\right\|_2^2 \leq Th$

Return

Else update the regularization parameter λ using (51) to get $\hat{\lambda}_k$

$\hat{\lambda}_{k-1} = \hat{\lambda}_k$

End if

$f_{lat,k-1} = f_{lat,k}$

End for

- **The global algorithm for the estimation of the PSF**

Here, we present the global algorithm for the alternating step of estimating the Point Spread Function (PSF) and the corresponding latent image f_{lat}, along with the estimation of the regularization parameters α and β_{lat}. The algorithm follows the proposed solutions and incorporates the suggested modifications.

The specific description of the alternating step for estimating the PSF and the latent image is provided below:

Algorithm 4

Input:

- Degraded image $\boldsymbol{g}$
- PSF size $\boldsymbol{k_1}, \boldsymbol{k_2}$
- Initialization of the regularization parameter related to the cost function of the estimation of f_{lat}: $\lambda_0 = g$
- Initialization of the regularization parameters related to the separation between the structural and textural components $\mathfrak{s}_{\mathbf{s,t}} = \mathbf{1}$
- Initialization the parameter related to the chock filter $\boldsymbol{t} = \mathbf{1}$
- Calculating the maximum number of scales, $\boldsymbol{max_{scales}}$ (section 3.1.1)
- Calculating the PSF size for each scale

PSF estimation:

for $i_{scale} = 1 : max_{scales}$

$\lambda_0 = g$ *(subsampled)*

If $i_{scale} == 1$

$f_{lat} = g$ *(subsampled)*

Else

$$f_{lat} = \left[h_E^T \times h_E^T + \lambda_0^{-1}\left(\frac{\nabla_x \times I}{\max(|\nabla_x f_{lat}|, \tau_x)} + \frac{\nabla_y \times I}{\max(|\nabla_y f_{lat}|, \tau_y)}\right)\right]^{-1} \times (h_E^T g)$$

End if

$\hat{\lambda} = \lambda_0$

For $k = 1 : \boldsymbol{maxitr}$

- Estimation of the structural component $\hat{I}_s$ from $\hat{f}_{lat}$ using (42)
- Compute $\widetilde{I_s}$ by applying shock filter for $\hat{I}_s$ using (44)
- Edge extraction from $\widetilde{I_s}$ then apply the estimated threshold ϑ to select significant edges
- Estimation of the regularization parameter α by applying the WGCV approach (Algorithm 1). Then estimation of the PSF (Algorithm 2)
- Estimation of the regularization parameter λ, then estimate f_{lat} (Algorithm 3)

End for

Retain $\hat{h}$ corresponding to the minimum of the criterion $\|g - \hat{g}\|_1$ for all the $\boldsymbol{maxitr}$ iterations.

Update the regularization parameters $\mathfrak{s}_{\mathbf{s,t}}$ and $\boldsymbol{t}$ as described in section 3.1.1.

End for

Output:

$\hat{h}, f_{lat}$ corresponding to the minimum of the criterion $\|g - \hat{g}\|_1$ over 100 iterations.

3.2. Original image estimation

For this subsection we are interested in the original image restoration. For this restoration we use the estimated PSF from the previous alternated step explained in subsection 3.1.

To restore the original image, two steps are introduced shown in Figure 11:

a) Spatial shift reduction
b) Estimation of the regularization parameter β and the original image restoration

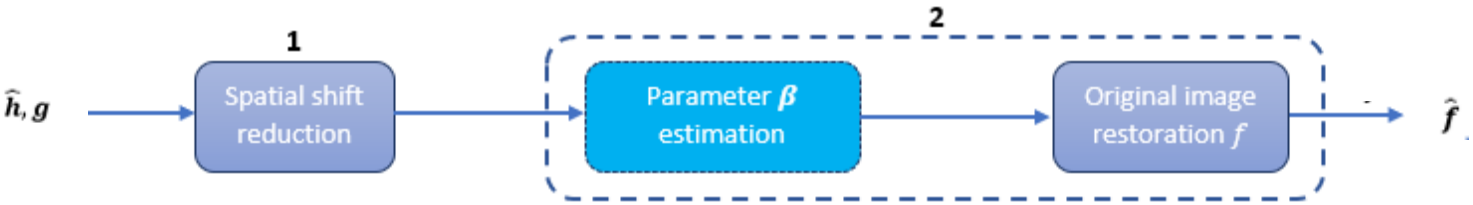

Figure 11: flowchart for the original image restoration

3.2.1. Spatial shift reduction

In most cases, during the alternating step, the estimated point spread functions undergo a slight spatial shift compared to their original PSF. This shift negatively impacts the quality of the estimated latent image. To mitigate this effect on the desired original image, we propose a straightforward approach: reducing the size of the estimated PSF by considering only the non-zero values. For the estimation of the original image, we utilize the PSF estimated based on the reduced support size.

This approach retains only the essential values of the estimated PSF while adjusting its support size. Initially, an adaptive threshold is applied based on the standard deviation of the estimated PSF. Then the support size is reduced by eliminating pixels values lower than the threshold. If, after this adjustment, the number of rows or columns is even, an additional row or column is added to ensure an odd-sized PSF support. Finally, a re-normalization step is performed to guarantee that the sum of all values is equal to 1.

3.2.2. Estimation of the regularization parameter β and the final image

After reducing the spatial shifting induced in the PSF estimation phase, we are interested in restoring the final image using the refined estimated PSF. First, we represent the cost function related to the final image restoration used in this second step.

$$C(f) = \|h_E * f - g\|_2^2 + \hat{\beta}\, \|\nabla^2 f\|_1 \tag{54}$$

$\hat{\boldsymbol{\beta}}$ is the estimated regularization parameter related to the original image estimation equal to λ^{-1}, $\|\nabla^2 f\|_1$ is the total anisotropic variation of second order.

To find the optimal solution for the cost function (54), we use the same approach proposed in [30]:

The optimality condition is $\nabla C(f) = 0$. While the term $\|\nabla^2 f\|_1$is not differentiable when $\nabla^2 f$ is null, an approximation of $\nabla[\|\nabla^2 f\|_1]$ is expressed as follows:

$$\nabla_f \left[\left\|\nabla^2 \hat{f}_k\right\|_1\right] \approx \sum_u \frac{\nabla_u \hat{f}_k}{\max\left(\left|\nabla_u \hat{f}_{k-1}\right|, \tau_u\right)}$$

$\hat{f}_{k-1}$ is the estimated image in the previous iteration, initially estimated by the solution of $\nabla\left\|h_E * \hat{f} - g\right\|_2^2 = 0$, $u \in \{x, y, xy, xx, yy\}$, τ_u are values introduced to prevent the division by zero. Here, instead of setting the values to 10^{-2} as proposed in [30], τ_u is equal to the average of $\left|\nabla_u \hat{f}_{k-1}\right|$. Finally, the optimal solution is obtained as follows:

$$\hat{f}_k = \left[h_E^T \times h_E + \hat{\lambda}^{-1} \times \sum \left(\nabla_u \times \frac{I}{\max\left(\left|\nabla_u \hat{f}_{k-1}\right|, \tau_u\right)}\right)\right]^{-1} \times (h_E^T g) \quad (55)$$

The equation (55) is resolved using the conjugate gradient algorithm with a fixed number of iterations set to 100. The estimation of the regularization parameter λ is performed in the same way as before (51).

- **The Algorithm for the final image restoration**

Algorithm 5

Input: g, $\hat{\lambda}_{k-1}$, $\hat{f}_{k-1}$, and h_E

Output : $\hat{f}$, and $\hat{\lambda}_k$

For $i_{ext} = 1{:}2$

$$\hat{f}_k = \left\{h_E^T \times h_E + \hat{\lambda}_{k-1}{}^{-1} \times \left[\frac{\nabla_x \times I}{\max\left(\left|\nabla_x \hat{f}_{k-1}\right|, \tau_x\right)} + \frac{\nabla_y \times I}{\max\left(\left|\nabla_y \hat{f}_{k-1}\right|, \tau_y\right)} + \frac{\nabla_{xy} \times I}{\max\left(\left|\nabla_{xy} \hat{f}_{k-1}\right|, \tau_{xy}\right)} + \frac{\nabla_{xx} \times I}{\max\left(\left|\nabla_{xx} \hat{f}_{k-1}\right|, \tau_{xx}\right)} + \frac{\nabla_{yy} \times I}{\max\left(\left|\nabla_{yy} \hat{f}_{k-1}\right|, \tau_{yy}\right)}\right]\right\}^{-1} \times (h_E^T g)$$

If $\left\|h_E * \hat{f}_{k-1} - g\right\|_2^2 - \left\|h_E * \hat{f}_k - g\right\|_2^2 \leq 10^{-3}$

Return

Else update the value of λ using (51)

$\hat{\lambda}_{k-1} = \hat{\lambda}_k$

End If

$\hat{f}_{k-1} = \hat{f}_k$

End For

4. Blind developed method for hyperspectral images

A hyperspectral image is composed of B spectral components of spatial dimension M×N. Therefore, after establishing a blind image restoration for monochrome images, in this section we represent two strategies

for restoring a full hyperspectral image. These strategies are intended to be compared in terms of their effectiveness and performance.

First strategy:

In the first strategy, we propose a spectral component selection method called Unsupervised Partitioning based on Affinity Propagation (UP-OAP) [76]. This method employs an unsupervised partitioning technique to group highly correlated spectral components and selects an exemplar component to represent each group. The main objective of this method is to reduce the number of spectral components used in the PSF estimation phase.

Instead of estimating the Point Spread Function (PSF) using all spectral components, this approach utilizes selected exemplar spectral components from each correlated group. The estimation of a latent image is then performed for each selected exemplar component (as a monochrome image) using the previously explained proposed blind restoration method for monochrome images. The estimated PSF from each exemplar spectral component is employed to restore all spectral components belonging to its respective group.

By employing the UP-OAP method [76], we aim to enhance the efficiency and accuracy of the restoration process by reducing the computational complexity associated with estimating the PSF using all spectral components.

Second strategy:

In the second strategy, we retain the first two steps from the first strategy. That is, we employ the UP-OAP method to select exemplar components and estimate the PSF and latent image for each selected exemplar component.

However, in the second strategy, after obtaining the estimated PSFs from each exemplar spectral component, we evaluate the accuracy of each estimated PSF by using the L_1 norm of the error estimation between the estimated PSF and the ground truth $\left(\left\|h-\hat{h}\right\|_1\right)$. Additionally, we examine the L_1 norm of the error estimation between the observed degraded image and the estimated degraded image $(\|g-\hat{g}\|_1)$. The purpose of this evaluation is to identify the most accurate estimated PSF from the selected exemplar spectral component.

From this examination, we can determine which estimated PSF exhibits the highest accuracy. Once the most accurate estimated PSF is identified, we utilize it to restore the entire hyperspectral image. This means that instead of using multiple estimated PSFs for the hyperspectral image restoration, we rely on the single most accurate estimated PSF.

By using only one estimated PSF, we simplify the restoration process and potentially improve the overall image quality of the restored hyperspectral image.

5. Evaluation of the proposed method

In this section, we present a comprehensive evaluation of the developed method by integrating all the proposed solutions discussed in the previous sections. The primary objective of this evaluation is to demonstrate the effectiveness and superiority of our method compared to state-of-the-art techniques.

To ensure a full analysis, we utilize diverse test image databases that encompass monochrome, multicomponent (RGB), and hyperspectral images. This wide range of image types allows us to assess the performance of our method across various scenarios. In addition to comparing our method with the original approach, we also evaluate it against recent state-of-the-art methods. The comparisons are based on several evaluation metrics, as detailed in subsection 4.1.

The main goal of conducting this evaluation is to validate the effectiveness and robustness of our proposed method. We aim to showcase its superiority over existing techniques by providing compelling evidence through the evaluation results. These insights into the performance of our approach will not only contribute to the field of blind image restoration but also highlight its potential for practical applications.

5.1. Databases and evaluation criteria

In order to obtain reliable results, various databases were used, and specific evaluation criteria were employed. This subsection provides an overview of the databases used and the criteria utilized for the analysis and assessment of the restored images.

5.1.1. Databases

In order to demonstrate the robustness and applicability of our blind restoration approach, we have utilized multiple databases of different data types for the evaluation. The databases employed in this study exhibit variations in characteristics such as size, structure, and content. By incorporating this diverse range of databases, we aim to provide comprehensive evidence of the effectiveness of our proposed method in handling various scenarios and data variations.

a) *DBS1:* The database used in this study was constructed by A. Levin et al [62]. It includes four distinct images (Bridge, Photo, Face, and Wall) that will be further explored. In addition to these images, eight motion blurs were captured using an 85 mm lens and a 0.3-second exposure. The size of the point spread function (PSF) support ranges from 13×13 to 27×27, which will be subsequently exploited in the analysis.

b) *DBS2:* The database, LIV Public Domain Subjective Image Quality [67], containing twenty-nine high-resolution images, was created in the Laboratory for Images and Video Engineering at the University of Texas-Austin. These images are in 24 bits/pixel RGB color format and typically have dimensions of 768×512 pixels.

c) *DBS3:* The Kodak Lossless True Color Image Suite [68], released by the Eastman Kodak company, is composed of twenty-four high-quality true color images. Each image in the suite has a pixel depth of 24 bits per pixel (24bpp) and a resolution of 768×512 pixels.

d) *DBS4:* The CAVE dataset [69] was obtained using a generalized assorted pixel camera [70]. It comprises 32 indoor hyperspectral images (HSIs) capturing real-world materials and objects. Each

image in the dataset has a spatial resolution of 512×512 pixels and contains 31 spectral components, ranging from 400 to 700 nm with a 10-nm interval

e) *DBS5:* The Harvard dataset [71] comprises 50 hyperspectral images (HSIs) that feature natural scenes. These images were captured using a commercial hyperspectral camera [72]. Similar to the CAVE dataset, each image in the Harvard dataset consists of 31 consecutive spectral components, covering the wavelength range from 420 to 720 nm with a 10-nm interval. The spatial resolution of each image in the Harvard dataset is 1392×1040 pixels. However, for evaluation purposes, the images are cropped to a resolution of 512×512 pixels.

5.1.2. Evaluation criteria

In this subsection, we focus on the evaluation criteria employed to objectively assess the performance of our blind image restoration approach. we have selected a range of widely used evaluation criteria that provide quantitative measures for analyzing and comparing the effectiveness our algorithm.

The evaluation criteria considered in this subsection include the L_1 norm, Peak Signal-to-Noise Ratio (PSNR), Mean Peak Signal-to-Noise Ratio (MPSNR), Structural Similarity Index (SSIM), Mean Structural Similarity Index (MSSIM), Root Mean Square Error (RMSE), Kernel similarity (KS), and spectral signature. These objective criteria are commonly utilized in the literature and offer valuable insights into the quality and fidelity of the restored images.

The L_1 norm measures the absolute pixel-wise differences between the restored and original images. PSNR and MPSNR evaluate the quality of the restoration by quantifying the signal-to-noise ratio. SSIM and MSSIM assess the structural similarity between the restored and original images, considering both luminance and structural information. RMSE calculates the root mean square error, providing a measure of overall pixel-wise differences.

In addition to these image-based criteria, kernel similarity evaluates the similarity between the estimated and true blur kernels. Spectral signature criteria analyze the accuracy of the spectral information in the restored images.

5.2. Evaluation using monochrome images

To validate our proposed method, we first compared its performance to the original method [26], which utilizes empirically tuned regularization parameters, as exploit in Chapter two. The choice of this method was based on the method's superior performance in a comparative study [48][49]. For this evaluation, we have used four monochrome images ("Bridge," "Photo," "Face," and "Wall") from DBS1 [62]. Each image underwent artificial degradation using eight different PSFs of different support sizes, resulting in a total of 32 monochrome degraded images. The specific PSF functions and support sizes used in this series of tests are presented in Table 12. Looking at the PSF number 6 and 7, they have the same support size but different functions. Additionally, Figure 12 represents the four original monochrome images.

n°	1	2	3	4	5	6	7	8
size	13x13	15x15	17x17	19x19	21x21	23x23	23x23	27x27
Original	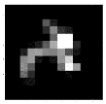	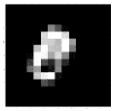	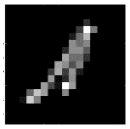	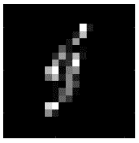	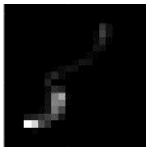	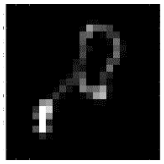	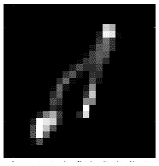	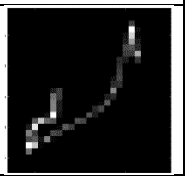

Table 12: The original PSFs from DBS1 [62]

"Bridge"

"Wall"

"Face"

"Photo"

Figure 12: The four original monochrome images used from DBS1 [62]

An assessment of the estimated Point Spread Function (PSF) was conducted to visually compare the performance of the original method and our proposed method. We are showing only the results of the "Bridge" image in Table 13. It is evident from the comparison that our proposed method effectively addresses the issue of spatial shifting present in the estimated PSF, which is not properly handled by the original method. This means that our method provides better regulation and alignment of the PSF, resulting in improved accuracy.

Upon visual inspection, it becomes particularly noticeable that the estimated PSFs obtained using our proposed method exhibit higher levels of accuracy. This is especially seen when examining PSF numbers 5, 6, 7, and 8.

Additionally, a visual evaluation was conducted to assess the restored image and the restored edges. Figure 13 illustrates the original edges that are present in both the "Bridge" and "Photo" images.

Table 14 visualizes the image restoration stages of two monochrome images, namely "Bridge" and "Photo", using three degradation functions (13×13, 19×19, 27×27) employed in the evaluation. Showing the progression from the blurred image to the latent image obtained during the PSF estimation step, and finally to the restored image after refining the estimated PSF. Additionally, the edge recovery process for each phase is shown in Table 14.

When examining the latent image of the "Photo" for the 13×13 PSF support size, a contrast difference is noticeable when compared to the final restored image. Similarly, for the "Bridge" latent image with the 27×27 PSF support size, there is a visible difference in contrast and a slight presence of blur.

In terms of edge recovery, it is evident that the final image restoration successfully recovers most of the salient edges in both images, as compared to the original edges shown in Figure 13. Moreover, the final restored images present more defined and continuous edges. In contrast, the edges in the estimated latent image appear discontinuous and less prominent.

Number	1	2	3	4	5	6	7	8
PSF Size	13x13	15x15	17x17	19x19	21x21	23x23	23x23	27x27
Original PSF(h)	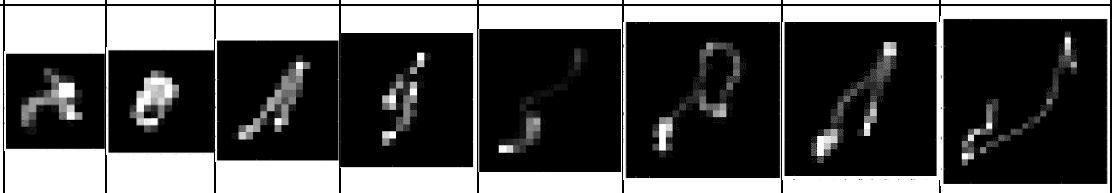							
Estimated PSF$(\hat{h})$ - original method	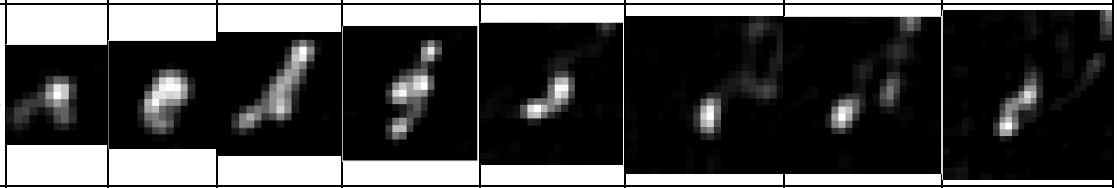							
Estimated PSF$(\hat{h})$- proposed method	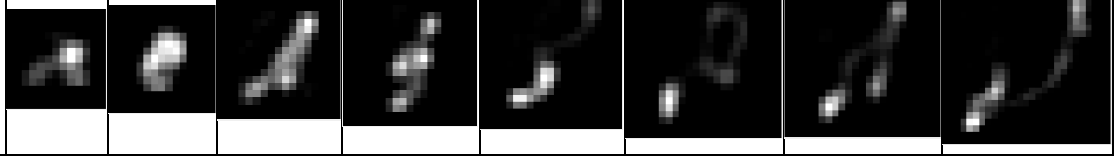							

Table 13: Visual comparison between the original PSFs, estimated PSFs using the original method, and the estimated PSF using the proposed method from the "Bridge" degraded image.

Figure 13: The original edges of the "Bridge" (left) and "Photo" (right) images

		Degraded	Latent	Restored
PSF size 13 × 13				
" Bridge"	image			
	Edges			

“ Photo”	Image			
	Edges			
PSF size 19 × 19				
“ Bridge”	Image			
	Edges			

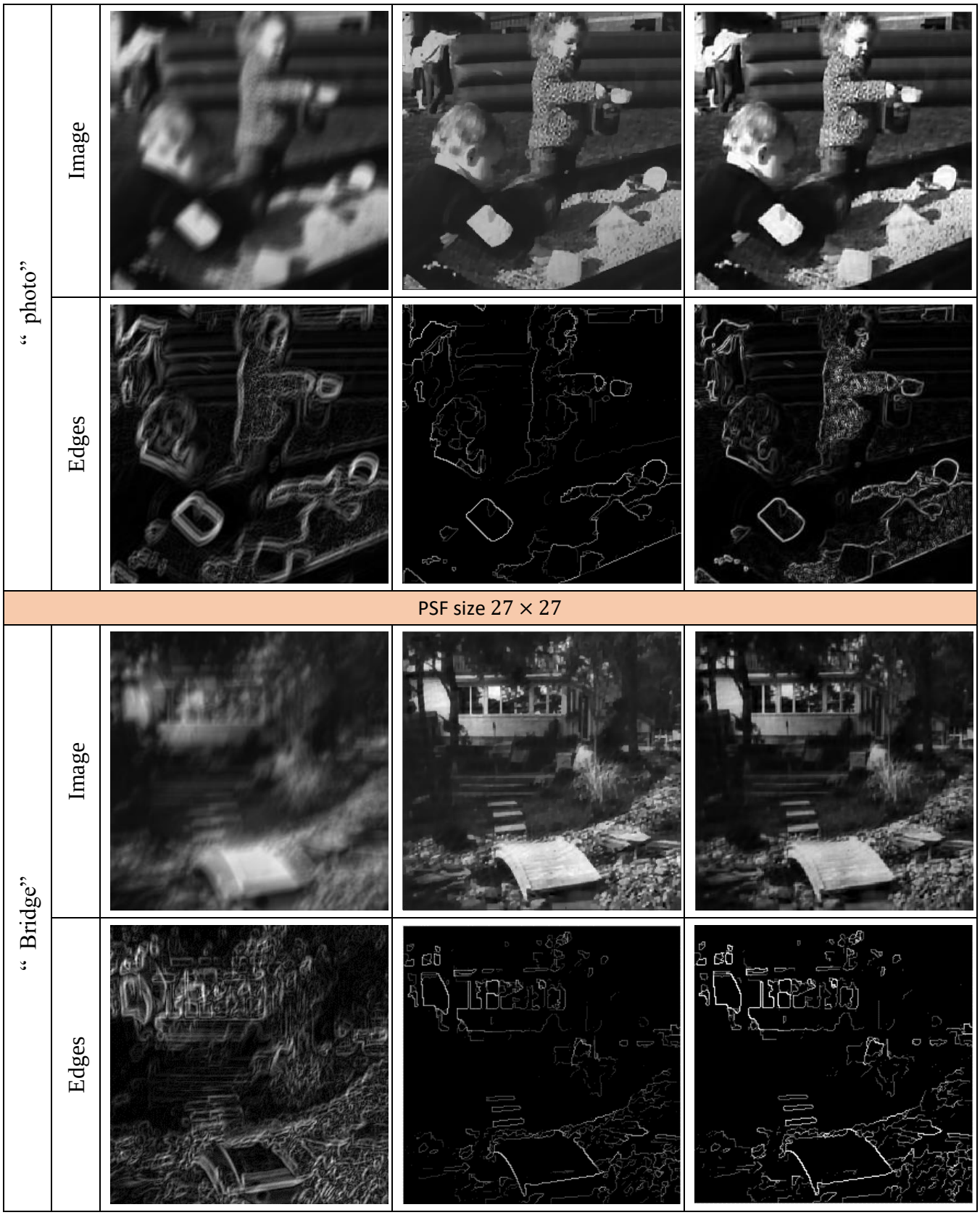
" photo"
Image
Edges
PSF size 27 × 27
" Bridge"
Image
Edges

" Photo"				
	Image	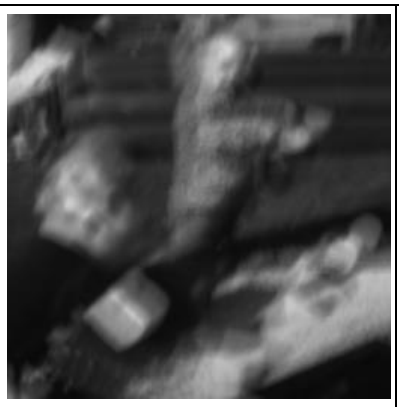		
	Edges	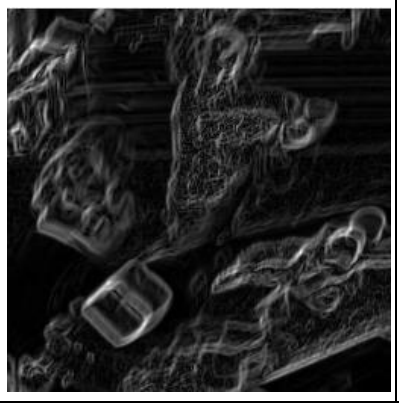		

Table 14: Comparison of degraded image, latent image, and final image restored with respective edges for "Bridge" and "Photo" images using PSF support size 13×13, 19×19, *and* 27×27

Furthermore, an objective assessment was carried out to evaluate the performance of the PSF estimation and restored image using our proposed method compared to the original method [26]. This assessment relied on three evaluation metrics: Peak Signal-to-Noise Ratio (PSNR), Structural Similarity Index (SSIM), and the absolute value of the L_1 norm of the estimated PSF and the restored image.

The results in Table 15 shows the comparison conducted between the original method and our proposed method using the absolute value of the L_1 norm to assess the estimation error of the PSF and the final restored image.

These results demonstrate that the proposed method outperforms the original method in terms of PSF estimation accuracy. The estimated PSFs obtained using our proposed method closely resemble the original degradation source, indicating higher precision. In addition to that, the absolute estimation error related to the final restored image is better than the original method.

Table 16 represent the evaluation conducted on the restored image using PSNR and SSIM evaluation criteria. Evaluating the final restored image using PSNR and SSIM and evaluation metrics shown the superiority and accuracy of our proposed method over the original method.

	PSF size	13x13	15x15	17x17	19x19	21x21	23x23	23x23	27x27
	Bridge								
$\|h - \hat{h}\|_1$	Original	1.0436	1.0706	0.8514	1.0501	1.6043	1.7024	1.6120	1.8183
	Proposed	**0.5166**	**0.5426**	**0.5547**	**0.7561**	**0.5500**	**0.5403**	**0.5040**	**0.7457**
	Original	3862.5	4256.3	3466.5	3238.1	7453.1	7039.7	7055.2	7323.7

$\|f-\hat{f}\|_1$	Proposed	**998.8030**	**1536.9**	**930.3412**	**984.9006**	**1022.9**	**1319.2**	**1193.7**	**1587.5**
Photo									
$\|h-\hat{h}\|_1$	Original	0.7003	0.6858	0.8475	1.0068	1.4357	1.6348	1.2606	1.7584
	Proposed	**0.6321**	**0.5730**	**0.7600**	**0.9128**	**0.7789**	**0.7700**	**0.6998**	**0.9824**
$\|f-\hat{f}\|_1$	Original	1131.4	1361.2	1798.8	1404.5	5533.6	5923.1	4135.6	5831.4
	Proposed	**938.0729**	**1214.2**	**1302.9**	**1320**	**1464.4**	**1513.4**	**1165.5**	**1329.5**
Face									
$\|h-\hat{h}\|_1$	Original	1.0031	**0.6943**	1.0797	1.1826	1.6606	1.7282	1.6215	1.7715
	Proposed	**0.7744**	0.7494	**0.8241**	**1.0201**	**0.9081**	**0.9513**	**1.0823**	**1.1973**
$\|f-\hat{f}\|_1$	Original	2093.8	**969.10**	2574.8	1895.6	6113.5	5154.6	5004.2	5785.4
	Proposed	**637.73**	1149.9	**1318.4**	**1331.9**	**1189.3**	**1549**	**3015.6**	**3126.9**
Wall									
$\|h-\hat{h}\|_1$	Original	1.0067	0.5903	1.2191	0.9607	1.5822	1.6969	1.4457	1.6956
	Proposed	**0.7181**	**0.5895**	**0.66729**	**0.9084**	**0.7127**	**0.6890**	**0.6814**	**0.8863**
$\|f-\hat{f}\|_1$	Original	2227.5	1040.8	2595.5	1272.4	6580.3	5610.4	5278.7	6254.3
	Proposed	**1259.5**	**1076.5**	**955.8388**	**1085.5**	**1200.9**	**1073.8**	**1229.9**	**1654**

Table 15: $\|h-\hat{h}\|_1$ and $\|f-\hat{f}\|_1$ of the proposed method and the original *methods*

	PSF size	13x13	15x15	17x17	19x19	21x21	23x23	23x23	27x27
	Bridge								
PSNR	Original	19.2438	19.8016	21.8706	21.0529	14.8784	15.3588	13.8763	15.4549
	Proposed	**29.3216**	**23.0437**	**25.1264**	**22.8250**	**20.1690**	**23.2581**	**25.3792**	**21.3737**
SSIM	Original	0.7175	0.6573	0.7874	0.8257	0.2676	0.3222	0.3210	0.2700
	Proposed	**0.9641**	**0.7457**	**0.8423**	**0.8876**	**0.5771**	**0.7397**	**0.8235**	**0.6146**
Photo									
PSNR	Original	**29.2214**	27.7363	**26.2064**	27.5756	16.5486	16.0657	17.8423	16.5517
	Proposed	23.4926	**28.3343**	25.1247	**27.6978**	**22.2322**	**21.1035**	**26.9023**	**24.5353**
SSIM	Original	**0.9356**	0.9057	**0.8576**	0.8310	0.4417	0.4420	0.5576	0.4167
	Proposed	0.8260	**0.9203**	0.8428	**0.9145**	**0.7402**	**0.6789**	**0.8794**	**0.8022**
Face									
PSNR	Original	24.8458	**32.6592**	23.7707	26.1673	16.8617	18.2953	18.7898	17.6096
	Proposed	**24.9343**	24.4035	**26.9823**	**29.3207**	**23.6247**	**26.6309**	**21.4071**	**22.0792**
SSIM	Original	0.8328	**0.9429**	0.7357	0.8385	0.3656	0.4285	0.4426	0.3980
	Proposed	**0.8919**	0.9094	**0.9004**	**0.9048**	**0.7849**	**0.8902**	**0.6117**	**0.6648**
Wall									
PSNR	Original	23.9710	**31.7460**	22.8936	29.8902	15.8735	16.9208	17.5547	16.4025
	Proposed	**25.1000**	24.7539	**24.7643**	**30.6666**	**21.2992**	**24.5423**	**23.2951**	**23.4602**
SSIM	Original	0.8136	**0.9483**	0.7717	0.9236	0.3308	0.3884	0.4219	0.3491
	Proposed	**0.9210**	0.8468	**0.8379**	**0.9398**	**0.6901**	**0.8338**	**0.7793**	**0.7627**

Table 16: Comparison of the final restored image between the original method and the proposed method using PSNR and SSIM evaluation criteria

To conclude the evaluation of the monochrome images, we also assessed the estimated regularization parameter obtained through our proposed method. According to the original method, the regularization parameters are fixed as $(\alpha, \beta_{lat}) = (0.01, 0.005)$ for the PSF and the latent image estimation, and $\beta = 0.003$ for the final image restoration, regardless of the image type used. In contrast, our proposed method estimates these parameters dynamically based on the specific characteristics of the image being processed.

Table 17 represents the estimated values for the regularization parameters related to the PSF and the latent image estimation at the iteration that yielded the optimal solution. These results are obtained for the four images and the eight PSFs of DBS1 [62]. We can see from this table that the minimum is reached at different iteration number even for two PSFs with the same support size (23x23).

As evident from Table 17, the combination of regularization parameters is specific to each individual image and degradation function. The proposed algorithm successfully estimated different parameter values based on the unique characteristics of the degraded image. This adaptability allows our algorithm to adapt the regularization process to effectively estimate the respective PSF and latent image, resulting in improved performance compared to the fixed parameter values used in the original method.

Table 18 displays the estimated parameters for the final image restoration, along with the corresponding iteration numbers at which the solutions are retained. The results presented in Table 18 highlight the distinctive nature of the regularization parameter values for each degraded image, emphasizing the significance of accurately estimating these parameters to achieve improved restoration outcomes.

		Estimated parameters						
	PSF size	Solution iteration number	λ variation range	β_{lat} variation range	$\hat{\alpha}$	$\ni_{s,t}$	t	ϑ
" Bridge"	13 × 13	84	[1, 908]	[0.001, 1]	0.0587	0.2336	0.2336	0.3178
	15 × 15	29	[1,881]	[0.0012, 1]	0.0080	0.2934	0.2934	0.3719
	17 × 17	20	[5, 677]	[0.0015, 0.2]	0.0636	0.2831	0.2831	0.3671
	19 × 19	39	[5, 683]	[0.0015, 0.2]	0.0408	0.3320	0.3320	0.2694
	21 × 21	70	[3, 588]	[0.0017, 0.3333]	0.1253	0.3176	0.3176	0.3315
	23 × 23	33	[3, 563]	[0.0018, 0.3333]	0.1194	0.3587	0.3587	0.2759
	23 × 23	93	[3, 538]	[0.0019, 0.3333]	0.0750	0.3587	0.3587	0.2541
	27 × 27	45	[4, 508]	[0.002, 0.25]	0.1376	0.3781	0.3781	0.2524
" Photo"	13 × 13	43	[2, 674]	[0.0015, 0.5]	0.0403	0.2336	0.2336	0.2021
	15 × 15	82	[2, 704]	[0.0014, 0.5]	0.0377	0.2934	0.2934	0.2943
	17 × 17	65	[2, 522]	[0.0019, 0.5]	0.0066	0.2831	0.2831	0.2570
	19 × 19	16	[3, 551]	[0.0018, 0.3333]	0.0068	0.3320	0.3320	0.1879
	21 × 21	51	[4, 480]	[0.0021, 0.25]	0.0052	0.3176	0.3176	0.1062
	23 × 23	15	[2, 485]	[0.0021, 0.5]	0.0042	0.3587	0.3587	0.2132
	23 × 23	63	[2, 512]	[0.002, 0.5]	0.0067	0.3587	0.3587	0.2440
	27 × 27	85	[2, 470]	[0.0021, 0.5]	0.0101	0.3781	0.3781	0.2163
" Face"	13 × 13	61	[6, 286]	[0.0035, 0.1667]	0.1194	0.2336	0.2336	0.3511
	15 × 15	17	[4, 272]	[0.0037, 0.25]	0.0057	0.2934	0.2934	0.3250
	17 × 17	79	[7, 297]	[0.0034, 0.1429]	0.0627	0.2831	0.2831	0.3261
	19 × 19	78	[5, 285]	[0.0035, 0.2]	0.0656	0.3320	0.3320	0.2834
	21 × 21	73	[4, 289]	[0.0035, 0.25]	0.0584	0.3176	0.3176	0.2879
	23 × 23	94	[3, 276]	[0.0036, 0.3333]	0.0608	0.3587	0.3587	0.2522
	23 × 23	9	[3, 273	[0.0037, 0.3333]	0.0053	0.3587	0.3587	0.1746
	27 × 27	5	[1, 288]	[0.0035, 1]	0.0106	0.3781	0.3781	0.1911
"	13 × 13	43	[5, 457]	[0.0022, 0.2]	0.1198	0.2336	0.2336	0.4828

	15 × 15	28	[2, 456]	[0.0022, 0.5]	0.0082	0.2934	0.2934	0.4530
	17 × 17	79	[2, 393]	[0.0025, 0.5]	0.0595	0.2831	0.2831	0.4468
	19 × 19	8	[1, 391]	[0.0026, 1]	0.0057	0.3320	0.3320	0.4216
	21 × 21	62	[1,339]	[0.0029, 1]	0.0620	0.3176	0.3176	0.4174
	23 × 23	98	[1, 304]	[0.0033, 1]	0.0597	0.3587	0.3587	0.3948
	23 × 23	12	[2, 290]	[0.0034, 0.5]	0.0035	0.3587	0.3587	0.3970
	27 × 27	74	[1,293]	[0.0034, 1]	0.0591	0.3781	0.3781	0.3430

Table 17: The estimated regularization parameter values related to the PSF estimated and the latent image along with the iteration number of the solution retained for the full database DBS1.

		Estimated parameters		
	PSF size	Solution iteration number	λ variation range	β variation range
" Bridge"	13 × 13	7	[7, 668]	[0.0015, 0.1429]
	15 × 15	7	[3, 677]	[0.0015, 0.3333]
	17 × 17	9	[7, 634]	[0.0016, 0.1429]
	19 × 19	8	[4, 676]	[0.0015, 0.25]
	21 × 21	7	[8, 671]	[0.0015, 0.1250]
	23 × 23	8	[8, 654]	[0.0015, 0.1250]
	23 × 23	8	[7, 630]	[0.0016, 0.1429]
	27 × 27	9	[4, 661]	[0.0015, 0.25]
" Photo"	13 × 13	5	[1, 550]	[0.0018, 1]
	15 × 15	6	[1, 475]	[0.0021, 1]
	17 × 17	6	[3, 504]	[0.002, 0.3333]
	19 × 19	7	[10, 507]	[0.002, 0.1]
	21 × 21	4	[1, 494]	[0.002, 1]
	23 × 23	8	[1, 465]	[0.0022, 1]
	23 × 23	6	[1, 564]	[0.0018, 1]
	27 × 27	7	[4, 609]	[0.0016, 0.25]
" Face"	13 × 13	6	[4, 322]	[0.003, 0.25]
	15 × 15	7	[5, 335]	[0.003, 0.2]
	17 × 17	6	[3, 342]	[0.0029, 0.3333]
	19 × 19	6	[4, 309]	[0.0032, 0.25]
	21 × 21	7	[4, 391]	[0.0026, 0.25]
	23 × 23	5	[2, 364]	[0.0027, 0.5]
	23 × 23	5	[1, 390]	[0.0026, 1]
	27 × 27	2	[1, 414]	[0.0024, 1]
" Wall"	13 × 13	5	[1, 434]	[0.0023, 1]
	15 × 15	6	[1, 408]	[0.0025, 1]
	17 × 17	8	[1, 315]	[0.0032, 1]
	19 × 19	6	[1, 326]	[0.0031, 1]
	21 × 21	5	[1, 307]	[0.0033, 1]
	23 × 23	7	[2, 349]	[0.0029, 0.5]
	23 × 23	7	[2, 332]	[0.003, 0.5]
	27 × 27	7	[2, 407]	[0.0025, 0.5]

Table 18: The estimated regularization parameter values related to the final image restoration along with the iteration number of the solution retained for the full database DBS1

Moreover, Table 19 presents a comparison between results obtained by our proposed blind method with the results obtained using the regularization parameter values found by the manual adjustment, shown in Table 9, in chapter 2.

For this evaluation, we have selected PSNR, SSIM, and the L_1 norm to compare the quality of the restored image. Based on the results shown in Table 19, we noticed that despite manually finding a better combination of regularization parameter values than the ones fixed by PAN, they are not the optimal values that yield the best restoration quality. Furthermore, it is shown that our proposed method yielded a higher restoration quality than the newly manually found combination.

PSF size	Method	PSNR	SSIM	L_1 norm
" Bridge"				
13 × 13	Ours	**29.3216**	**0.9641**	**998.8030**
	PAN	22.1019	0.8099	3036.67
19 × 19	Ours	**22.8250**	**0.8876**	**984.9006**
	PAN	22.3450	0.8826	2880.61
23 × 23	Ours	**25.3792**	**0.8235**	**1193.7**
	PAN	17.6851	0.4424	5175.99
"Photo"				
13 × 13	Ours	23.4926	0.8260	**938.0729**
	PAN	**30.9476**	0.9492	942.86
19 × 19	Ours	**27.6978**	**0.9145**	**1320**
	PAN	27.6787	0.9012	1333.01
23 × 23	Ours	**26.9023**	**0.8794**	**1165.5**
	PAN	21.6381	0.7111	2757.06

Table 19: comparison between results obtained by our proposed blind method with the results obtained using the regularization parameter values found by the manual adjustment

To further evaluate the accuracy of the estimated Point Spread Function (PSF), we conducted an additional quantitative assessment using the kernel similarity criterion [59]. For this evaluation, we utilized the DBS1 [62]. In Figure 14 we present the kernel similarity results for the whole dataset used (32 degraded images) obtained from four different restoration methods from the literature [33, 73-75] as well as our proposed blind method. The kernel similarity metric allows us to compare the similarity between the estimated PSFs of these methods and the ground truth PSF.

After analyzing the results in Table 20, it becomes evident that our proposed blind method surpasses the performance of the other restoration methods. The kernel similarity scores clearly demonstrate that our method achieves a higher level of similarity to the ground truth PSF, indicating its superior capability in accurately estimating the PSF for image restoration.

			[33]	[73]	[74]	[75]	Proposed method
	n°	PSF size	Kernel similarity				
“Photo”	1	13 × 13	0.7880	0.7625	0.7270	**0.8100**	0.7842
	2	15 × 15	**0.8060**	0.6900	0.7230	0.7250	0.7908
	3	17 × 17	**0.8750**	0.8625	0.8270	0.8250	0.8725
	4	19 × 19	0.6700	0.5850	0.5875	0.6400	**0.7440**
	5	21 × 21	0.8820	0.7880	0.7200	0.8125	**0.8882**
	6	23 × 23	**0.8750**	0.5650	0.7700	0.7720	0.8146
	7	23 × 23	0.8125	0.5200	0.7950	0.7950	**0.8160**
	8	27 × 27	0.7590	0.6580	0.6500	0.5000	**0.8433**
“Bridge”	1	13 × 13	**0.8375**	0.7590	0.7005	0.8125	0.8130
	2	15 × 15	0.8060	0.7760	0.7500	0.7250	**0.8506**
	3	17 × 17	0.8750	0.8500	0.8374	0.8510	**0.8804**
	4	19 × 19	0.7000	0.5760	0.6530	0.6050	**0.7668**
	5	21 × 21	0.8250	0.8500	0.8060	0.8300	**0.9128**
	6	23 × 23	0.7790	0.5270	0.7250	0.8127	**0.8925**
	7	23 × 23	0.8010	0.4875	0.8375	0.8770	**0.8915**
	8	27 × 27	0.7760	0.6745	0.6635	0.7700	**0.8954**
“Wall”	1	13 × 13	**0.7930**	0.7780	0.7350	0.7750	0.7435
	2	15 × 15	0.7901	0.7187	0.7125	0.7290	**0.8090**
	3	17 × 17	**0.8760**	0.8625	0.8240	0.8400	0.8684
	4	19 × 19	0.7250	0.6050	0.5625	0.5625	**0.7285**
	5	21 × 21	0.8875	0.8400	0.8130	0.8750	**0.8900**
	6	23 × 23	**0.8500**	0.5800	0.7210	0.7625	0.8211
	7	23 × 23	0.9010	0.5270	0.8400	0.8525	**0.9184**
	8	27 × 27	0.7500	0.6625	0.6625	0.7060	**0.8224**
“Face”	1	13 × 13	**0.8125**	0.7270	0.6850	0.7630	0.7270
	2	15 × 15	0.7620	0.7200	0.6750	0.7220	**0.7689**
	3	17 × 17	0.8500	0.8270	0.8270	0.8270	**0.8576**
	4	19 × 19	0.6625	0.5650	0.5850	0.5375	**0.6681**
	5	21 × 21	0.8600	0.7750	0.7650	0.8250	**0.8642**
	6	23 × 23	**0.8200**	0.7750	0.7550	0.7690	0.7913
	7	23 × 23	**0.8125**	0.7100	0.6650	0.7510	0.7733
	8	27 × 27	0.6875	0.6500	0.6460	**0.7150**	0.6875

Table 20: Kernel similarity Comparison between our proposed method and four methods from the literature [33] [73-75] using DBS1 [62]

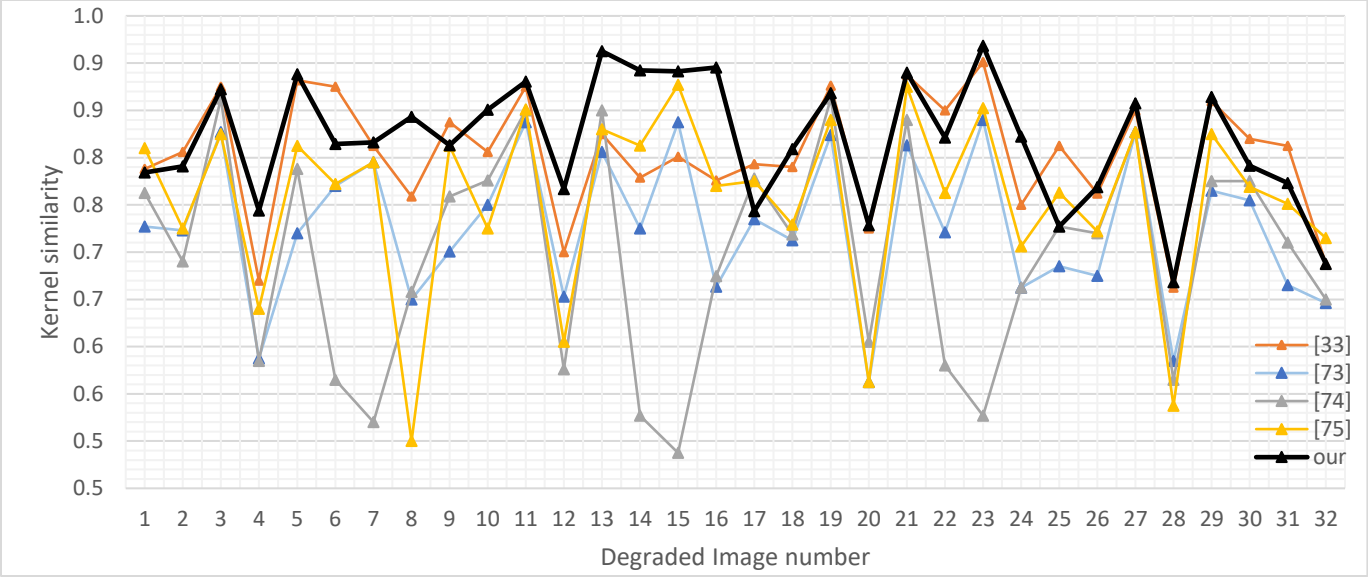

Figure 14: Kernel similarity criterion for the estimated PSF from our proposed method and four methods from the literature [33] [73-75] using DBS1 [62]

5.3. Evaluation using multicomponent images

After validating the superior performance of our proposed method on monochrome images, we proceed to evaluate the developed approach on multicomponent images (RGB). In the case of these images, the same Point Spread Function (PSF) is applied to degrade each component.

Firstly, we utilize two images, namely "Butterfly" and "Lighthouse," sourced from DBS2 [67] and DBS3 [68], respectively, as shown in Figure 15. Each image has a size of 768×512 pixels. we apply a PSF of support size 13×13 obtained from DBS1 [62] to degrade each component of the images.

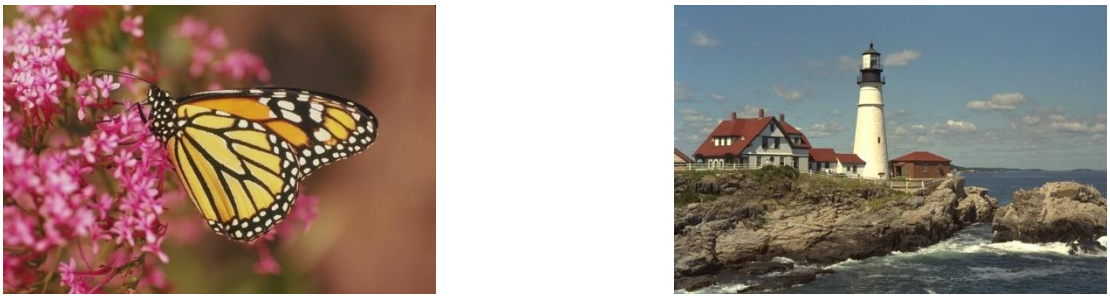

Figure 15: The original "Butterfly"(left) and "Lighthouse"(right) images from DBS2 [67] and DBS3 [68]

We have estimated the PSF from each component (R, G, and B) also we have calculated the average estimated PSF (PSF_{avg}) as follows:

$$\hat{h}_{avg} = \frac{1}{3}\sum_{n=1}^{3} \hat{h}_i \text{ with } i \in \{R, G, B\}$$

The visual results of the PSF estimation for both RGB images can be seen in Table 21. Upon visual inspection, it is difficult to discern any noticeable differences between the estimated PSFs from each component and the average estimated PSF. Therefore, a qualitative assessment is conducted using the L_1 norm of the estimation error and the kernel similarity as evaluation metrics, as shown in Table 22.

Analyzing the results in Table 22, we observe that the L_1 norm of the error estimation and the kernel similarity metrics indicate that there is one estimated PSF that exhibits higher accuracy compared to all other estimations regarding both images. The results also demonstrate that, contrary to expectations, the average PSF does not provide the most accurate estimation.

For instance, in the case of the "Lighthouse" image, the estimated PSF from the Blue component yields the best estimation with an L_1 norm of 0.2382, whereas the average estimated PSF has an L_1 norm of 0.3405. As for the "Butterfly" image, the kernel similarity of the average PSF is 0.9309, slightly higher than the kernel similarity of the estimated PSF from the Green component (0.9212). However, the highest kernel similarity value is obtained by the estimated PSF from the Red component, with a value of 0.9506.

Moreover, to indicate which of the estimated PSFs is the most accurate estimation in a blind manner, Table 23 represents the L_1 nom of the error estimation between the observed degraded image components (R, G, B) with the estimated degraded image components obtained by using the PSFs estimated from R, G, and B components, along with the average estimated PSF.

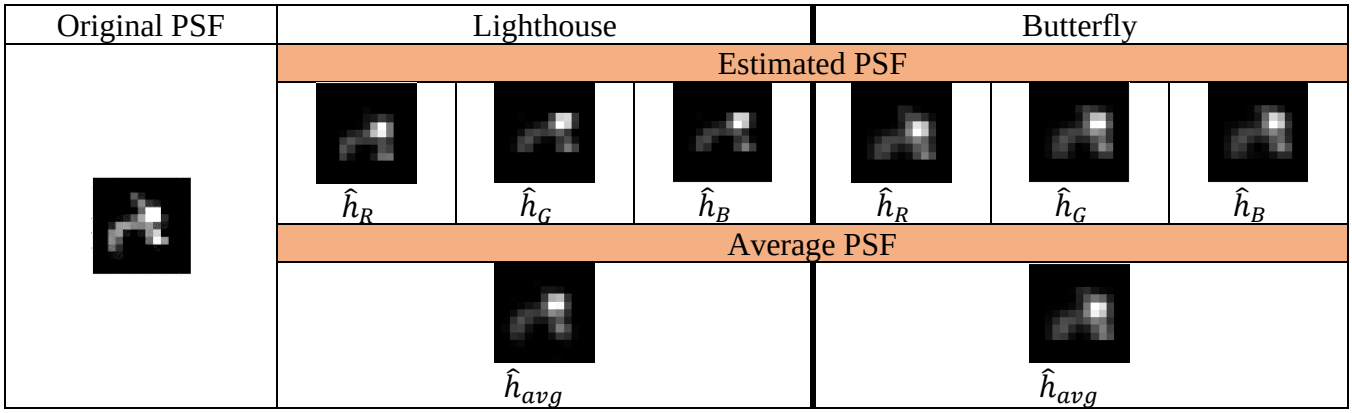

Table 21: Visual evaluation for the estimated PSF from each component and the average estimated PSF for the "Lighthouse" and "Butterfly" images degraded by the original PSF of support size 13×13

Lighthouse	L_1 norm	$\|h - \hat{h}_R\|_1$	$\|h - \hat{h}_G\|_1$	$\|h - \hat{h}_B\|_1$	$\|h - \hat{h}_{avg}\|_1$
		0.5098	0.2734	**0.2382**	0.3405
	Kernel similarity	KS_R	KS_G	KS_B	KS_{avg}
		0.8926	0.9760	**0.9812**	0.9300
Butterfly	L_1 norm	$\|h - \hat{h}_R\|_1$	$\|h - \hat{h}_G\|_1$	$\|h - \hat{h}_B\|_1$	$\|h - \hat{h}_{avg}\|_1$
		0.4334	0.4880	0.4451	0.4555
	Kernel similarity	KS_R	KS_G	KS_B	KS_{avg}
		0.9506	0.9212	0.9484	0.9309

Table 22: Qualitative evaluation of the estimated PSF of each component and the average estimated PSF for the "Lighthouse" and "Butterfly" images using the L_1 norm of the error estimation and the kernel similarity as evaluation criteria

Image	L_1 norm: $\|g - \hat{g}\|_1$			
" Lighthouse"	Red component			
	$\|g_R - \hat{g}_{R_R}\|_1$	$\|g_R - \hat{g}_{R_G}\|_1$	$\|g_R - \hat{g}_{R_B}\|_1$	$\|g_R - \hat{g}_{R_{avg}}\|_1$
	3.1681×10^4	2.4812×10^4	$\mathbf{2.1353 \times 10^4}$	4.1264×10^4
	Green component			
	$\|g_G - \hat{g}_{G_R}\|_1$	$\|g_G - \hat{g}_{G_G}\|_1$	$\|g_G - \hat{g}_{G_B}\|_1$	$\|g_G - \hat{g}_{G_{avg}}\|_1$
	3.1053×10^4	2.6934×10^4	$\mathbf{2.2551 \times 10^4}$	4.2616×10^4
	Blue components			
	$\|g_B - \hat{g}_{B_R}\|_1$	$\|g_B - \hat{g}_{B_G}\|_1$	$\|g_B - \hat{g}_{B_B}\|_1$	$\|g_B - \hat{g}_{B_{avg}}\|_1$
	3.3659×10^4	2.7486×10^4	$\mathbf{2.3764 \times 10^4}$	4.2876×10^4
" Butterfly"	Red component			
	$\|g_R - \hat{g}_{R_R}\|_1$	$\|g_R - \hat{g}_{R_G}\|_1$	$\|g_R - \hat{g}_{R_B}\|_1$	$\|g_R - \hat{g}_{R_{avg}}\|_1$
	$\mathbf{2.4424 \times 10^4}$	2.76564×10^4	2.7446×10^4	3.0255×10^4
	Green component			
	$\|g_G - \hat{g}_{G_R}\|_1$	$\|g_G - \hat{g}_{G_G}\|_1$	$\|g_G - \hat{g}_{G_B}\|_1$	$\|g_G - \hat{g}_{G_{avg}}\|_1$
	$\mathbf{2.5118 \times 10^4}$	2.7946×10^4	2.9924×10^4	3.0697×10^4
	Blue components			
	$\|g_B - \hat{g}_{B_R}\|_1$	$\|g_B - \hat{g}_{B_G}\|_1$	$\|g_B - \hat{g}_{B_B}\|_1$	$\|g_B - \hat{g}_{B_{avg}}\|_1$
	$\mathbf{2.5927 \times 10^4}$	2.7486×10^4	2.6000×10^4	3.0981×10^4

Table 23: Evaluation of the L_1 norm of the error estimation between the observed degraded image and the estimated degraded image for both "Lighthouse" and "butterfly" images

Looking in Table 23, we can notice that the most accurate PSF estimation for the "Lighthouse" image is the from the blue components, where the L_1 norm between the observed degrade R, G and B components and the estimated degraded image using the PSF estimated from the blue component gave the lowest value. Regarding the "Butterfly" image, the PSF estimated from the red component gave the lowest L_1 norm value. These results confirm the results obtained in Table 22.

After evaluating the estimated PSFs, it was determined that the estimated PSF from the Blue component provides the most accurate estimation for the image "Lighthouse", while the estimated PSF from the Red component is the most accurate for the "Butterfly" image. We compare, in Table 24, the restoration results using the most accurate estimated PSF for each image with the restoration results obtained using each estimated PSF to restore its respective component. Additionally, we include the restoration results obtained using the average PSF for comparison.

In Table 24, we present the results obtained using the evaluation criteria of PSNR and SSIM. The analysis of the results reveals that the best image restoration outcomes are achieved when utilizing the most accurate PSF for both the "Lighthouse" and "Butterfly" images, respectively. These results highlight the effectiveness of using the most accurate PSF estimation in achieving superior image restoration quality.

		Most accurate Estimated PSF		Appropriate estimated PSF		Average estimated PSF	
	Restored image	PSNR	SSIM	PSNR	SSIM	PSNR	SSIM
“Lighthouse”	$\hat{f}_R$	**24.2029**	**0.8283**	22.0331	0.7059	24.1528	0.7985
	$\hat{f}_G$	**24.0023**	**0.8245**	23.1457	0.8096	24.0549	0.7949
	$\hat{f}_B$	**24.2981**	**0.8473**	24.2981	0.8473	20.1346	0.7511
	$\hat{f}_{RGB}$	**24.3660**	**0.8876**	23.0612	0.8443	22.3485	0.7592
“Butterfly”	$\hat{f}_R$	**23.3033**	**0.8577**	20.3033	0.8577	20.9401	0.8763
	$\hat{f}_G$	**25.5007**	**0.8836**	21.5242	0.8513	22.2208	0.8704
	$\hat{f}_B$	**25.5090**	**0.8954**	22.2588	0.8405	23.0102	0.8609
	$\hat{f}_{RGB}$	**26.1700**	**0.9556**	21.2862	0.9350	21.9721	0.9448

Table 24: Comparing the restoration result using the most accurate PSF, the appropriate estimated PSF from each component and the average PSF based on the PSNR and SSIM metrics

After obtaining these results, we proceeded to compare the restoration of these two RGB images with four methods from the literature [33] [73-75]. The comparison was based on the evaluation criteria of PSNR and SSIM, as shown in Table 25. By comparing the restoration results using these metrics, we were able to assess the performance and effectiveness of the proposed method in relation to the existing methods from the literature.

Following this qualitative evaluation, we present in Figure 16 the visual assessment of the two restored RGB images obtained using our proposed method, as well as the four methods from the literature [33] [73-75]. Upon observing the visual evaluation, it is evident that our proposed method exhibits the highest visual quality for both restored images. The images restored using our method showcase superior visual fidelity and clarity compared to the results obtained from the other methods. This visual confirmation further supports the conclusion that our proposed method outperforms the existing methods from the literature in terms of visual restoration quality.

Image	Evaluation metric	[33]	[73]	[74]	[75]	Our proposed method
“Lighthouse	PSNR	24.02	22.58	19.96	23.51	**24.37**
	SSIM	0.8073	0.7787	0.6475	0.7924	**0.8876**
“Butterfly”	PSNR	26.11	21.71	17.48	25.08	**26.17**
	SSIM	0.9552	0.9147	0.8355	0.9458	**0.9556**

Table 25: qualitative comparison between out proposed method and four methods from the literature for the restoration of the “Lighthouse” and “Butterfly” images using PSNR and SSIM

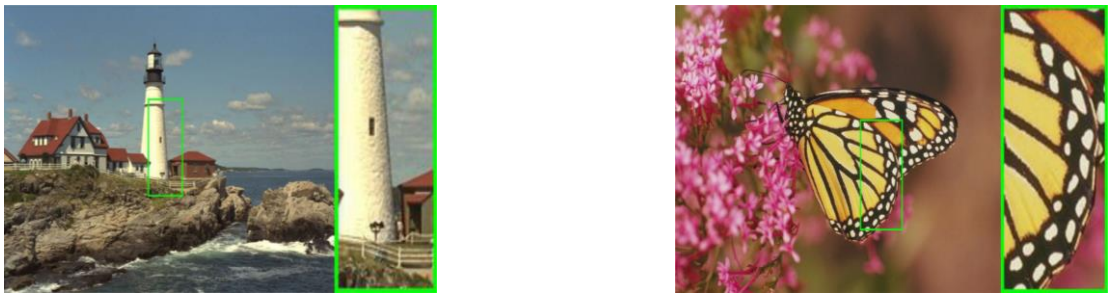

(a) Original images (left: lighthouse, right: butterfly)

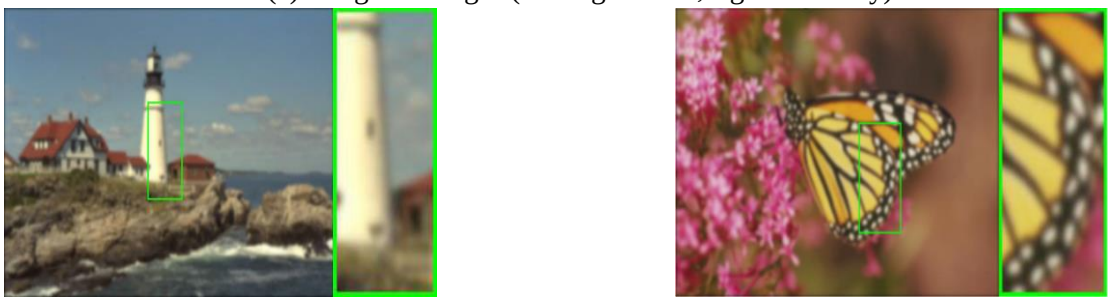

(b) Blurred images (left: lighthouse, right: butterfly)

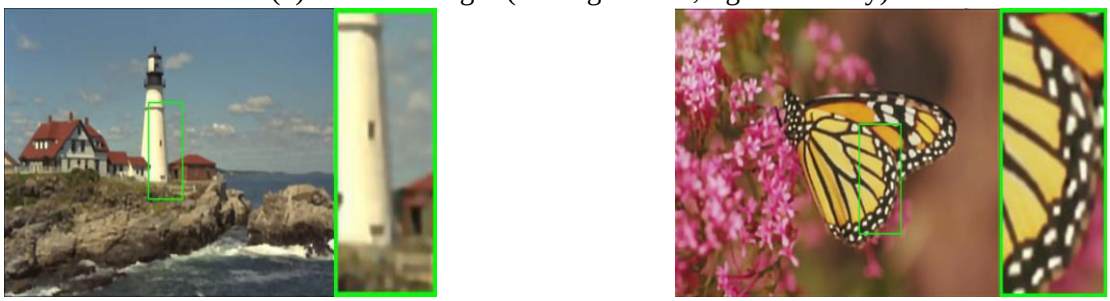

(c) Restored images by Zhou L. et al. [33] (left: lighthouse, right: butterfly)

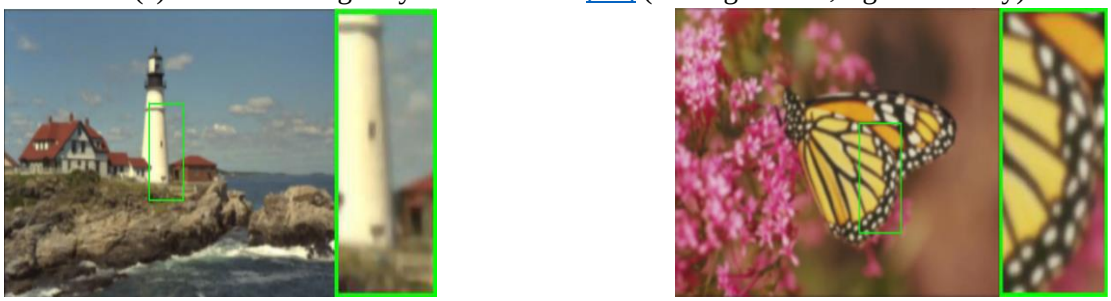

(d) Restored images by Zhou L. et al. [73] (left: lighthouse, right: butterfly)

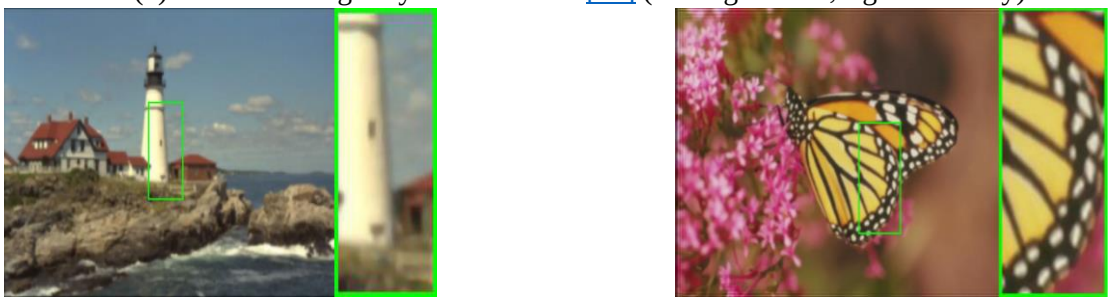

(e) Restored images by Zhong L. et al. [74] (left: lighthouse, right: butterfly)

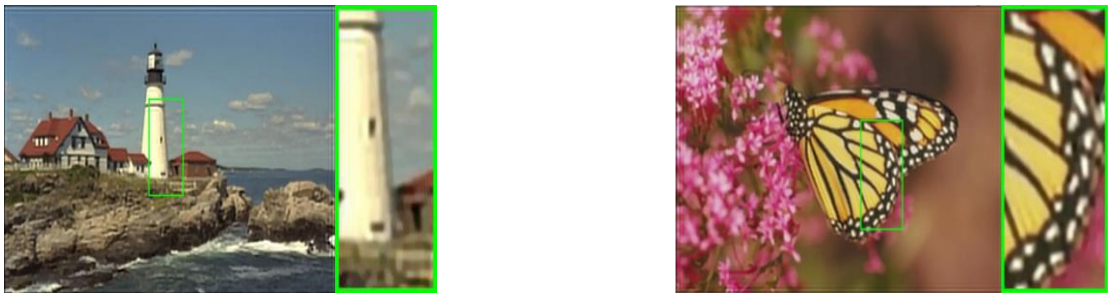

(f) Restored images by Elmi S Y et al. [75] (left: lighthouse, right: butterfly)

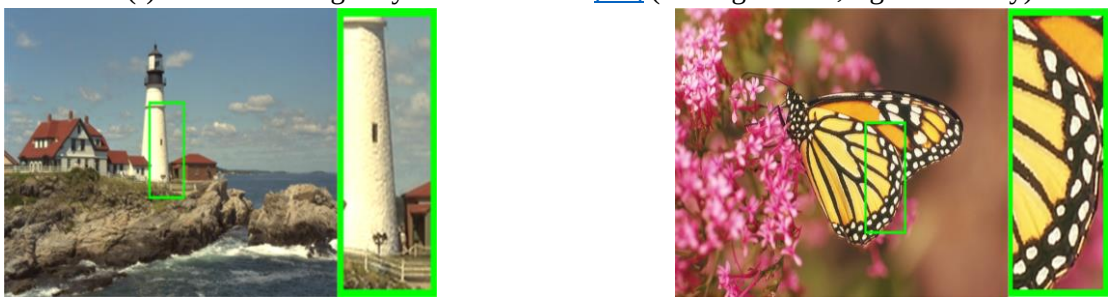

(g) Restored images by our proposed method (left: lighthouse, right: butterfly)

Figure 16: Visual comparison of the restored image between our proposed method and four methods from the literature using the "Lighthouse" (left) and the "Butterfly" (right) images

5.4. Evaluation using Hyperspectral images

The previous evaluation of RGB images has demonstrated that, despite degrading each component using the same PSF, the accuracy level of the estimated PSF differs across the components. Furthermore, employing the most accurate PSF to restore all components leads to superior image restoration results.

Moreover, when the most accurate PSF estimation was utilized for the restoration of all components, it resulted in improved image restoration compared to using component-specific PSFs or an average PSF.

Therefore, in the evaluation of hyperspectral images, we intend to examine the two proposed strategies for restore a full hyperspectral image.

5.4.1. Evaluation of the first strategy

To assess the first strategies, we utilized a synthetic Hyperspectral Image (HSI) comprising 100 spectral components with a size of 60×60 pixels. Each component underwent degradation using two different motion blurs of different support sourced from DBS1 dataset [62]. Additionally, a Gaussian blur with a standard deviation of 1.5 and a support size of 9×9 was also applied.

By implementing the unsupervised partitioning method [76], we blindly grouped the spectral components into five distinct groups. Each group was represented by a specific exemplar component. These exemplar components were employed for estimating the Point Spread Function (PSF) associated with each group. Subsequently, the estimated PSFs were utilized to restore all the spectral components belonging to their respective groups.

Figure 17 shows the synthetic HSI used in RGB mode and the correlation matrix between all spectral components, indicating the different correlation groups blindly formed by the UP-OAP method. Table 26

provides details of each formed group, indicating the range of spectral components included in each group, along with the exemplary spectral component selected to represent each group in the PSF estimation phase.

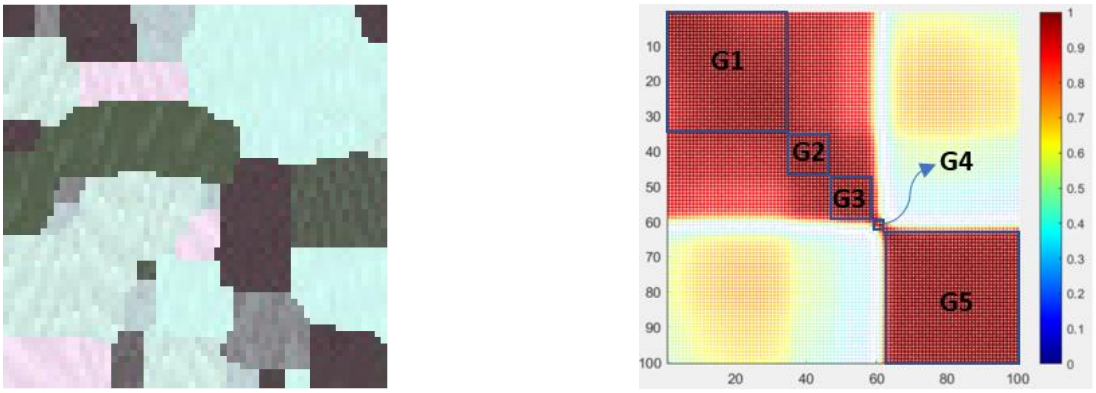

Figure 17: The synthetic HSI in RGB mode (left) and the correlation matric between all spectral component of our HSI (right)

Spectral group	G1	G2	G3	G4	G5
Range of spectral components	1-34	35-47	48-58	59-61	62-100
Exemplar	B18	B39	B50	B60	B88

Table 26: Correlated groups and their exemplar spectral component for the first strategy

In the PSF estimation phase we have only used the selected spectral components of each group to estimate the PSF. A visual evaluation was performed shown in Table 27, representing the estimated PSF of support size 9×9, 13×13, and 19×19. The visual assessment shows no difference between the estimated PSF therefore a qualitative evaluation was performed based on the L_1norm of the error estimation of the PSF shown in Table 27.

PSF Size	9×9	13x13	19x19
Original PSF (h)		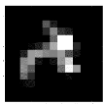	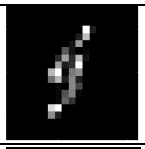
Estimated PSF $(\hat{h}_{18})$ from B18			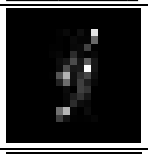
Estimated PSF $(\hat{h}_{39})$ from B39			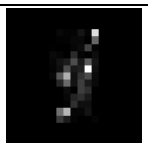
Estimated PSF $(\hat{h}_{50})$ from B50			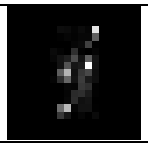

Estimated PSF ($\hat{h}_{60}$) from B60			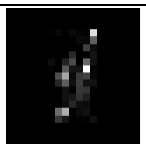
Estimated PSF $(\hat{h}_{88})$ from B88			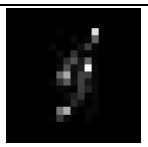

Table 27: Estimated PSF from each exemplar

PSF size	9×9	13×13	19×19
$\|h - \hat{h}_{18}\|_1$	0.1071	0.2348	0.3739
$\|h - \hat{h}_{39}\|_1$	0.0713	0.3271	0.4772
$\|h - \hat{h}_{50}\|_1$	0.1124	0.3746	0.5133
$\|h - \hat{h}_{60}\|_1$	0.1034	0.7404	0.4819
$\|h - \hat{h}_{88}\|_1$	0.0515	0.1850	0.2789

Table 28: Qualitative evaluation of the estimated PSF from the exemplar spectral components using the L_1 norm

After obtaining the PSF estimation from the exemplar spectral component of each group, we applied the estimated PSF to restore all the spectral components belonging to their respective groups.

To assess the effectiveness of our first proposed strategy, we conducted a visual evaluation, as depicted in Table 29. The table showcases the original, degraded, and restored RGB mode images of three exemplar components (B18, B50, and B60) using different PSF sizes. The visual evaluation demonstrates that our proposed method successfully restores the original colors and details, resulting in a visually enhanced image representation compared to the degraded and original one image

In addition to the visual evaluation, we also employed quantitative measures to evaluate the restoration quality. Three criteria were considered: Mean Peak Signal-to-Noise Ratio (MPSNR), Mean Structural Similarity Index Measure (MSSIM), Mean L_1 norm of the estimation error, and Mean Root Mean Squared Error (MRMSE). These metrics provide measurements of the fidelity and accuracy of the restoration process.

Table 30 presents the results of the qualitative evaluation for the different PSF sizes used in the restoration. The obtained values for MPSNR, MSSIM, L_1 norm of the estimation error, and MRMSE indicate the high quality of the restored hyperspectral image. The proposed method effectively preserves the important spectral and spatial information, resulting in accurate restorations.

Lastly, in order to further validate our results, Table 31 depicts the comparison of the original, degraded, and restored spectral signatures of different pixel coordinated $\{(1,1), (34,8), (60,14)\}$ for the three degradation functions used 9×9, 13×13,and 19×19.

Upon careful examination, we can observe that the restored spectral signature closely resembles the original spectral signature, specially at the spectral component 71, where we were able to precisely recover the important information lost during the degradation. This indicates that our proposed method successfully recovers the spectral information that was lost during the degradation process. The restored

spectral signature demonstrates the accuracy and reliability of our restoration approach, providing further evidence of the effectiveness of our method.

Based on the analysis of the spectral signature, it has been observed that the last ten spectral components exhibit significant fluctuations. These fluctuations suggest the presence of acquisition noise without any substantial information. Consequently, in the second suggested strategy, we will exclude these ten spectral components.

PSF size	Original RGB	degraded RGB	restored RGB
9 × 9		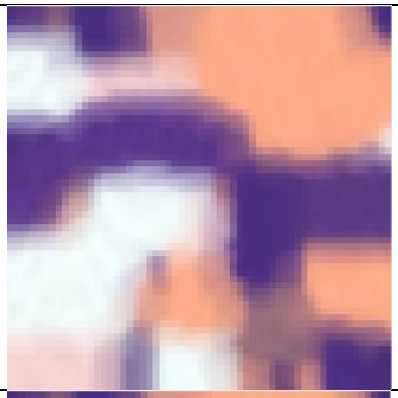	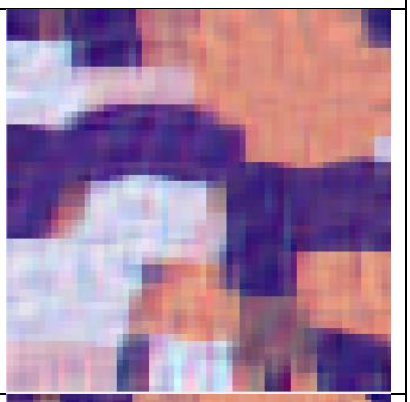
13 × 13		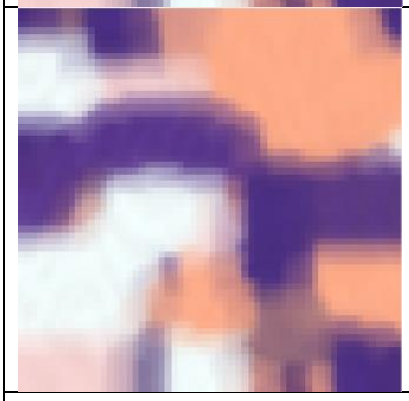	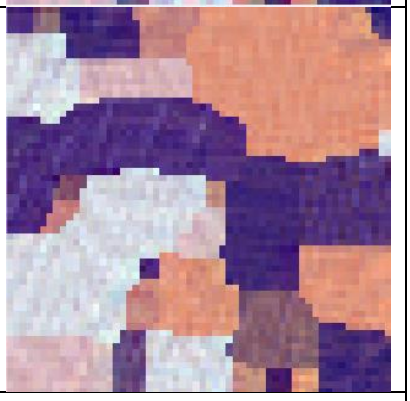
19 × 19		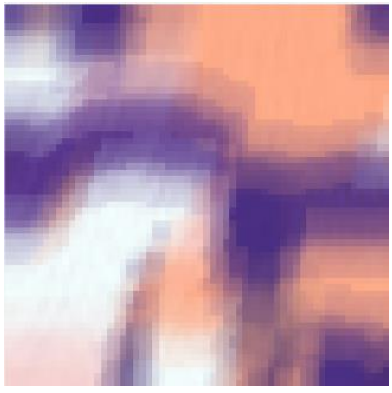	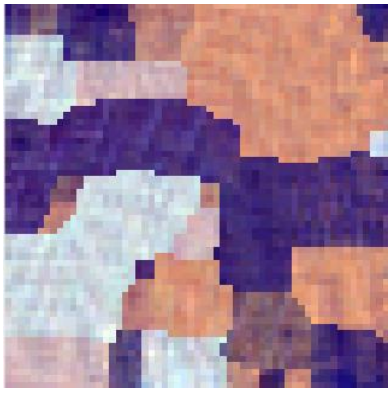

Table 29: visual representation of the original, degraded, and restored HSI shown in RGB mode using the spectral component B18, B50 and B60

PSF size	MPSNR	MSSIM	ML_1 norm	MRMSE
9×9	47.003	0.9805	201.0475	1.2128
13×13	39.2026	0.9148	166.2662	2.9392
19×19	40.3858	0.9384	179.6001	2.4565

Table 30: Qualitative evaluation of the full HSI for the three PSF used, utilizing the MPSNR, MSSIM, L_1norm, and MRMSE as evaluation metrics.

PSF size	9×9	13×13	19×19
Pixel (1,1)	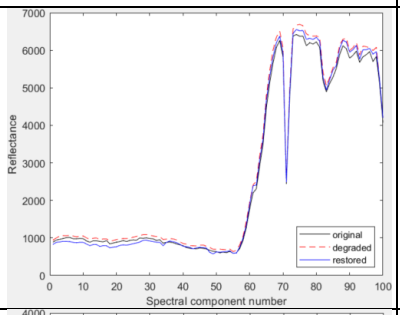	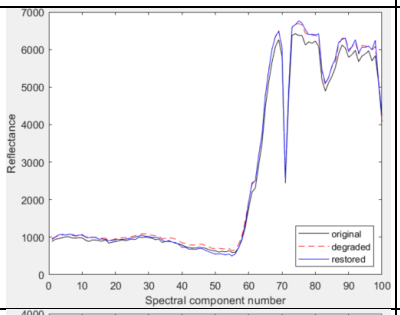	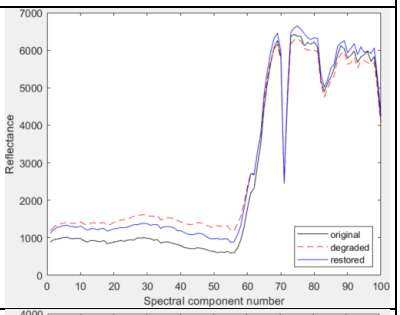
Pixel (34,8)	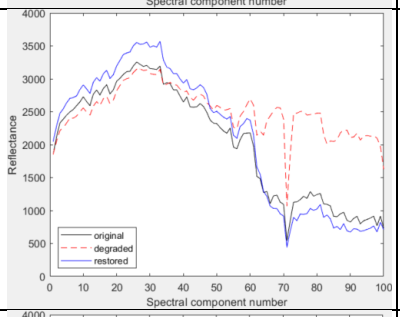	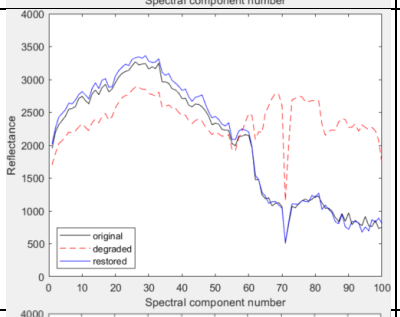	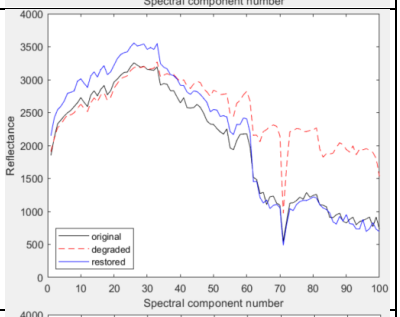
Pixel (60,14)	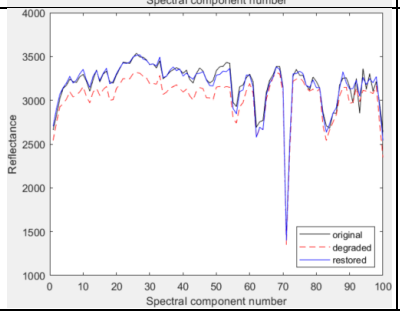	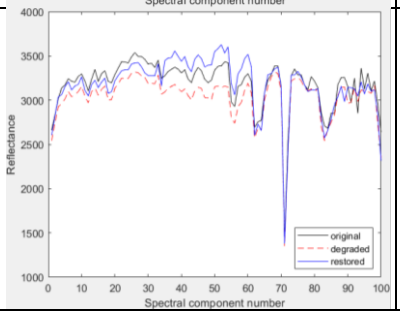	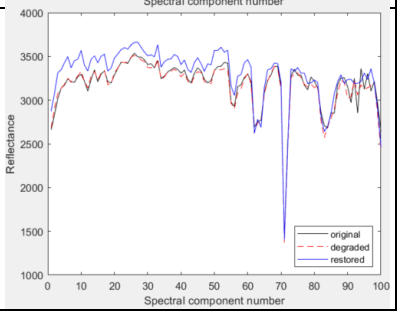

Table 31: Comparison between the original, degraded and restored spectral signature of three different pixel coordinates using three different PSF functions of different support sizes

5.4.2. Evaluation of the second strategy

In the second strategy, we proceeded by eliminating the last ten spectral components due to the hight alternation in the spectral signature and less informative spectral components. By eliminating them, we aim to improve the overall quality and accuracy of the restoration process. This strategic decision allows us to focus on the more relevant spectral components, which are expected to contribute significantly to the restoration of the hyperspectral image.

By applying the partitioning method described in [76], we obtained five correlation groups, which differed in their partitioning of spectral components and the selection of exemplar components compared to the first strategy.

Figure 18 illustrates the new correlation map. Additionally, Table 32 provides a detailed overview of the content of each group and specifies the exemplar component chosen to represent it.

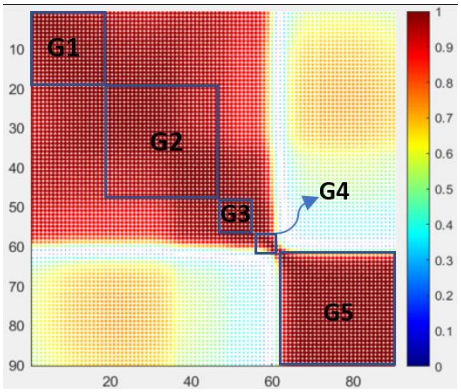

Figure 18: The new correlation map between all spectral components after eliminating the last ten spectral components

Spectral group	G1	G2	G3	G4	G5
Range of spectral components	1-19	20-47	48-56	57-61	62-90
Exemplar	B11	B38	B49	B58	B85

Table 32: Correlated groups and their exemplar spectral component for the first strategy

After partitioning the spectral components, we proceeded with the estimation of the Point Spread Function (PSF) using only the exemplar spectral components indicated in Table 32. We utilized the same PSFs as in the first strategy. The estimation results of the PSF are presented in Table 33.

A qualitative assessment was conducted to evaluate the accuracy of the estimated PSFs for the exemplar spectral components. This assessment considered the L_1 norm of the estimation error for the estimated PSFs and the estimated degraded image.

Table 34 displays the results of the assessment based on the L_1 norm of the estimation error for the estimated PSFs with support sizes of 9×9, 13×13, and 19×19. The values obtained were 0.0460, 0.1847, and 0.3056, respectively. Notably, the exemplar B85 exhibited the lowest estimation errors for all three PSFs, indicating a more accurate estimation. Conversely, the exemplar B58 had the highest estimation errors for the PSFs with support sizes of 9×9 and 13×13, with values of 0.1051 and 0.3654, respectively. The exemplar B11 showed the highest estimation error for the PSF with a support size of 19×19, with a value of 0.9719.

Table 35 presents the L_1 norm values of the error estimation between the observed degraded exemplar spectral component and the estimated degraded exemplar spectral component using the estimated PSFs with support sizes of 9×9, 13×13, and 19×19. These results further confirm that the most accurate estimation is achieved when using the exemplar spectral component B85. For each estimated degraded exemplar spectral component, the L_1 norm values are 1.5417×10^4, 1.8159×10^4, and 2.0102×10^4, respectively. These values indicate a close resemblance between the observed spectral component and the estimated degraded spectral component, validating the accuracy of the PSF estimation process using the B85 exemplar spectral component.

Based on the results presented in Tables 34 and 35, we can conclude that the most accurate estimation for the three PSFs with support sizes of 9×9, 13×13, and 19×19 is achieved when utilizing the exemplar

spectral component B85. Therefore, for the restoration of the full hyperspectral image, we will exclusively employ the most accurate estimated PSF obtained from B85.

PSF Size	9×9	13x13	19x19
Original PSF (h)		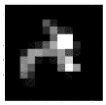	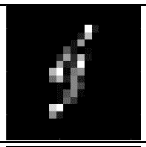
Estimated PSF $(\hat{h}_{11})$ from B11			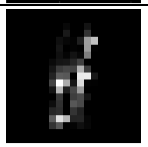
Estimated PSF $(\hat{h}_{38})$ from B38			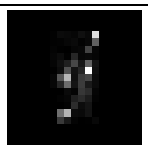
Estimated PSF $(\hat{h}_{49})$ from B49			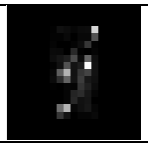
Estimated PSF $(\hat{h}_{58})$ from B58			
Estimated PSF $(\hat{h}_{85})$ from B85			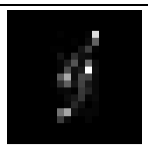

Table 33: visual evaluation of the estimated PSF of the exemplar spectral components

PSF size	9×9	13×13	19×19
$\|h - \hat{h}_{11}\|_1$	0.0517	0.2092	0.9719
$\|h - \hat{h}_{38}\|_1$	0.0594	0.3251	0.4689
$\|h - \hat{h}_{49}\|_1$	0.1026	0.3334	0.4932
$\|h - \hat{h}_{58}\|_1$	0.1051	0.3654	0.5074
$\|h - \hat{h}_{85}\|_1$	**0.0460**	**0.1847**	**0.3056**

Table 34: Qualitative evaluation of the estimated PSFs of the exemplar spectral components using the L_1 norm of the error estimation

PSF size	9×9	13×13	19×19
$\|g_{11} - \hat{g}_{11}\|_1$	1.3936×10^4	1.9894×10^4	4.2004×10^4
$\|g_{38} - \hat{g}_{38}\|_1$	1.9052×10^4	2.5728×10^4	3.9480×10^4
$\|g_{49} - \hat{g}_{49}\|_1$	1.9017×10^4	2.3532×10^4	3.7629×10^4
$\|g_{58} - \hat{g}_{58}\|_1$	1.5777×10^4	2.1772×10^4	3.1886×10^4
$\|g_{85} - \hat{g}_{85}\|_1$	$\mathbf{1.5417 \times 10^4}$	$\mathbf{1.8159 \times 10^4}$	$\mathbf{2.0102 \times 10^4}$

Table 35: Qualitative evaluation of the estimated degraded exemplar spectral components using the L_1 norm of the error estimation

After analyzing the estimated Point Spread Functions (PSFs) obtained in the second strategy, we selected the most accurate estimated PSF to restore all the spectral components of our degraded hyperspectral image.

The first assessment involves a visual comparison of the hyperspectral image restoration between the first and second strategies. Table 35 illustrates the original hyperspectral image visualized in RGB mode using the spectral components B18, B50, and B60, along with its restoration using both the first and second strategies for three different PSF functions with support sizes of 9×9, 13×13, and 19×19.

Upon visual inspection, it is apparent that in the case of the PSF with a support size of 13×13, the restored image using the first strategy exhibits blurriness on the right side, which is not observed in the second strategy. Additionally, when considering the restored image using the first strategy with a PSF of support size 19×19, a difference in pixel intensity is noticeable, resulting in a difference in color compared to the original image. This difference can be attributed to the lower estimation accuracy of the PSF obtained from the exemplar spectral component B11, as indicated in Tables 33-35. Conversely, the restored image using the second strategy demonstrates significant improvements and better definition.

A comprehensive comparison was conducted between the first and second strategies using four evaluation metrics: Mean Peak Signal-to-Noise Ratio (MPSNR), Mean Structural Similarity Index Measure (MSSIM), mean L_1 norm of the estimation error, and Mean Root Mean Squared Error (MRMSE). The results, as presented in Table 37, clearly demonstrate the superior performance of the second strategy across all evaluated metrics. The second strategy consistently outperforms the first strategy, indicating its effectiveness in achieving higher restoration accuracy and fidelity.

In addition to the quantitative evaluation, a qualitative assessment was performed on the spectral signatures of seven different pixel coordinates $\{(1,1), (,1,19), (31,6), (31,9), (34,8), (60,14), (60,23)\}$. The evaluation aimed to compare the original spectral signatures with the degraded and restored (first strategy) spectral signatures, as well as the restored spectral signatures obtained through the second strategy. The findings, illustrated in Table 38, reveal the notable success of the second strategy in accurately recovering the spectral signatures of these pixel coordinates. The spectral signatures restored using the second strategy exhibit remarkable similarity to the original signatures, surpassing the quality of the degraded and restored (first strategy) spectral signatures.

PSF size	Original RGB	First strategy	Second strategy
9 × 9			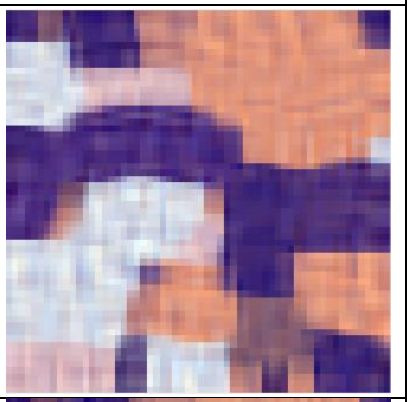
13 × 13		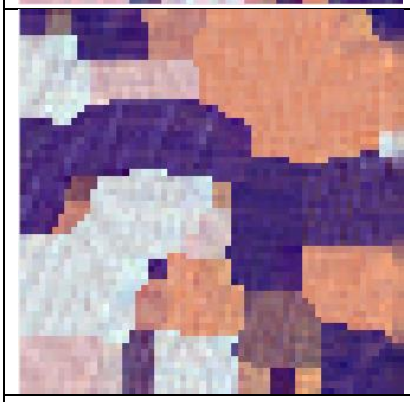	
19 × 19		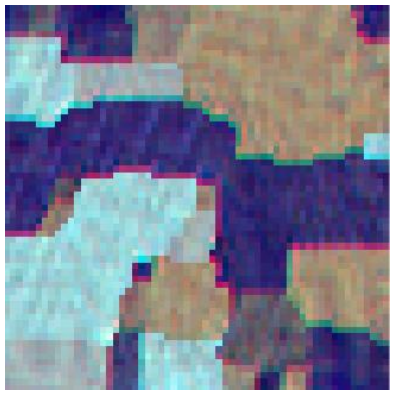	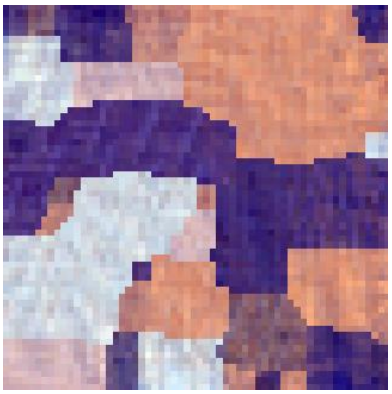

Table 36: visual comparison between the 1st and 2nd strategy for the original, degraded, and restored HSI shown in RGB mode using the spectral component B18, B50 and B60

PSF size	MPSNR		MSSIM		ML_1 norm		MRMSE	
	1st strategy	2nd strategy	1st strategy	2nd strategy	1st strategy	2nd strategy	1st strategy	2nd strategy
9 × 9	47.7992	**47.8180**	0.9825	**0.9828**	195.06	**194.57**	1.1130	**1.1109**
13 × 13	39.5419	**41.2643**	0.9257	**0.9445**	151.63	**135.65**	2.7773	**2.3460**
19 × 19	39.5586	**41.0850**	0.9301	**0.9408**	194.87	**172.88**	2.7652	**2.3986**

Table 37: Qualitative comparison between the 1st and 2nd strategies of the full HSI for the three PSF used, utilizing the MPSNR, MSSIM, ML_1norm, and MRMSE as evaluation metrics.

PSF size	9 × 9	13 × 13	19 × 19
Pixel (1,1)	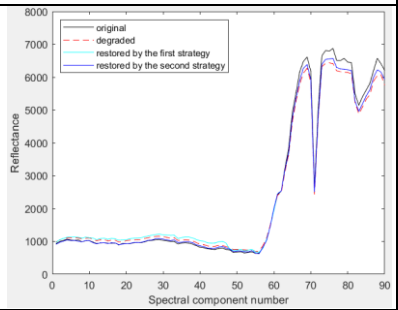	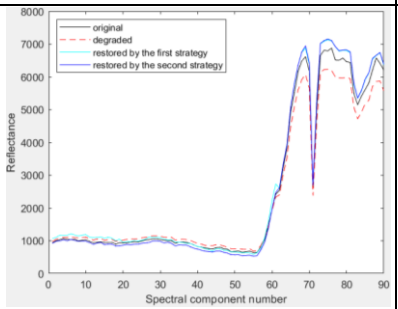	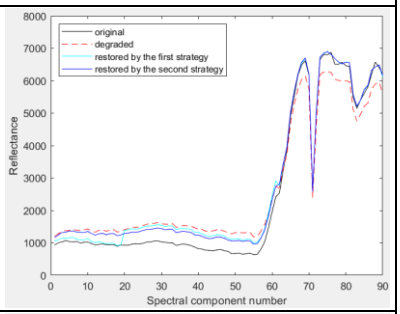
Pixel (1,19)	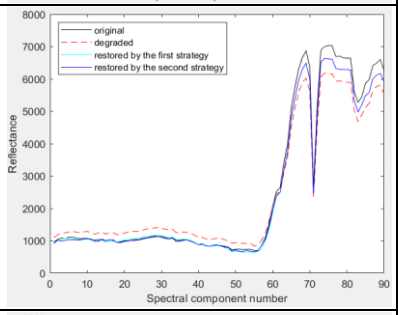	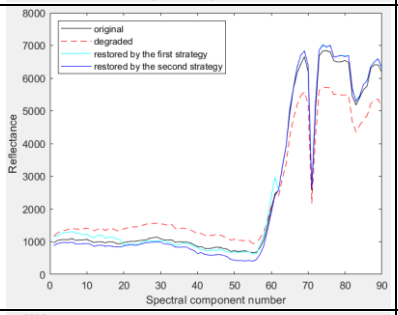	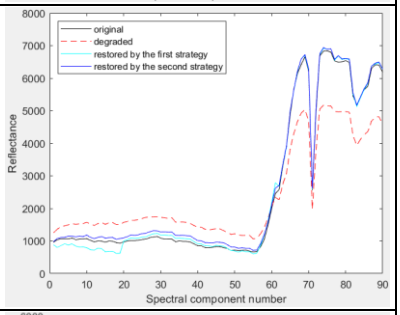
Pixel (31,6)	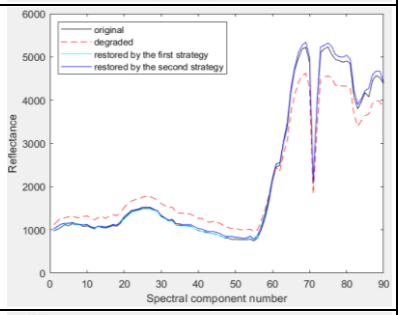	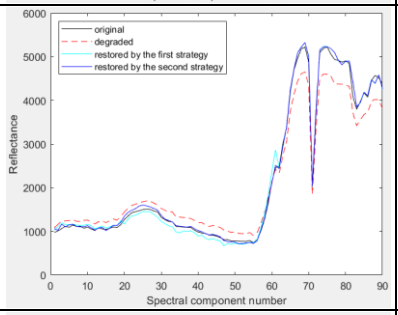	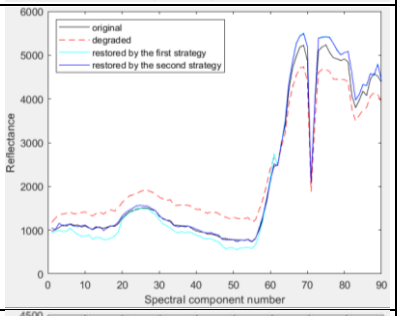
Pixel (31,9)	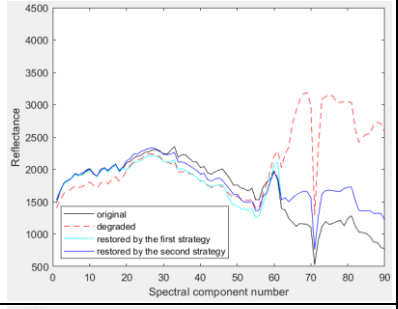	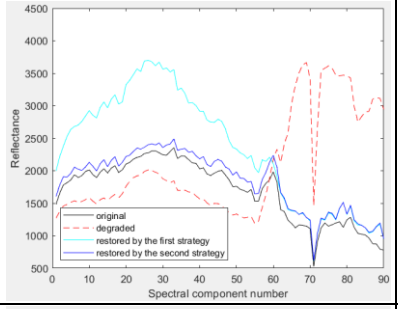	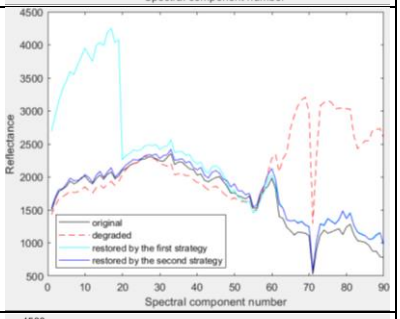
Pixel (34,8)	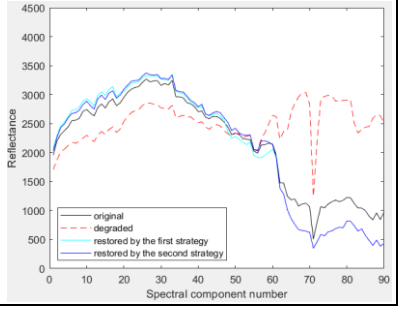	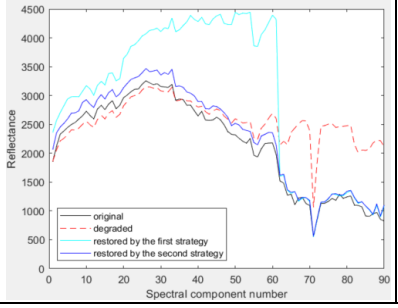	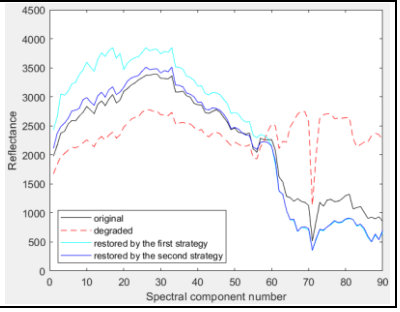

Pixel (60,14)	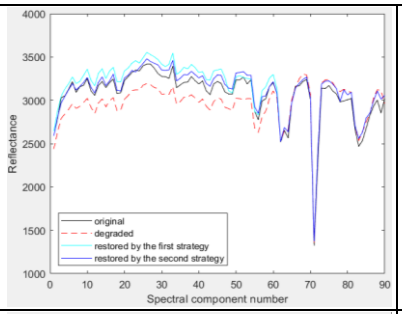	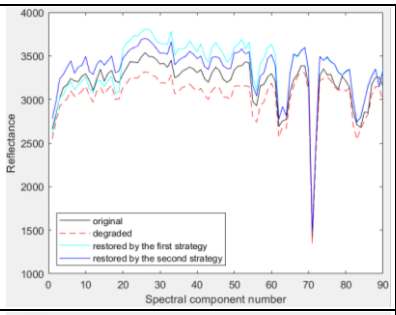	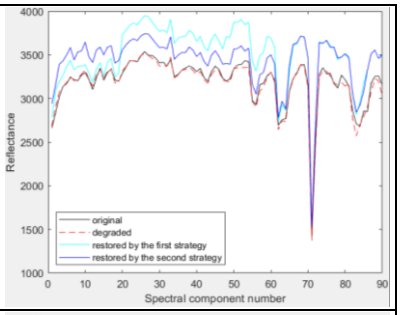
Pixel (60,23)	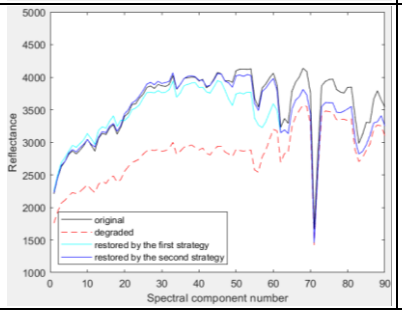	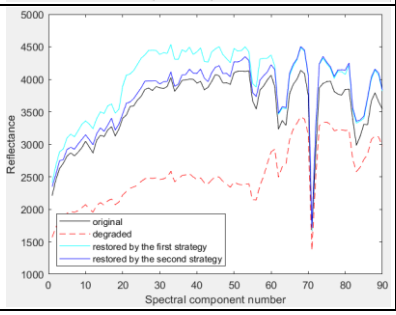	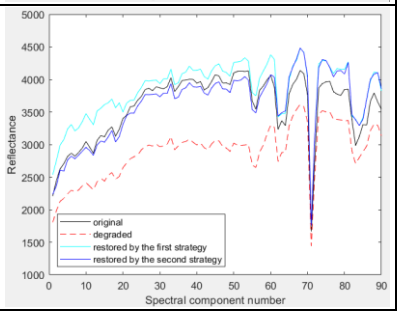

Table 38: Comparison of the original, degraded and restored spectral signature (1st and 2nd strategy) for seven different pixel coordinates using three different PSF functions of different support sizes

These combined evaluation results substantiate the effectiveness and superiority of the second strategy in achieving highly accurate and reliable restoration of the spectral signatures. Using the most accurate estimated PSF consistently provides superior results, enabling the better recovery of spectral information in the degraded hyperspectral image, thus demonstrating its significant advantages over the first strategy.

5.4.3. Comparing the proposed strategy with the recent developed methods of the literature

After conducting a thorough evaluation of the two strategies proposed for hyperspectral image restoration, we now turn our attention to comparing the second strategy with recent methods available in the literature. This comparative analysis aims to assess the performance and effectiveness of the second strategy in relation to other state-of-the-art approaches. We have chosen methods that focus on super resolution [47] that aims to improve the image quality in both spatial and spectral domains and compare the image quality obtained by super resolution with the one obtained by our blind image restoration method.

To facilitate a comprehensive comparison, we selected two hyperspectral images from different datasets. The first image, named "TOY", was chosen from the DBS4 dataset [69], while the second image, named "HARV", was obtained from the DBS5 dataset [71]. In order to conduct a meaningful comparison with the recent method proposed in [47], we employed the same degradation function utilized in their experiments. Specifically, we applied a Gaussian blur with a standard deviation of $\sqrt{2}$ and a support size of 9×9 to both of the selected images. Furthermore, we implemented the suggested unsupervised partitioning method described in reference [76] on the two chosen images. As a result, the image "TOY" yielded three correlation groups, while the image "HARV" produced four correlated groups. Detailed information regarding this partitioning process can be found in Table 39 for the "TOY" image and Table 40 for the "HARV" image.

"TOY"			
Spectral group	G1	G2	G3
Range of spectral components	1-12	13-20	21-31
Exemplar	B5	B17	B24

Table 39: Correlated groups and their exemplar spectral component for the "TOY" image

"HARV"				
Spectral group	G1	G2	G3	G4
Range of spectral components	1-4	5-11	12-19	20-31
Exemplar	B3	B8	B15	B24

Table 40: Correlated groups and their exemplar spectral component for the "HARV" image

In line with our second strategy, we conducted an evaluation of the estimated PSF derived from each selected exemplar spectral component for both images. The evaluation process involved the utilization of two criteria: the L_1 norm of the error estimation.

For the "TOY" image, the evaluation results revealed that the estimated PSF obtained from the exemplar spectral component five ($\hat{h}_{B5}$) demonstrated the highest level of accuracy. It exhibited an L_1 norm of 0.2054, indicating a remarkably close approximation to the true PSF. Furthermore, the kernel similarity score for this estimated PSF was calculated to be 0.9840, further affirming its accuracy and similarity to the ideal PSF.

As for the "HARV" image, we discovered that the estimated PSF derived from the exemplar spectral component eight, denoted as $\hat{h}_{B8}$, yielded the most accurate result according to the evaluation metrics. This estimated PSF possessed an L_1 norm value of 0.5502, implying a reasonably accurate approximation of the true PSF for this image. The kernel similarity score for this PSF estimation was determined to be 0.8944, showing a significant degree of similarity between the estimated PSF and the ground truth PSF.

As suggested in the second strategy, we will use the most accurate PSFs, $\hat{h}_{B5}$ and $\hat{h}_{B8}$ to restore the degraded hyperspectral images "TOY" and "HARV" respectively.

A comparison of results is conducted for the two images displayed in Table 41. The results presented in this table are derived from the article [47] and are compared to our own results, utilizing the MPSNR, MSSIM, and MRMSE metrics.

Upon analyzing the obtained results, it is evident that our proposed method, following the second strategy, yielded better image quality compared with the other super resolution methods [47][77-81] in terms of the selected criteria (MPSNR, MSSIM, and MRMSE). This comparison serves to demonstrate the reliability of the results obtained through our proposed method.

For a more comprehensive analysis of the restoration quality of these two images, Table 42 and Table 43 present a visualization of the original, degraded, and restored spectral signatures of multiple pixel coordinates from the "HARV" and "TOY" images, respectively. These tables serve as evidence for the effectiveness of the restoration quality.

HSI	Methods	MPSNR	MSSIM	MRMSE
“TOY”	SNNMF [77]	23.67	0.4883	17.66
	NSSR [78]	29.64	0.6117	8.85
	CMS [79]	29.41	0.9054	9.15
	DIP [80]	30.23	0.9069	8.39
	Yong [81]	33.55	0.6866	5.76
	Method in [47]	37.65	0.9725	3.95
	Our method	**40.01**	**0.9757**	**2.58**
“HARV”	SNNMF [77]	26.59	0.4986	12.86
	NSSR [78]	31.74	0.6481	7.07
	CMS [79]	31.13	0.9162	7.54
	DIP [80]	27.91	0.8390	12.23
	Yong [81]	37.26	0.6800	3.74
	Method in [47]	39.06	0.9863	3.26
	Our method	**49.26**	**0.9935**	**1.85**

Table 41: Comparison result for the full HSI restoration between our method and six methods from the literature based on the MPSNR, MSSIM, and MRMSE for the two images of the databases DBS4 [69] and DBS5 [71], “TOY” and “HARV”, respectively.

coordinates	Spectral signature	coordinates	Spectral signature
Pixel (0,8)	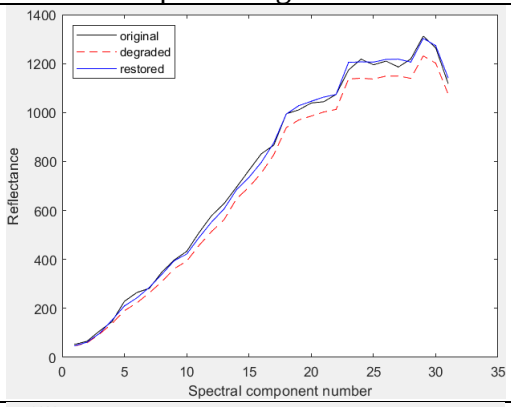	Pixel (391,325)	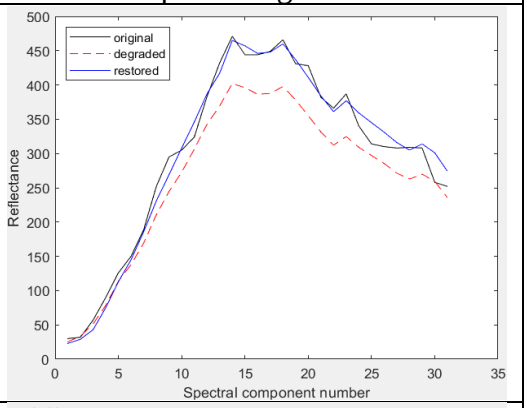
Pixel (2,25)	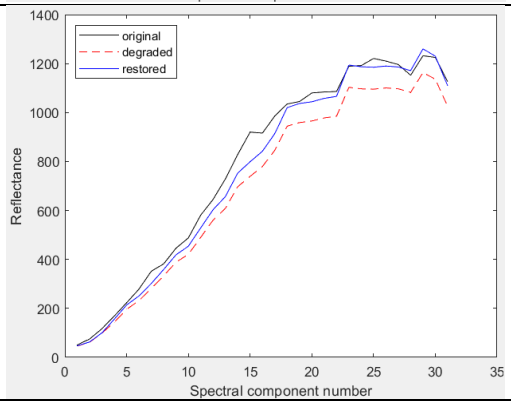	Pixel (401,106)	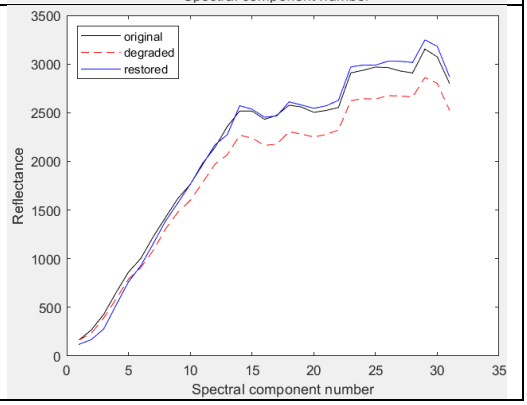

Table 42: Comparison between the original, degraded and restored spectral signature of four different pixel coordinates using a gaussian blue of support size 9×9 for the image “HARV

coordinate	Spectral signature	coordinate	Spectral signature
Pixel (205,309)	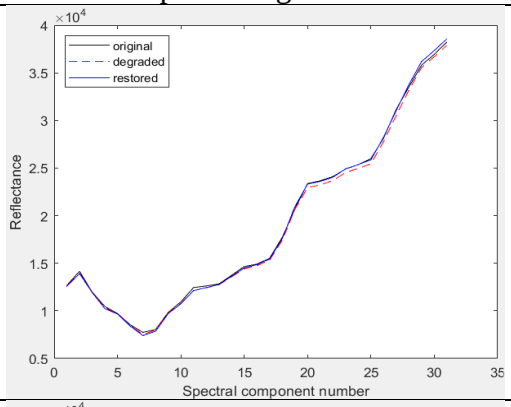	Pixel (391,340)	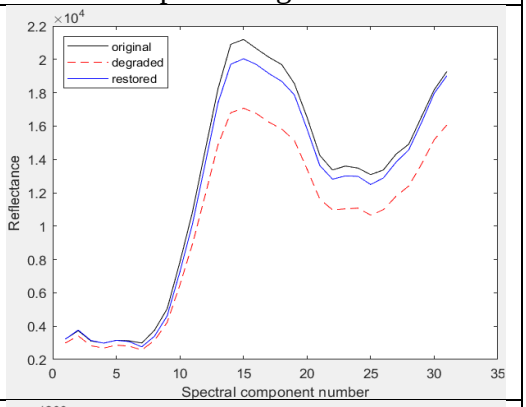
Pixel (207,297)	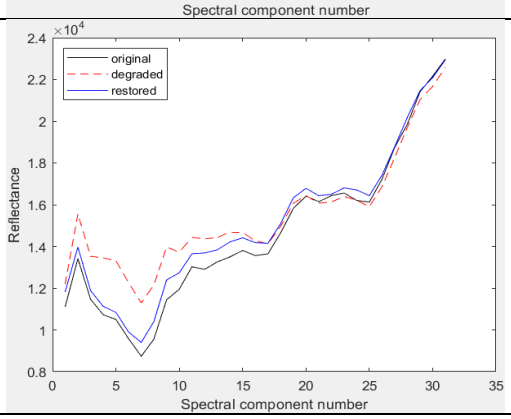	Pixel (512,494)	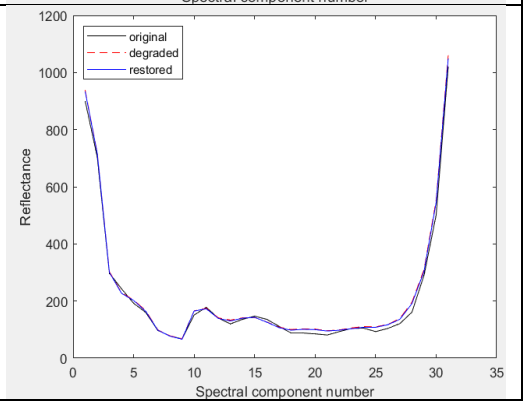

Table 43: Comparison between the original, degraded and restored spectral signature of four different pixel coordinates using a gaussian blue of support size 9×9 for the image "TOY"

5.5. Computational efficiency

All the above experiments were conducted on a laptop computer featuring an 11th Gen Intel Core i5-1135G7 processor and 16 GB of RAM. The laptop operated on Windows 10 Pro, version 22H2, providing a stable environment for the execution of the image restoration algorithms.

To quantify the computational efficiency of the proposed restoration methods, we utilized the "cpuruntime" function available in MATLAB 2020a to measure the CPU runtime. This approach allowed us to accurately capture the execution time of the restoration processes.

Table 44 presents the recorded CPU time measured in seconds for the PSF estimation using four monochrome images ("Bridge", "Photo", "Wall", and "Face") and three HSIs. We considered four different degradation functions of different support sizes ($9 \times 9, 13 \times 13, 19 \times 19$, and 23×23). Table 45 focuses on the CPU run time needed for the final image restoration of the above-mentioned images. In Table 46 a comparison between the CPU runtime of the whole restoration process using PAN's method and our blind proposed method. For this comparison we have used the four monochrome images in DBS1 [62] degraded by three different PSFs of different support size (13×13, 19×19, 23×23).

While the CPU time recorded in the presented tables may appear extensive, it is crucial to recognize that these durations reflect a balance between restoration quality and computational efficiency. Our proposed

method involves investing time to accurately estimate all the necessary regularization parameters. This parameter estimation process contributes in achieving an optimal restoration quality.

While the method might take more time for the restoration itself, this additional time is dedicated to ensuring that the restoration results are of the highest possible quality. Therefore, the trade-off between restoration quality and computation time is a strategic decision that prioritizes the final outcome. By dedicating the necessary time to parameter estimation and optimization, our method aims to deliver results that align with the desired restoration quality, even if it involves slightly longer CPU runtime.

PSF estimation CPU run time (seconds)				
PSF size	**9 × 9**	**13 × 13**	**19 × 19**	**23 × 23**
Bridge	-	6848.4	6885.5	8208.9
Photo	-	5786.3	6535.8	7765.6
Wall	-	6195.9	6820.5	9024.9
Face	-	6198.9	7130.7	8251.4
60 × 60 × 90	4478.1	5303.2	7135.1	-
TOY	78467	-	-	-
HARV	127873	-	-	-

Table 44: CPU run time for the PSF estimation

Final image restoration CPU run time (seconds)				
PSF size	**9 × 9**	**13 × 13**	**19 × 19**	**23 × 23**
Bridge	-	2237.2	2574.3	3609.5
Photo	-	2205.9	2491	3360
Wall	-	2362.1	2600	3075.3
Face	-	2386.4	2718.5	3145.7
60 × 60 × 90	47300.7	41067.2	38007.8	-
TOY	237751.1	-	-	-
HARV	259861.5	-	-	-

Table 45: CPU Time for the final image restoration

PSF size	**13 × 13**	**19 × 19**	**23 × 23**
"Bridge"			
PAN	81.33	105.84	118.58
OURS	9085.6	9459.8	11818.4
"Photo"			
PAN	78.5	106.33	118.31
OURS	7992.2	9026.8	11125.6
"Wall"			
PAN	77.78	103	115.03
OURS	8558	9420.5	12100.2
"Face"			
PAN	75.36	95.02	112.98
OURS	8585.3	9849.2	11397.1

Table 46: Comparison of the CPU runtime between the original method and our proposed blind method

6. Conclusion

In this chapter, we propose a new image restoration method with the main objective of eliminating all prior information and avoiding empirical parameter tuning. This guarantees an optimal solution while improving the restoration quality compared to existing restoration methods. The proposed hybrid method is applied to various types of images, including monochrome, RGB, and hyperspectral images.

Two strategies are suggested for restoring a hyperspectral image. The first strategy involves forming groups of highly correlated spectral components using an unsupervised partition method. For each group, one exemplar spectral component is selected to represent the group, and the PSF estimation is performed using only these exemplar components. Finally, the estimated PSF of each group is used to restore all the spectral components of it designated group.

For the second strategy we have introduced an evaluation of the estimated PSFs from each exemplar spectral component obtained in the first strategy to find the most accurate estimation. Subsequently, the most accurate estimated PSF is used to restore all the spectral components of our hyperspectral image.

Our proposed method was evaluated and validated using different images from various databases artificially degraded. We employed different degradation functions with different support sizes to degraded our reference image. To assess the results, we selected multiple evaluation metrics, including PSNR, SSIM, RMSE, and L_1 norm for error estimation. For the assessment of hyperspectral images, we also evaluated the spectral signature. The assessment results demonstrated the effectiveness of our proposed method compared to existing methods in the literature, emphasizing the significant improvement achieved by our approach.

List of Figures

List of Tables

General conclusion and prospective

In this thesis, we developed a method for blind image restoration where no prior information is required and we proposed a new approach to restore a full hyperspectral image. To better understand the importance of parameter estimation and evaluation of the influence of these regularization parameter values was conducted. This assessment was conducted on a database of monochrome images artificially degraded by three different motion blur functions.

Following this study, a multi-scale restoration method based on the principle of a hybrid method was developed. The contributions focused on several aspects. The first set of contributions involved redefining the scales and initializing the latent image at each scale, evolving parameters for selecting relevant edges to support PSF estimation. The second set of contributions focused on the blind estimation of the two regularization parameters involved to avoid having to fix them empirically. The first parameter is introduced into the cost function for PSF estimation and is estimated using the Weighted Generalized Cross Validation (WGCV) approach. The second parameter is integrated into the cost function for estimating the latent image and is also estimated. In the next step, we refine the support size of the PSF estimated before utilizing it in the image restoration process.

Two approaches were suggested and evaluated to restore a degraded hypercube. The first one uses unsupervised partitioning based on affinity propagation to form groups of highly correlated spectral components and blindly select an exemplar spectral component to represent each group. Then, only these exemplar spectral components are used to estimate the PSF for each group. These estimated PSFs are then used to restore all the spectral components of their designated group.

The second approach follows the same steps as the first one, forming groups of highly correlated spectral components with an exemplar for each group. This is followed by PSF estimation from each exemplar. Then, an evaluation of these estimated PSFs is conducted to select the most accurate PSF, using the kernel similarity criterion. After identifying the most accurate estimated PSF, it is used to restore all the spectral components of the degraded hyperspectral image.

In comparison with many recent state-of-the-art methods, our proposed method outperforms them, leading to an improvement in the quality of the PSF estimation, as well as the restored image (monochrome, RGB, and hyperspectral).

Looking ahead, we can consider a more complex observation model, involving spatial variability, and explore the robustness of the proposed method in the presence of different types of noise.

References

[1] R. Dian, S. Li, A. Guo, and L. Fang, "Deep Hyperspectral Image Sharpening," *IEEE Transactions on Neural Networks and Learning Systems*, vol. 29, no. 11, pp. 5345–5355, Nov. 2018, doi: 10.1109/TNNLS.2018.2798162.

[2] L. Zhang, W. Wei, Y. Zhang, C. Shen, A. Hengel, and Q. Shi, "Cluster Sparsity Field: An Internal Hyperspectral Imagery Prior for Reconstruction," *International Journal of Computer Vision*, vol. 126, Aug. 2018, doi: 10.1007/s11263-018-1080-8.

[3] Y. Fu, A. Lam, I. Sato, T. Okabe, and Y. Sato, "Separating Reflective and Fluorescent Components Using High Frequency Illumination in the Spectral Domain," in *2013 IEEE International Conference on Computer Vision*, Sydney, Australia: IEEE, Dec. 2013, pp. 457–464. doi: 10.1109/ICCV.2013.63.

[4] J. Liu, Z. Wu, L. Xiao, and X.-J. Wu, "Model Inspired Autoencoder for Unsupervised Hyperspectral Image Super-Resolution," *IEEE Transactions on Geoscience and Remote Sensing*, vol. 60, pp. 1–12, 2022, doi: 10.1109/TGRS.2022.3143156.

[5] Y. Zhang, B. Du, L. Zhang, and T. Liu, "Joint Sparse Representation and Multitask Learning for Hyperspectral Target Detection," *IEEE Transactions on Geoscience and Remote Sensing*, vol. 55, no. 2, pp. 894–906, Feb. 2017, doi: 10.1109/TGRS.2016.2616649.

[6] S. Li, W. Song, L. Fang, Y. Chen, P. Ghamisi, and J. A. Benediktsson, "Deep Learning for Hyperspectral Image Classification: An Overview," *IEEE Transactions on Geoscience and Remote Sensing*, vol. 57, no. 9, pp. 6690–6709, Sep. 2019, doi: 10.1109/TGRS.2019.2907932.

[7] C. Wu, B. Du, and L. Zhang, "Hyperspectral anomalous change detection based on joint sparse representation," *ISPRS Journal of Photogrammetry and Remote Sensing*, vol. 146, pp. 137–150, Dec. 2018, doi: 10.1016/j.isprsjprs.2018.09.005.

[8] Q. Wang, J. Lin, and Y. Yuan, "Salient Band Selection for Hyperspectral Image Classification via Manifold Ranking," *IEEE Transactions on Neural Networks and Learning Systems*, vol. 27, no. 6, pp. 1279–1289, Jun. 2016, doi: 10.1109/TNNLS.2015.2477537.

[9] N. Akhtar and A. Mian, "Nonparametric Coupled Bayesian Dictionary and Classifier Learning for Hyperspectral Classification," *IEEE Transactions on Neural Networks and Learning Systems*, vol. 29, no. 9, pp. 4038–4050, Sep. 2018, doi: 10.1109/TNNLS.2017.2742528.

[10] N. He, L. Fang, S. Li, J. Plaza, and A. Plaza, "Skip-Connected Covariance Network for Remote Sensing Scene Classification," *IEEE Transactions on Neural Networks and Learning Systems*, vol. 31, no. 5, pp. 1461–1474, May 2020, doi: 10.1109/TNNLS.2019.2920374.

[11] H. V. Nguyen, A. Banerjee, and R. Chellappa, "Tracking via object reflectance using a hyperspectral video camera," in *2010 IEEE Computer Society Conference on Computer Vision and Pattern Recognition - Workshops*, Jun. 2010, pp. 44–51. doi: 10.1109/CVPRW.2010.5543780.

[12] R. Larsen, A. A. Nielsen, and K. Conradsen, "Restoration of Hyperspectral Push-Broom Scanner Data".

[13] Y. Song, E.-H. Djermoune, J. Chen, C. Richard, and D. Brie, "Online deconvolution for pushbroom hyperspectral imaging systems," in *2017 IEEE 7th International Workshop on Computational Advances in Multi-Sensor Adaptive Processing (CAMSAP)*, Dec. 2017, pp. 1–5. doi: 10.1109/CAMSAP.2017.8313143.

[14] M. A. Hadj-Youcef, F. Orieux, A. Fraysse, and A. Abergel, "Restoration from multispectral blurred data with non-stationary instrument response," in *2017 25th European Signal Processing Conference (EUSIPCO)*, Aug. 2017, pp. 503–507. doi: 10.23919/EUSIPCO.2017.8081258.

[15] A. Foi, M. Trimeche, V. Katkovnik, and K. Egiazarian, "Practical Poissonian-Gaussian Noise Modeling and Fitting for Single-Image Raw-Data," *IEEE Transactions on Image Processing*, vol.

17, no. 10, pp. 1737–1754, Oct. 2008, doi: 10.1109/TIP.2008.2001399.
[16] N. Acito, M. Diani, and G. Corsini, "Signal-Dependent Noise Modeling and Model Parameter Estimation in Hyperspectral Images," *IEEE Transactions on Geoscience and Remote Sensing*, vol. 49, no. 8, pp. 2957–2971, Aug. 2011, doi: 10.1109/TGRS.2011.2110657.
[17] S. Bourennane and C. Fossati, "Rare signals detection in nonwhite noise environment based on multidimensional signal subspace for hyperspectral image," in *2016 24th European Signal Processing Conference (EUSIPCO)*, Aug. 2016, pp. 928–932. doi: 10.1109/EUSIPCO.2016.7760384.
[18] R. K. Mourya, "Université Jean Monnet, Saint-Etienne".
[19] M. L. Uss, B. Vozel, V. V. Lukin, and K. Chehdi, "Local Signal-Dependent Noise Variance Estimation From Hyperspectral Textural Images," *IEEE Journal of Selected Topics in Signal Processing*, vol. 5, no. 3, pp. 469–486, Jun. 2011, doi: 10.1109/JSTSP.2010.2104312.
[20] M. S. C. Almeida and M. Figueiredo, "Deconvolving Images With Unknown Boundaries Using the Alternating Direction Method of Multipliers," *IEEE Transactions on Image Processing*, vol. 22, no. 8, pp. 3074–3086, Aug. 2013, doi: 10.1109/TIP.2013.2258354.
[21] M. S. C. Almeida and L. B. Almeida, "Blind and Semi-Blind Deblurring of Natural Images," *IEEE Transactions on Image Processing*, vol. 19, no. 1, pp. 36–52, Jan. 2010, doi: 10.1109/TIP.2009.2031231.
[22] Z.-B. Xu, H.-L. Guo, Y. Wang, and H. Zhang, "Representative of L1/2 Regularization among Lq (0 < q ≤ 1) Regularizations: an Experimental Study Based on Phase Diagram," *Acta Automatica Sinica*, vol. 38, no. 7, pp. 1225–1228, Jul. 2012, doi: 10.1016/S1874-1029(11)60293-0.
[23] F. Sroubek and P. Milanfar, "Robust Multichannel Blind Deconvolution via Fast Alternating Minimization," *IEEE Transactions on Image Processing*, vol. 21, no. 4, pp. 1687–1700, Apr. 2012, doi: 10.1109/TIP.2011.2175740.
[24] D. Ren, K. Zhang, Q. Wang, Q. Hu, and W. Zuo, "Neural Blind Deconvolution Using Deep Priors," in *2020 IEEE/CVF Conference on Computer Vision and Pattern Recognition (CVPR)*, Seattle, WA, USA: IEEE, Jun. 2020, pp. 3338–3347. doi: 10.1109/CVPR42600.2020.00340.
[25] V. Lempitsky, A. Vedaldi, and D. Ulyanov, "Deep Image Prior," in *2018 IEEE/CVF Conference on Computer Vision and Pattern Recognition*, Jun. 2018, pp. 9446–9454. doi: 10.1109/CVPR.2018.00984.
[26] J. Pan, R. Liu, Z. Su, and X. Gu, "Kernel Estimation from Salient Structure for Robust Motion Deblurring," *Signal Processing: Image Communication*, vol. 28, no. 9, pp. 1156–1170, Oct. 2013, doi: 10.1016/j.image.2013.05.001.
[27] J. Pan, R. Liu, Z. Su, and G. Liu, "Motion blur kernel estimation via salient edges and low rank prior," in *2014 IEEE International Conference on Multimedia and Expo (ICME)*, Jul. 2014, pp. 1–6. doi: 10.1109/ICME.2014.6890182.
[28] L. I. Rudin, S. Osher, and E. Fatemi, "Nonlinear total variation based noise removal algorithms," *Physica D: Nonlinear Phenomena*, vol. 60, no. 1–4, pp. 259–268, Nov. 1992, doi: 10.1016/0167-2789(92)90242-F.
[29] S. Osher and L. I. Rudin, "Feature-Oriented Image Enhancement Using Shock Filters," *SIAM J. Numer. Anal.*, vol. 27, no. 4, pp. 919–940, Aug. 1990, doi: 10.1137/0727053.
[30] A. Levin, R. Fergus, F. Durand, and W. T. Freeman, "Image and depth from a conventional camera with a coded aperture," *ACM Trans. Graph.*, vol. 26, no. 3, p. 70, Jul. 2007, doi: 10.1145/1276377.1276464.
[31] H. Yang, X. Su, and S. Chen, "Blind Image Deconvolution Algorithm Based on Sparse Optimization with an Adaptive Blur Kernel Estimation," *Applied Sciences*, vol. 10, no. 7, p. 2437, Apr. 2020, doi: 10.3390/app10072437.

[32] W. E. Snyder and H. Qi, *Machine Vision*. Cambridge University Press, 2004.
[33] L. Zhou, T. Zhang, Y. Tian, and H. Huang, "Fraction-Order Total Variation Image Blind Restoration Based on Self-Similarity Features," *IEEE Access*, vol. 8, pp. 30436–30444, 2020, doi: 10.1109/ACCESS.2020.2972269.
[34] L. Zhou and J. Tang, "Fraction-order total variation blind image restoration based on L1-norm," *Applied Mathematical Modelling*, vol. 51, pp. 469–476, Nov. 2017, doi: 10.1016/j.apm.2017.07.009.
[35] B. B. Mandelbrot and J. W. Van Ness, "Fractional Brownian Motions, Fractional Noises and Applications," *SIAM Rev.*, vol. 10, no. 4, pp. 422–437, Oct. 1968, doi: 10.1137/1010093.
[36] X. Ge, J. Tan, and L. Zhang, "Blind Image Deblurring Using a Non-Linear Channel Prior Based on Dark and Bright Channels," *IEEE Transactions on Image Processing*, vol. 30, pp. 6970–6984, 2021, doi: 10.1109/TIP.2021.3101154.
[37] K. He, J. Sun, and X. Tang, "Single Image Haze Removal Using Dark Channel Prior," *IEEE Transactions on Pattern Analysis and Machine Intelligence*, vol. 33, no. 12, pp. 2341–2353, Dec. 2011, doi: 10.1109/TPAMI.2010.168.
[38] Y. Yan, W. Ren, Y. Guo, R. Wang, and X. Cao, "Image Deblurring via Extreme Channels Prior".
[39] J. Pan, D. Sun, H. Pfister, and M.-H. Yang, "Blind Image Deblurring Using Dark Channel Prior".
[40] L. Xu, C. Lu, Y. Xu, and J. Jia, "Image smoothing via L0 gradient minimization," in *Proceedings of the 2011 SIGGRAPH Asia Conference*, in SA '11. New York, NY, USA: Association for Computing Machinery, Dec. 2011, pp. 1–12. doi: 10.1145/2024156.2024208.
[41] D. Perrone and P. Favaro, "Total Variation Blind Deconvolution: The Devil Is in the Details," in *2014 IEEE Conference on Computer Vision and Pattern Recognition*, Columbus, OH, USA: IEEE, Jun. 2014, pp. 2909–2916. doi: 10.1109/CVPR.2014.372.
[42] L. Huang and Y. Xia, "Joint blur kernel estimation and CNN for blind image restoration," *Neurocomputing*, vol. 396, pp. 324–345, Jul. 2020, doi: 10.1016/j.neucom.2018.12.083.
[43] T. Kobayashi, "BFO Meets HOG: Feature Extraction Based on Histograms of Oriented p.d.f. Gradients for Image Classification," in *2013 IEEE Conference on Computer Vision and Pattern Recognition*, Portland, OR, USA: IEEE, Jun. 2013, pp. 747–754. doi: 10.1109/CVPR.2013.102.
[44] W. Wang, J. Li, F. Huang, and H. Feng, "Design and implementation of Log-Gabor filter in fingerprint image enhancement," *Pattern Recognition Letters*, vol. 29, no. 3, pp. 301–308, Feb. 2008, doi: 10.1016/j.patrec.2007.10.004.
[45] L. Zhang, L. Zhang, X. Mou, and D. Zhang, "FSIM: A Feature Similarity Index for Image Quality Assessment," *IEEE Transactions on Image Processing*, vol. 20, no. 8, pp. 2378–2386, Aug. 2011, doi: 10.1109/TIP.2011.2109730.
[46] D. P. Kingma and J. Ba, "Adam: A Method for Stochastic Optimization." arXiv, Jan. 29, 2017. Accessed: Aug. 25, 2023. [Online]. Available: http://arxiv.org/abs/1412.6980
[47] L. Zhang, J. Nie, W. Wei, Y. Li, and Y. Zhang, "Deep Blind Hyperspectral Image Super-Resolution," *IEEE Transactions on Neural Networks and Learning Systems*, vol. 32, no. 6, pp. 2388–2400, Jun. 2021, doi: 10.1109/TNNLS.2020.3005234.
[48] M. Zhang, B. Vozel, K. Chehdi, M. Uss, S. Abramov, and V. Lukin, "Accuracy assessment of blind and semi-blind restoration methods for hyperspectral images," presented at the SPIE Remote Sensing, L. Bruzzone and F. Bovolo, Eds., Edinburgh, United Kingdom, Oct. 2016, p. 100040P. doi: 10.1117/12.2240950.
[49] M. Zhang, "Vers une méthode de restauration aveugle d'images hyperspectrales," These de doctorat, Rennes 1, 2018. Accessed: Aug. 25, 2023. [Online]. Available: https://www.theses.fr/2018REN1S132
[50] D. Krishnan, T. Tay, and R. Fergus, "Blind deconvolution using a normalized sparsity measure," in *CVPR 2011*, Jun. 2011, pp. 233–240. doi: 10.1109/CVPR.2011.5995521.

[51] C. Charrier, C. Larabi, and H. Saadane, “Evaluation de la qualité des images”.
[52] A. Horé and D. Ziou, “Image Quality Metrics: PSNR vs. SSIM,” in *2010 20th International Conference on Pattern Recognition*, Aug. 2010, pp. 2366–2369. doi: 10.1109/ICPR.2010.579.
[53] Z. Wang, A. C. Bovik, H. R. Sheikh, and E. P. Simoncelli, “Image quality assessment: from error visibility to structural similarity,” *IEEE Transactions on Image Processing*, vol. 13, no. 4, pp. 600–612, Apr. 2004, doi: 10.1109/TIP.2003.819861.
[54] W. Xue, L. Zhang, X. Mou, and A. C. Bovik, “Gradient Magnitude Similarity Deviation: A Highly Efficient Perceptual Image Quality Index,” *IEEE Transactions on Image Processing*, vol. 23, no. 2, pp. 684–695, Feb. 2014, doi: 10.1109/TIP.2013.2293423.
[55] A. Levin, Y. Weiss, F. Durand, and W. T. Freeman, “Efficient marginal likelihood optimization in blind deconvolution,” in *CVPR 2011*, Jun. 2011, pp. 2657–2664. doi: 10.1109/CVPR.2011.5995308.
[56] X. Tao, H. Gao, X. Shen, J. Wang, and J. Jia, “Scale-Recurrent Network for Deep Image Deblurring”.
[57] J. Pan, D. Sun, H. Pfister, and M.-H. Yang, “Deblurring Images via Dark Channel Prior,” *IEEE Transactions on Pattern Analysis and Machine Intelligence*, vol. 40, no. 10, pp. 2315–2328, Oct. 2018, doi: 10.1109/TPAMI.2017.2753804.
[58] W. Zuo, D. Ren, D. Zhang, S. Gu, and L. Zhang, “Learning Iteration-wise Generalized Shrinkage–Thresholding Operators for Blind Deconvolution,” *IEEE Transactions on Image Processing*, vol. 25, no. 4, pp. 1751–1764, Apr. 2016, doi: 10.1109/TIP.2016.2531905.
[59] Z. Hu and M.-H. Yang, “Good Regions to Deblur,” in *Computer Vision – ECCV 2012*, A. Fitzgibbon, S. Lazebnik, P. Perona, Y. Sato, and C. Schmid, Eds., in Lecture Notes in Computer Science, vol. 7576. Berlin, Heidelberg: Springer Berlin Heidelberg, 2012, pp. 59–72. doi: 10.1007/978-3-642-33715-4_5.
[60] L. Sun, S. Cho, J. Wang, and J. Hays, “Edge-based blur kernel estimation using patch priors,” in *IEEE International Conference on Computational Photography (ICCP)*, Apr. 2013, pp. 1–8. doi: 10.1109/ICCPhot.2013.6528301.
[61] M. S. C. Almeida and M. A. T. Figueiredo, “Parameter Estimation for Blind and Non-Blind Deblurring Using Residual Whiteness Measures,” *IEEE Transactions on Image Processing*, vol. 22, no. 7, pp. 2751–2763, Jul. 2013, doi: 10.1109/TIP.2013.2257810.
[62] A. Levin, Y. Weiss, F. Durand, and W. T. Freeman, “Understanding and evaluating blind deconvolution algorithms,” in *2009 IEEE Conference on Computer Vision and Pattern Recognition*, Jun. 2009, pp. 1964–1971. doi: 10.1109/CVPR.2009.5206815.
[63] J. Chung, J. G. Nagy, and D. P. O’Leary, “A weighted GCV method for Lanczos hybrid regularization,” *in Electronic Transactions on Numerical Analysis*, 2008, 28(149-167).
[64] R. M. Larsen, “Lanczos Bidiagonalization With Partial Reorthogonalization,” *DAIMI Report Series*, no. 537, Art. no. 537, Dec. 1998, doi: 10.7146/dpb.v27i537.7070.
[65] Y. Dong, M. Hintermüller, and M. M. Rincon-Camacho, “Automated Regularization Parameter Selection in Multi-Scale Total Variation Models for Image Restoration,” *J Math Imaging Vis*, vol. 40, no. 1, pp. 82–104, May 2011, doi: 10.1007/s10851-010-0248-9.
[66] M. Hintermüller and M. M. Rincon-Camacho, “Expected absolute value estimators for a spatially adapted regularization parameter choice rule in L1-TV-based image restoration,” *Inverse Problems*, vol. 26, no. 8, p. 085005, Jun. 2010, doi: 10.1088/0266-5611/26/8/085005.
[67] “Laboratory for Image and Video Engineering - The University of Texas at Austin.” https://live.ece.utexas.edu/research/quality/subjective.htm
[68] “True Color Kodak Images.” https://r0k.us/graphics/kodak/
[69] “CAVE | Projects: Multispectral Image Database.” https://www.cs.columbia.edu/CAVE/databases/multispectral/
[70] F. Yasuma, T. Mitsunaga, D. Iso, and S. K. Nayar, “Generalized Assorted Pixel Camera: Postcapture

Control of Resolution, Dynamic Range, and Spectrum," *IEEE Transactions on Image Processing*, vol. 19, no. 9, pp. 2241–2253, Sep. 2010, doi: 10.1109/TIP.2010.2046811.
[71] "Statistics of Real-World Hyperspectral Images." https://vision.seas.harvard.edu/hyperspec/download.html
[72] K. Zhang, D. Tao, X. Gao, X. Li, and J. Li, "Coarse-to-Fine Learning for Single-Image Super-Resolution," *IEEE Transactions on Neural Networks and Learning Systems*, vol. 28, no. 5, pp. 1109–1122, May 2017, doi: 10.1109/TNNLS.2015.2511069.
[73] L. Zhou and J. Tang, "Fraction-order total variation blind image restoration based on L1-norm," *Applied Mathematical Modelling*, vol. 51, pp. 469–476, Nov. 2017, doi: 10.1016/j.apm.2017.07.009.
[74] L. Zhong, S. Cho, D. Metaxas, S. Paris, and J. Wang, "Handling Noise in Single Image Deblurring Using Directional Filters," in *2013 IEEE Conference on Computer Vision and Pattern Recognition*, Portland, OR, USA: IEEE, Jun. 2013, pp. 612–619. doi: 10.1109/CVPR.2013.85.
[75] Y. Elmi Sola, F. Zargari, and A. M. Rahmani, "Blind image deblurring based on multi-resolution ringing removal," *Signal Processing*, vol. 154, pp. 250–259, Jan. 2019, doi: 10.1016/j.sigpro.2018.09.015.
[76] J. Alameddine, K. Chehdi, and C. Cariou, "Hierarchical Unsupervised Partitioning of Large Size Data and Its Application to Hyperspectral Images," *Remote Sensing*, vol. 13, no. 23, p. 4874, Nov. 2021, doi: 10.3390/rs13234874.
[77] E. Wycoff, T.-H. Chan, K. Jia, W.-K. Ma, and Y. Ma, "A non-negative sparse promoting algorithm for high resolution hyperspectral imaging," in *2013 IEEE International Conference on Acoustics, Speech and Signal Processing*, May 2013, pp. 1409–1413. doi: 10.1109/ICASSP.2013.6637883.
[78] W. Dong *et al.*, "Hyperspectral Image Super-Resolution via Non-Negative Structured Sparse Representation," *IEEE Transactions on Image Processing*, vol. 25, no. 5, pp. 2337–2352, May 2016, doi: 10.1109/TIP.2016.2542360.
[79] L. Zhang, W. Wei, C. Bai, Y. Gao, and Y. Zhang, "Exploiting Clustering Manifold Structure for Hyperspectral Imagery Super-Resolution," *IEEE Transactions on Image Processing*, vol. 27, no. 12, pp. 5969–5982, Dec. 2018, doi: 10.1109/TIP.2018.2862629.
[80] V. Lempitsky, A. Vedaldi, and D. Ulyanov, "Deep Image Prior," in *2018 IEEE/CVF Conference on Computer Vision and Pattern Recognition*, Jun. 2018, pp. 9446–9454. doi: 10.1109/CVPR.2018.00984.
[81] Y. Li, L. Zhang, C. Tian, C. Ding, Y. Zhang, and W. Wei, "Hyperspectral image super-resolution extending: An effective fusion based method without knowing the spatial transformation matrix," in *2017 IEEE International Conference on Multimedia and Expo (ICME)*, Jul. 2017, pp. 1117–1122. doi: 10.1109/ICME.2017.8019510.

APPENDIX

1. Evaluating the empirical choice of the regularization parameters fixed by PAN

a) Evaluation using PSF of support size 13×13

Test	PSNR	SNR	$E(L_1)$ norm	MSE	$\boldsymbol{\alpha}$	$\boldsymbol{\beta_{lat}}$	$\boldsymbol{\beta}$
			« Bridge »				
Test 1 -PAN	19.2438	11.0613	0.0594	0.0085	0.01	0.005	0.003
Test 2	19.5721	10.7201	0.0677	0.0078	1	1	1
Test 3	**21.7414**	**13.4455**	**0.0478**	**0.0048**	**0.001**	**0.05**	**0.03**
Test 4	19.7669	11.0048	0.0655	0.0075	0.5	0.01	0.7
Test 5	20.2814	11.5949	0.0615	0.0067	0.5	0.5	0.5
Test 6	20.8642	12.3153	0.0563	0.0058	0.058	0.4	0.25
Test 7	21.2287	12.7262	0.0534	0.0054	0.75	0.3333	0.1429
Test 8	21.5111	13.1235	0.0503	0.0050	0.04	0.2	0.072
Test 9	20.2453	11.5718	0.0610	0.0067	0.9	0.001	0.4
Test 10	18.9111	10.7625	0.0612	0.0090	0.05	0.004	0.002
			« Photo »				
Test 1 -PAN	29.2214	21.4220	0.0174	0.001	0.01	0.005	0.003
Test 2	21.9594	13.6235	0.0500	0.0050	1	1	1
Test 3	27.7456	19.8834	0.0220	0.0013	0.001	0.05	0.03
Test 4	22.7683	14.5357	0.0440	0.0042	0.5	0.01	0.7
Test 5	23.8351	15.6728	0.0384	0.0032	0.5	0.5	0.5
Test 6	25.1503	17.1138	0.0313	0.0024	0.058	0.4	0.25
Test 7	26.3759	18.3707	0.0269	0.0018	0.75	0.3333	0.1429
Test 8	27.2160	19.2997	0.0237	0.0015	0.04	0.2	0.072
Test 9	24.5295	16.3878	0.0356	0.0028	0.9	0.001	0.4
Test 10	**29.2307**	**21.4301**	**0.0173**	**0.0009**	**0.05**	**0.004**	**0.002**

Table A1: Results of the evaluation criteria chosen for ten different combinations of the regularization parameters for PSF support size 13×13 using PAN's algorithm

b) Evaluation using PSF of support size 19×19

Test	PSNR	SNR	$E(L_1)$ norm	L_1 norm	MSE	SSIM	$\boldsymbol{\alpha}$	$\boldsymbol{\beta_{lat}}$	$\boldsymbol{\beta}$
« Bridge »									
Test 1 -PAN	**21.0529**	**12.8807**	**0.0498**	**3238.25**	**0.0056**	**0.8257**	**0.01**	**0.005**	**0.003**
Test 2	18.2024	9.2974	0.0777	5052.44	0.0108	0.4721	1	1	1
Test 3	20.1557	11.7738	0.0574	3732.44	0.0069	0.6840	0.001	0.05	0.03
Test 4	19.1362	10.2831	0.0696	4525.74	0.0087	0.5190	0.5	0.01	0.7
Test 5	19.4087	10.6460	0.0674	4382.69	0.0081	0.5396	0.5	0.5	0.5
Test 6	19.9156	11.2844	0.0624	4057.56	0.0072	0.5864	0.058	0.4	0.25
Test 7	20.3016	11.6902	0.0593	3855.98	0.0066	0.6212	0.75	0.3333	0.1429
Test 8	20.2234	11.7327	0.0583	3790.96	0.0068	0.6482	0.04	0.2	0.072
Test 9	19.5663	10.7821	0.0659	4285.15	0.0079	0.5541	0.9	0.001	0.4

Test 10	20.7864	12.6474	0.0508	3303.27	0.0059	0.8193	0.05	0.004	0.002
« Photo »									
Test 1- PAN	27.5756	19.7405	0.0216	1404.54	0.0014	0.8945	0.01	0.005	0.003
Test 2	19.1974	10.7597	0.0660	4291.65	0.0094	0.5783	1	1	1
Test 3	26.1470	18.2515	0.0277	1801.19	0.0019	0.8148	0.001	0.05	0.03
Test 4	21.6094	13.2919	0.0515	3348.79	0.0054	0.6536	0.5	0.01	0.7
Test 5	20.5552	12.2997	0.0543	3530.86	0.0069	0.6362	0.5	0.5	0.5
Test 6	22.0782	13.9610	0.0445	2893.61	0.0049	0.6918	0.058	0.4	0.25
Test 7	21.6541	13.5588	0.0447	2906.62	0.0054	0.6955	0.75	0.3333	0.1429
Test 8	23.6497	15.6599	0.0357	2321.39	0.0034	0.7539	0.04	0.2	0.072
Test 9	22.3023	14.0487	0.0466	3030.17	0.0046	0.6868	0.9	0.001	0.4
Test 10	**27.6787**	**19.9342**	**0.0205**	**1333.01**	**0.0013**	**0.9012**	**0.05**	**0.004**	**0.002**

Table A2: Results of the evaluation criteria chosen for ten different combinations of the regularization parameters for PSF support size 19×19 using PAN's algorithm

Original image	Restored image		
	Test 2	Test 1 – PAN	Test 10
	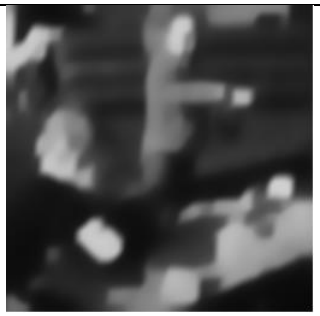		

Table A3: Visual comparison between the original image "Photo" and the restored images the restoration was performed using specific regularization parameters set for Test 1 – PAN, and Test 10 for the "Photo" image degraded by the PSF od support size 19×19.

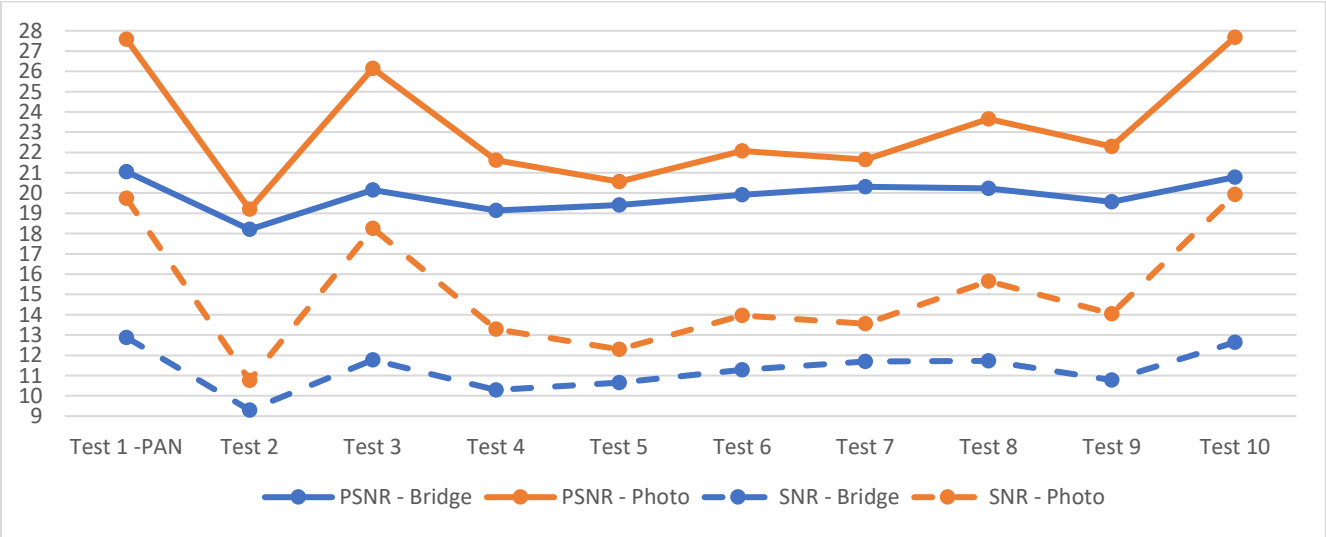

Figure A1: PSNR and SNR variation using ten different regularization parameters combinations for the "Bridge" and "Photo" images, with PSF support size 19×19

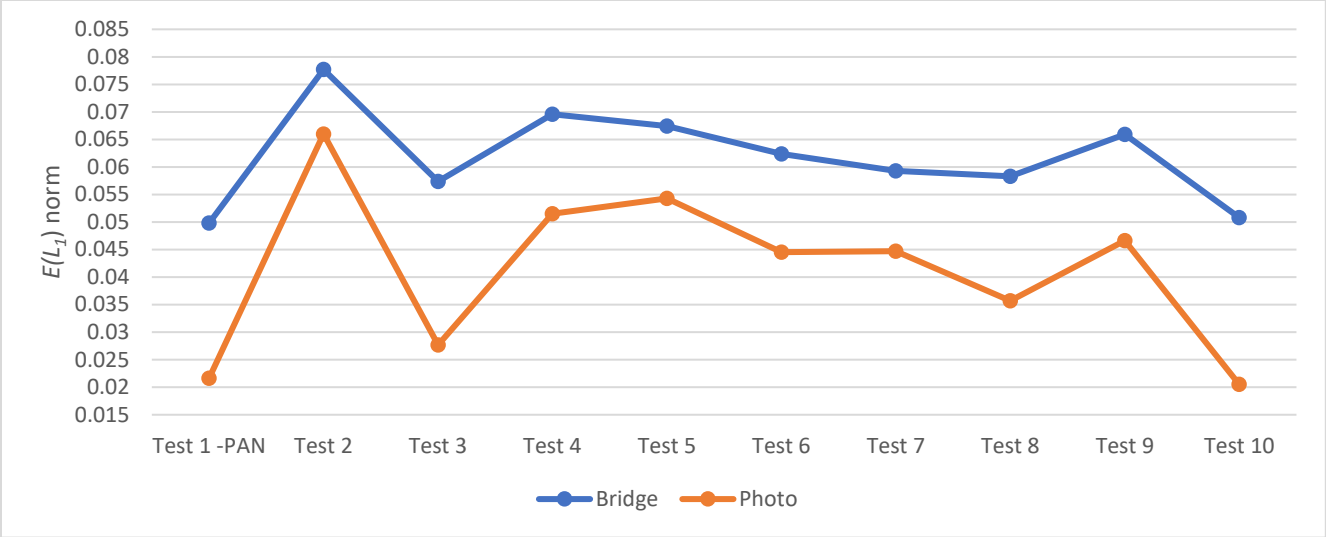

Figure A2: $E(L_1)$ norm variation using ten different regularization parameters combinations for the "Bridge" and "Photo" images, with PSF support size 19×19

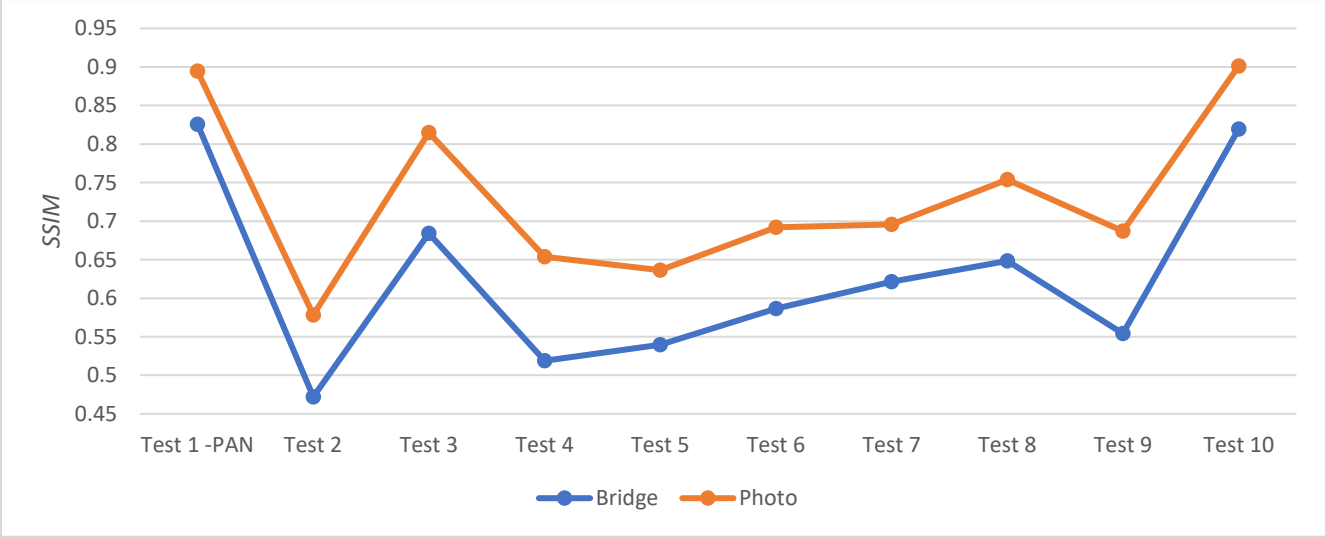

Figure A3: SSIM variation using ten different regularization parameters combinations for the "Bridge" and "Photo" images, with PSF support size 19×19

c) Evaluation using PSF of support size 23×23

Test	PSNR	SNR	$E(L_1)$ norm	L_1 norm	MSE	SSIM	α	β_{lat}	β
« Bridge »									
Test 1 -PAN	13.8763	5.7559	0.1085	7055.21	0.0291	0.3210	0.01	0.005	0.003
Test 2	15.6256	6.5417	0.1022	6645.56	0.0195	0.3593	1	1	1
Test 3	14.8350	6.4875	0.0965	6274.91	0.0234	0.3842	0.001	0.05	0.03
Test 4	17.4117	8.3621	0.0830	5397.08	0.0128	0.4335	0.5	0.01	0.7
Test 5	15.7526	6.8051	0.0991	6443.98	0.0189	0.3648	0.5	0.5	0.5
Test 6	16.1439	7.4654	0.0900	5852.25	0.0173	0.4057	0.058	0.4	0.25
Test 7	15.2437	6.4076	0.1031	6704.08	0.0213	0.3371	0.75	0.3333	0.1429

Test 8	15.6157	7.1232	0.0919	5975.80	0.0195	0.4011	0.04	0.2	0.072
Test 9	**17.4464**	**8.3865**	**0.0895**	**5819.74**	**0.0129**	**0.4388**	**0.9**	**0.001**	**0.4**
Test 10	15.0310	6.6404	0.0980	6372.45	0.0221	0.2776	0.05	0.004	0.002
« Photo »									
Test 1 -PAN	17.8423	10.0405	0.0636	4135.59	0.0129	0.5576	0.01	0.005	0.003
Test 2	17.7895	9.2318	0.0795	5169.49	0.0131	0.5220	1	1	1
Test 3	19.1347	11.2122	0.0558	3628.40	0.0096	0.5289	0.001	0.05	0.03
Test 4	18.8341	10.2785	0.0712	4629.78	0.0103	0.5477	0.5	0.01	0.7
Test 5	20.2605	11.8995	0.0596	3875.49	0.0074	0.6099	0.5	0.5	0.5
Test 6	**20.4484**	**12.2344**	**0.0548**	**3563.37**	**0.0071**	**0.6331**	**0.058**	**0.4**	**0.25**
Test 7	20.0566	11.8307	0.0604	3927.51	0.0076	0.6057	0.75	0.3333	0.1429
Test 8	20.1982	12.1446	0.0513	3335.78	0.0075	0.6571	0.04	0.2	0.072
Test 9	18.8140	10.2863	0.0704	4577.76	0.0103	0.5437	0.9	0.001	0.4
Test 10	17.9404	10.0881	0.0632	4109.58	0.0126	0.5409	0.05	0.004	0.002

Table A4: Results of the evaluation criteria chosen for ten different combinations of the regularization parameters for PSF support size 23×23 using PAN's algorithm

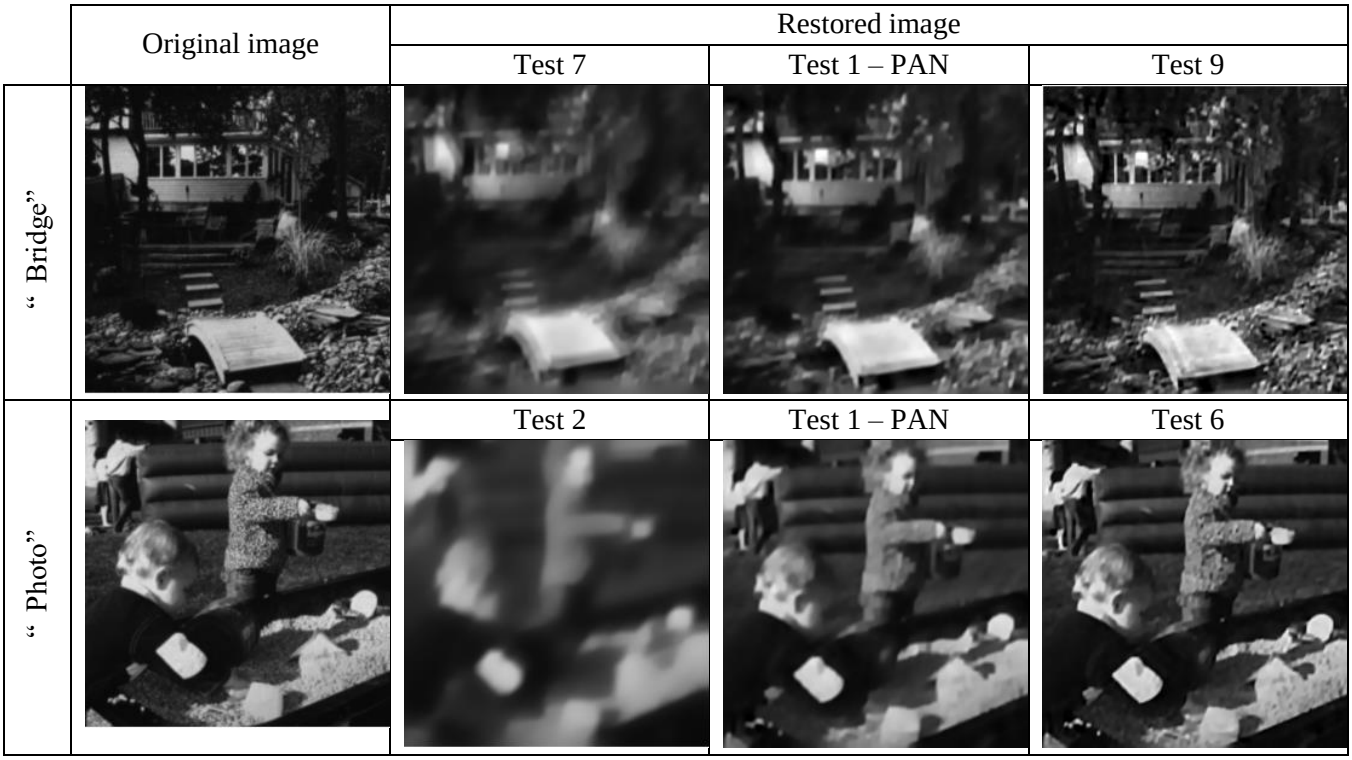

Table A5: visual comparison between the original images (“Bridge” and “Photo”) and the restored images the restoration was performed using specific regularization parameters set for Test 1 – PAN, Test 9 form the “Bridge” image and Test 6 for the “Photo” image degraded by the PSF od support size 23×23.

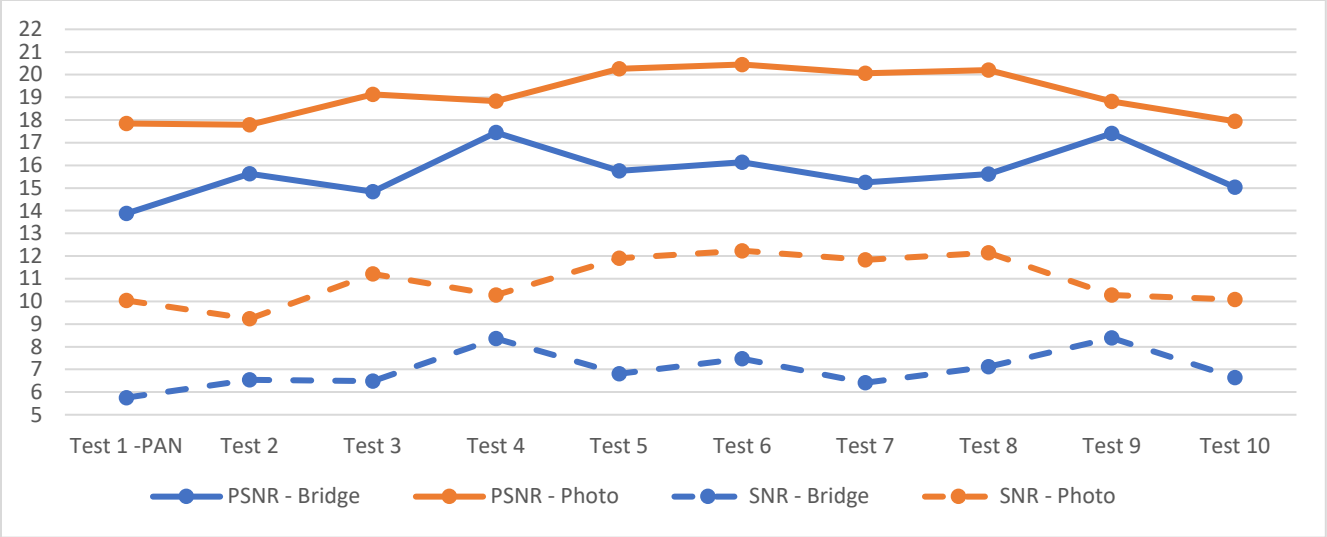

Figure A4: PSNR and SNR variation using ten different regularization parameters combinations for the "Bridge" and "Photo" images, with PSF support size 23×23

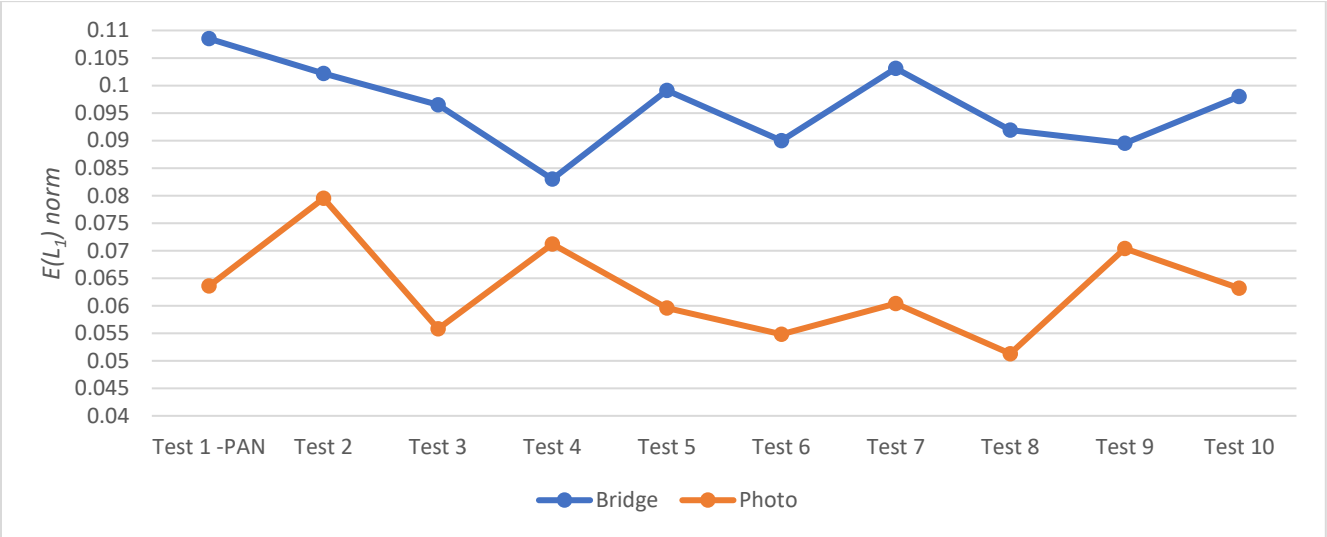

Figure A5: E(L_1) norm variation using ten different regularization parameters combinations for the "Bridge" and "Photo" images, with PSF support size 23×23

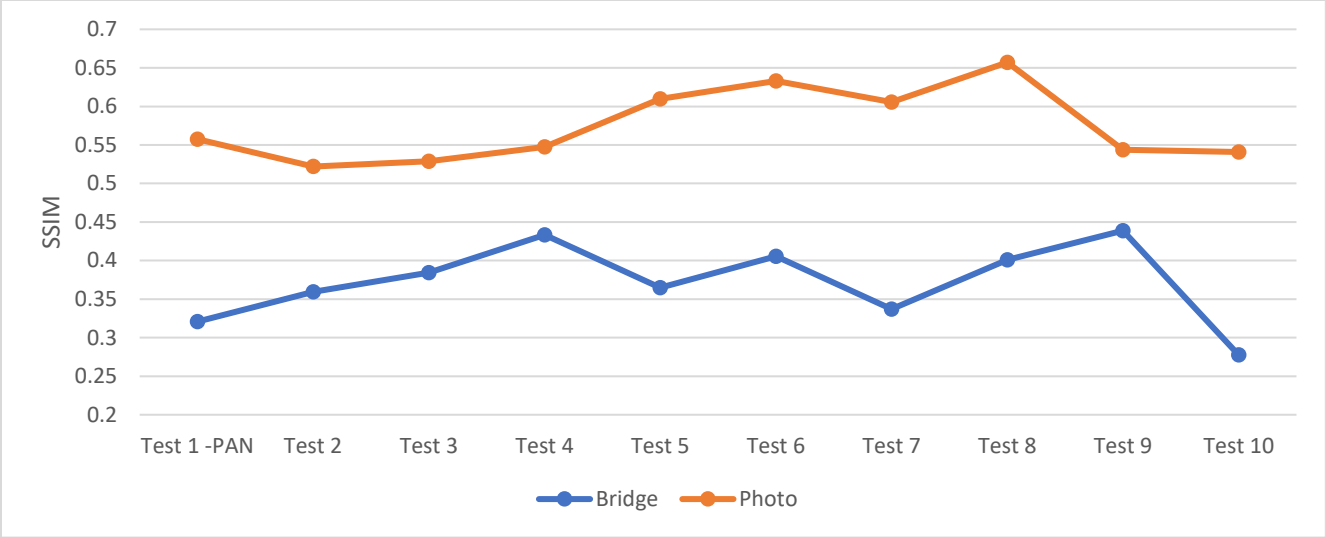

Figure A6: SSIM variation using ten different regularization parameters combinations for the "Bridge" and "Photo" images, with PSF support size 23×23

2. Evaluating the influence of each regularization parameter over the image restoration quality

i) Evaluation using PSF of support size 13x13

a) Evaluating the influence of the regularization parameter α over the restoration quality by fixing β_{lat} and β

Test	PSNR	SNR	$E(L_1)$ norm	L_1 norm	MSE	SSIM	α
« Bridge »							
Test 1	21.7414	13.4455	0.0478	3108.20	0.0048	**0.8058**	0.001
Test 2	21.7084	13.4023	0.0481	3127.70	0.0048	0.8027	0.05
Test 3	21.7380	13.4243	0.0481	3127.70	0.0048	0.8024	0.1
Test 4	**21.8156**	**13.4952**	**0.0478**	**3108.20**	**0.0047**	0.8054	**0.15**
Test 5	21.7524	13.4235	0.0481	3127.70	0.0047	0.8001	0.2
Test 6	21.7639	13.4285	0.0482	3134.21	0.0047	0.7999	0.25
Test 7	21.7701	13.4270	0.0482	3134.21	0.0047	0.7975	0.3
Test 8	21.7345	13.3843	0.0484	3147.21	0.0048	0.7944	0.35
Test 9	21.7333	13.3778	0.0485	3153.71	0.0048	0.7931	0.4
Test 10	21.6658	13.3023	0.0488	3173.22	0.0048	0.7885	0.45
Test 11	21.6886	13.3167	0.0488	3173.22	0.0048	0.7875	0.5
Test 12	21.6802	13.3027	0.0489	3179.72	0.0048	0.7857	0.55
Test 13	21.6614	13.2781	0.0490	3186.23	0.0048	0.7833	0.6
Test 14	21.6442	13.2555	0.0492	3199.23	0.0049	0.7811	0.65
Test 15	21.6147	13.2214	0.0494	3212.24	0.0049	0.7785	0.7
Test 16	21.5929	13.1958	0.0495	3218.74	0.0049	0.7763	0.75
Test 17	21.5896	13.1886	0.0496	3225.24	0.0049	0.7752	0.8
Test 18	21.5846	13.1788	0.0496	3225.24	0.0049	0.7735	0.85
Test 19	21.5614	13.1525	0.0498	3238.25	0.0050	0.7716	0.9

Test 20	21.5270	13.1150	0.0499	3244.75	0.0050	0.7691	0.95
Test 21	21.4982	13.0833	0.0501	3257.75	0.0050	0.7670	0.99
« Photo »							
Test 1	28.5341	20.7552	0.0183	1189.96	0.0011	0.9345	0.001
Test 2	29.2307	21.4301	0.0171	1111.93	0.00092	0.9396	0.05
Test 3	29.4675	21.6550	0.0167	1085.92	0.00088	0.9405	0.1
Test 4	29.5712	21.7528	0.0165	1072.91	0.00086	0.9408	0.15
Test 5	29.6848	21.8599	0.0163	1059.91	0.00084	0.9409	0.2
Test 6	**29.8364**	**22.0043**	**0.0162**	**1053.41**	**0.00081**	**0.9414**	**0.25**
Test 7	29.7366	21.8999	0.0163	1059.91	0.00083	0.9397	0.3
Test 8	29.7608	21.9205	0.0163	1059.91	0.00083	0.9392	0.35
Test 9	29.3851	21.5416	0.0169	1098.92	0.00091	0.9351	0.4
Test 10	29.2849	21.4374	0.0170	1105.43	0.00093	0.9332	0.45
Test 11	28.8492	20.9979	0.0178	1157.45	0.0010	0.9277	0.5
Test 12	29.1966	21.3396	0.0173	1124.93	0.00094	0.9307	0.55
Test 13	28.4288	20.5670	0.0187	1215.97	0.0011	0.9207	0.6
Test 14	28.1452	20.2788	0.0193	1254.98	0.0012	0.9161	0.65
Test 15	27.6146	19.7443	0.0204	1326.51	0.0014	0.9074	0.7
Test 16	28.2323	20.3592	0.0192	1248.48	0.0012	0.9156	0.75
Test 17	27.6872	19.8097	0.0203	1320.01	0.0013	0.9066	0.8
Test 18	26.3676	18.4837	0.0234	1521.59	0.0018	0.8817	0.85
Test 19	27.0311	19.1440	0.0219	1424.05	0.0016	0.8933	0.9
Test 20	27.0885	19.1985	0.0218	1417.55	0.0015	0.8935	0.95
Test 21	25.6885	17.7921	0.0253	1645.13	0.0021	0.8629	0.99

Table A6: The effect of the regularization parameter α using the PSF of support size 13×13, where β_{lat}=0.05 and β=0.03 are fixed for the image "Bridge" and for the "photo" image $\beta_{lat} = 0.004$ and $\beta = 0.002$, while α increase by a step size of 0.05

b) Evaluating the influence of the regularization parameter β_{lat} over the restoration quality by fixing α and β

Test	PSNR	SNR	$E(L_1)$ norm	L_1 norm	MSE	SSIM	$\boldsymbol{\beta_{lat}}$
« Bridge »							
Test 1	19.9227	11.5718	0.0573	3725.93	0.0072	0.7050	0.001
Test 2	21.8156	13.4952	0.0478	3108.20	0.0047	0.8054	0.05
Test 3	21.6103	13.2819	0.0487	3166.72	0.0049	0.7936	0.1
Test 4	21.5610	13.2363	0.0489	3179.72	0.0050	0.7906	0.15
Test 5	21.8348	13.5091	0.0477	3101.69	0.0047	0.8019	0.2
Test 6	21.7390	13.4130	0.0482	3134.21	0.0048	0.7972	0.25
Test 7	21.8421	13.5116	0.0478	3108.20	0.0047	0.8004	0.3
Test 8	**22.1019**	**13.7664**	**0.0467**	**3036.67**	**0.0044**	**0.8099**	**0.35**
Test 9	21.9780	13.6424	0.0472	3069.18	0.0045	0.8048	0.4
Test 10	21.8562	13.5198	0.0478	3108.20	0.0046	0.7991	0.45
Test 11	21.8974	13.5598	0.0477	3101.69	0.0046	0.8007	0.5
Test 12	21.8814	13.5459	0.0477	3101.69	0.0046	0.7999	0.55
Test 13	21.8835	13.5476	0.0477	3101.69	0.0046	0.7999	0.6
Test 14	21.8245	13.4888	0.0480	3121.20	0.0047	0.7971	0.65

Test 15	21.8495	13.5157	0.0479	3114.70	0.0046	0.7985	0.7
Test 16	21.7841	13.4557	0.0481	3127.70	0.0047	0.7962	0.75
Test 17	21.7690	13.4379	0.0483	3140.71	0.0047	0.7949	0.8
Test 18	21.7969	13.4668	0.0481	3127.70	0.0047	0.7959	0.85
Test 19	21.7722	13.4426	0.0483	3140.71	0.0047	0.7947	0.9
Test 20	21.8334	13.5067	0.0480	3121.20	0.0047	0.7978	0.95
Test 21	21.8411	13.5169	0.0479	3114.70	0.0047	0.7985	0.99
« Photo »							
Test 1	**30.9476**	**23.1062**	**0.0145**	**942.86**	**0.00063**	**0.9492**	**0.001**
Test 2	27.7687	19.9607	0.0202	1313.51	0.0013	0.9192	0.05
Test 3	26.8577	19.0584	0.0223	1450.06	0.0016	0.9057	0.1
Test 4	27.4806	19.6854	0.0209	1359.02	0.0014	0.9148	0.15
Test 5	27.7592	19.9674	0.0204	1326.51	0.0013	0.9187	0.2
Test 6	27.6442	19.8548	0.0207	1346.02	0.0014	0.9174	0.25
Test 7	27.5714	19.7851	0.0209	1359.02	0.0014	0.9168	0.3
Test 8	27.6590	19.8754	0.0208	1352.52	0.0013	0.9180	0.35
Test 9	27.0752	19.2952	0.0221	1437.05	0.0015	0.9096	0.4
Test 10	27.1817	19.4058	0.0219	1424.05	0.0015	0.9111	0.45
Test 11	26.6772	18.9034	0.0232	1508.58	0.0017	0.9035	0.5
Test 12	26.9579	19.1845	0.0225	1463.06	0.0016	0.9074	0.55
Test 13	26.5446	18.7710	0.0235	1528.09	0.0017	0.9012	0.6
Test 14	26.4402	18.6690	0.0238	1547.60	0.0018	0.8994	0.65
Test 15	26.3364	18.5667	0.0241	1567.10	0.0018	0.8974	0.7
Test 16	26.2054	18.4386	0.0245	1593.11	0.0019	0.8951	0.75
Test 17	26.1334	18.3684	0.0247	1606.12	0.0019	0.8937	0.8
Test 18	25.8860	18.1235	0.0254	1651.64	0.0020	0.8898	0.85
Test 19	25.7483	17.9896	0.0258	1677.65	0.0021	0.8877	0.9
Test 20	25.8113	18.0548	0.0256	1664.64	0.0021	0.8891	0.95
Test 21	25.8376	18.0822	0.0255	1658.14	0.0020	0.8895	0.99

Table A7: The effect of the regularization parameter β_{lat} using the PSF of support size 13×13, where α=0.15 and β=0.03 are fixed for the image "Bridge" and for the "photo" image $\alpha = 0.25$ and $\beta = 0.002$, while β_{lat} increase by a step size of 0.05

c) Evaluating the influence of the regularization parameter β over the restoration quality by fixing β_{lat} and α

Test	PSNR	SNR	$E(L_1)$ norm	L_1 norm	MSE	SSIM	$\boldsymbol{\beta}$
« Bridge »							
Test 1	20.6751	12.5813	0.0517	3361.79	0.0061	0.8215	0.001
Test 2	**21.9367**	**13.5627**	**0.0481**	**3127.70**	**0.0046**	**0.8267**	**0.05**
Test 3	21.5965	13.1590	0.0507	3296.77	0.0049	0.7371	0.1
Test 4	21.3399	12.8563	0.0528	3433.32	0.0052	0.7074	0.15
Test 5	21.1293	12.6079	0.0544	3537.36	0.0055	0.6848	0.2
Test 6	20.9493	12.3951	0.0559	3634.90	0.0057	0.6663	0.25
Test 7	20.7912	12.2078	0.0572	3719.43	0.0059	0.6507	0.3
Test 8	20.6503	12.0405	0.0584	3797.46	0.0061	0.6370	0.35

Test 9	20.5235	11.8891	0.0595	3868.99	0.0063	0.6250	0.4
Test 10	20.4083	11.7511	0.0605	3934.01	0.0065	0.6142	0.45
Test 11	20.3028	11.6243	0.0614	3992.54	0.0066	0.6046	0.5
Test 12	20.2057	11.5071	0.0622	4044.56	0.0068	0.5958	0.55
Test 13	20.1158	11.3981	0.0630	4096.58	0.0069	0.5877	0.6
Test 14	20.0322	11.2962	0.0637	4142.09	0.0071	0.5803	0.65
Test 15	19.9539	11.2006	0.0644	4187.61	0.0072	0.5734	0.7
Test 16	19.8805	11.1105	0.0650	4226.63	0.0073	0.5671	0.75
Test 17	19.8114	11.0252	0.0656	4265.64	0.0074	0.5611	0.8
Test 18	19.7459	10.9442	0.0662	4304.66	0.0075	0.5555	0.85
Test 19	19.6839	10.8671	0.0667	4337.17	0.0076	0.5503	0.9
Test 20	19.6248	10.7933	0.0672	4369.68	0.0078	0.5454	0.95
Test 21	19.5795	10.7366	0.0677	4402.19	0.0078	0.5416	0.99
« Photo »							
Test 1	**30.3552**	**22.5296**	**0.0151**	**981.88**	**0.00072**	**0.9504**	**0.001**
Test 2	28.5687	20.6347	0.0204	1326.51	0.0011	0.8684	0.05
Test 3	27.3687	19.3946	0.0239	1554.10	0.0014	0.8369	0.1
Test 4	26.6034	18.5975	0.0264	1716.66	0.0017	0.8160	0.15
Test 5	26.0301	17.9965	0.0286	1859.72	0.0020	0.7999	0.2
Test 6	25.5648	17.5060	0.0305	1983.26	0.0022	0.7865	0.25
Test 7	25.1699	17.0876	0.0322	2093.81	0.0024	0.7748	0.3
Test 8	24.8244	16.7202	0.0338	2197.85	0.0026	0.7644	0.35
Test 9	24.5158	16.3906	0.0353	2295.38	0.0028	0.7550	0.4
Test 10	24.2362	16.0910	0.0367	2386.42	0.0030	0.7462	0.45
Test 11	23.9807	15.8163	0.0381	2477.45	0.0031	0.7382	0.5
Test 12	23.7453	15.5624	0.0393	2555.48	0.0033	0.7306	0.55
Test 13	23.5269	15.3262	0.0406	2640.02	0.0035	0.7235	0.6
Test 14	23.3231	15.1051	0.0417	2711.54	0.0037	0.7168	0.65
Test 15	23.1319	14.8972	0.0429	2789.57	0.0038	0.7105	0.7
Test 16	22.9518	14.7009	0.0439	2854.60	0.0040	0.7044	0.75
Test 17	22.7816	14.5148	0.0450	2926.13	0.0041	0.6987	0.8
Test 18	22.6202	14.3379	0.0460	2991.15	0.0043	0.6932	0.85
Test 19	22.4669	14.1694	0.0470	3056.18	0.0045	0.6879	0.9
Test 20	22.3207	14.0084	0.0480	3121.20	0.0046	0.6829	0.95
Test 21	22.2085	13.8845	0.0487	3166.72	0.0047	0.6790	0.99

Table A8: The effect of the regularization parameter β using the PSF of support size 13×13, where α=0.15 and β_{lat}=0.35 are fixed for the image "Bridge" and for the "photo" image $\alpha = 0.25$ and $\beta_{lat} = 0.001$, while β increase by a step size of 0.05

ii) Evaluation using PSF of support size 19x19

a) Evaluating the influence of the regularization parameter $\boldsymbol{\alpha}$ over the restoration quality by fixing $\boldsymbol{\beta_{lat}}$ and $\boldsymbol{\beta}$

Test	PSNR	SNR	$E(L_1)$ norm	L_1 norm	MSE	SSIM	$\boldsymbol{\alpha}$
« Bridge »							
Test 1	**22.3450**	**14.2008**	**0.0443**	**2880.61**	**0.0041**	**0.8826**	**0.001**

Test 2	21.0186	12.8150	0.0503	3270.76	0.0056	0.8181	0.05
Test 3	21.0076	12.7817	0.0506	3290.27	0.0056	0.8126	0.1
Test 4	20.8338	12.5872	0.0516	3355.29	0.0059	0.7991	0.15
Test 5	20.8202	12.5537	0.0519	3374.80	0.0059	0.7932	0.2
Test 6	20.6830	12.4004	0.0528	3433.32	0.0061	0.7817	0.25
Test 7	20.7373	12.4325	0.0528	3433.32	0.0060	0.7784	0.3
Test 8	20.5511	12.2357	0.0538	3498.35	0.0063	0.7647	0.35
Test 9	20.3576	12.0211	0.0551	3582.88	0.0065	0.7488	0.4
Test 10	20.3837	12.0322	0.0551	3582.88	0.0065	0.7449	0.45
Test 11	20.3006	11.9297	0.0558	3628.40	0.0066	0.7322	0.5
Test 12	20.3576	11.9685	0.0557	3621.89	0.0065	0.7298	0.55
Test 13	19.8532	11.4561	0.0584	3797.46	0.0074	0.6967	0.6
Test 14	19.8929	11.4828	0.0583	3790.96	0.0073	0.6952	0.65
Test 15	19.7893	11.3646	0.0590	3836.48	0.0075	0.6828	0.7
Test 16	19.9908	11.5409	0.0583	3790.96	0.0071	0.6825	0.75
Test 17	20.0286	11.5755	0.0581	3777.95	0.0071	0.6838	0.8
Test 18	19.8947	11.4305	0.0589	3829.97	0.0073	0.6708	0.85
Test 19	19.8600	11.3823	0.0592	3849.48	0.0073	0.6649	0.9
Test 20	19.6475	11.1593	0.0605	3934.01	0.0077	0.6412	0.95
Test 21	19.6669	11.1634	0.0605	3934.01	0.0077	0.6364	0.99
« Photo »							
Test 1	27.3370	19.5319	0.0217	1411.04	0.0015	0.9008	0.001
Test 2	**27.6787**	**19.9342**	**0.0205**	1333.01	**0.0013**	**0.9012**	**0.05**
Test 3	26.5211	18.6600	0.0245	1593.11	0.0017	0.8800	0.1
Test 4	26.5937	18.7184	0.0247	1606.12	0.0017	0.8776	0.15
Test 5	26.6028	18.7127	0.0251	1632.13	0.0017	0.8731	0.2
Test 6	26.6002	18.6968	0.0254	1651.64	0.0017	0.8692	0.25
Test 7	27.0564	19.1379	0.0248	1612.62	0.0015	0.8734	0.3
Test 8	26.9736	19.0422	0.0253	1645.13	0.0016	0.8689	0.35
Test 9	26.6070	18.6652	0.0262	1703.66	0.0017	0.8606	0.4
Test 10	26.3948	18.4429	0.0269	1749.17	0.0018	0.8543	0.45
Test 11	26.1603	18.1982	0.0278	1807.70	0.0019	0.8471	0.5
Test 12	25.9898	18.0178	0.0284	1846.71	0.0020	0.8422	0.55
Test 13	25.8057	17.8226	0.0291	1892.23	0.0021	0.8367	0.6
Test 14	25.3808	17.3863	0.0305	1983.26	0.0023	0.8256	0.65
Test 15	25.1675	17.1650	0.0313	2035.28	0.0024	0.8193	0.7
Test 16	25.1134	17.1031	0.0315	2048.29	0.0024	0.8167	0.75
Test 17	24.9763	16.9592	0.0320	2080.80	0.0025	0.8122	0.8
Test 18	24.9130	16.8897	0.0323	2100.31	0.0025	0.8096	0.85
Test 19	24.7187	16.6880	0.0330	2145.83	0.0027	0.8028	0.9
Test 20	24.5916	16.5557	0.0334	2171.84	0.0027	0.7990	0.95
Test 21	24.6434	16.6040	0.0334	2171.84	0.0027	0.8000	0.99

Table A9: The effect of the regularization parameter α using the PSF of support size 19×19, where β_{lat}=0.005 and β=0.003 are fixed for the image "Bridge" and for the "Photo" image $\beta_{lat} = 0.004$ and $\beta = 0.002$, while α increase by a step size of 0.05

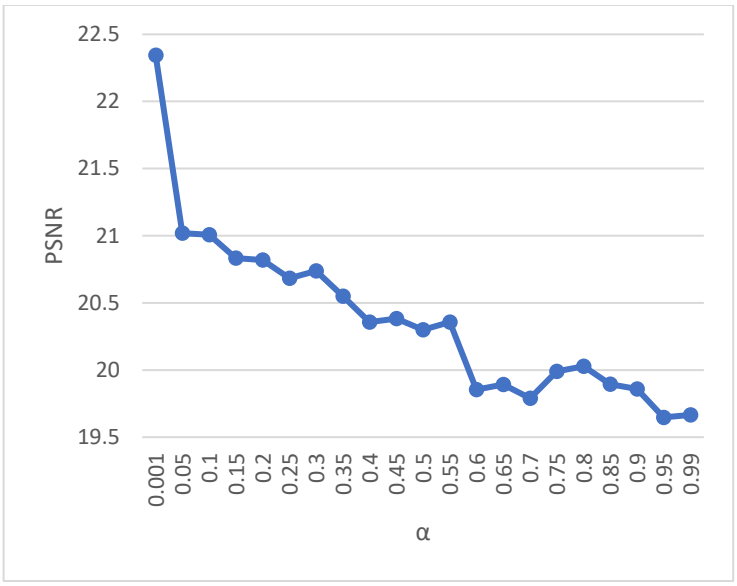

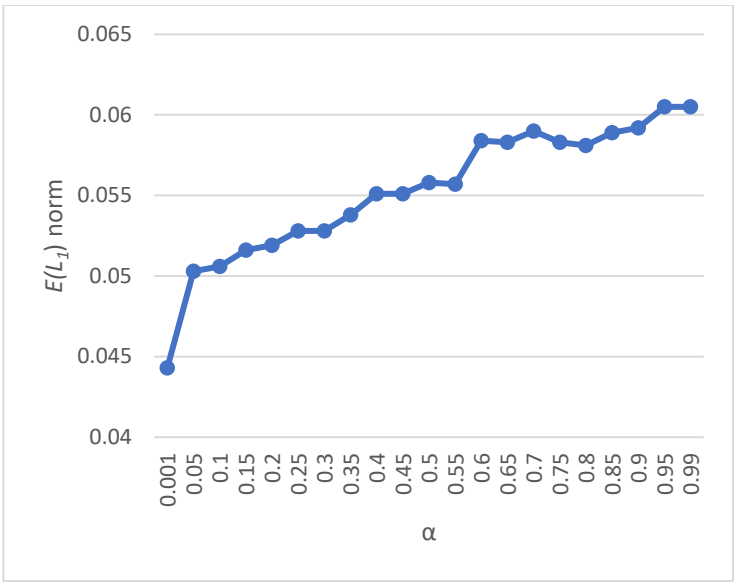

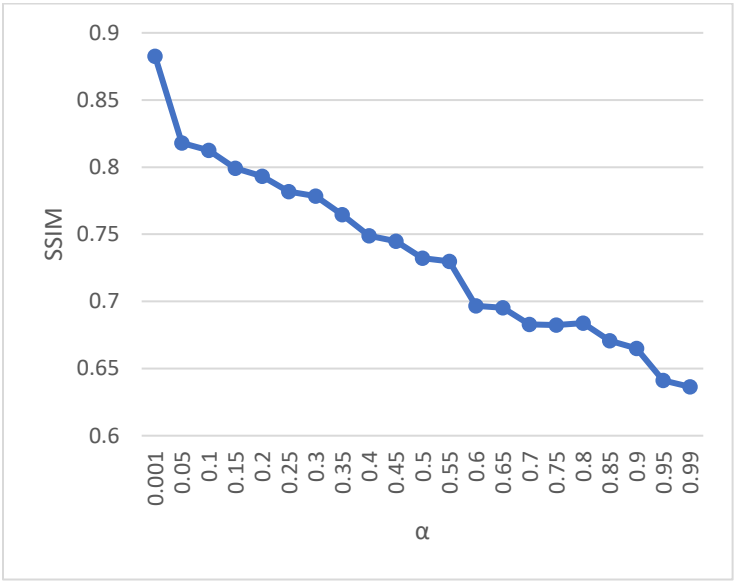

Figure A7: The effect of the regularization parameter α over the PSNR (top left), E(L_1) norm (Top right), and SSIM (middle) for the "Bridge" image using a PSF of support size 19x19 and fixing $\beta_{lat} = 0.005$ and $\beta = 0.003$

Figure A8: The effect of the regularization parameter α over the PSNR (top left), E(L_1) norm (Top right), and SSIM (middle) for the "Photo" image using a PSF of support size 19x19 and fixing $\beta_{lat} = 0.004$ and $\beta = 0.002$

b) Evaluating the influence of the regularization parameter β_{lat} over the restoration quality by fixing α and β

Test	PSNR	SNR	$E(L_1)$ norm	$L1$ norm	MSE	SSIM	$\boldsymbol{\beta_{lat}}$
« Bridge »							
Test 1	20.4485	12.3055	0.0524	3407.31	0.0064	0.8017	0.001
Test 2	19.6254	11.4376	0.0583	3790.96	0.0077	0.7303	0.05
Test 3	19.2971	11.1131	0.0603	3921.01	0.0084	0.7077	0.1
Test 4	19.8277	11.6475	0.0570	3706.43	0.0074	0.7383	0.15
Test 5	19.9009	11.7313	0.0565	3673.91	0.0073	0.7436	0.2
Test 6	19.8541	11.6926	0.0566	3680.42	0.0074	0.7423	0.25
Test 7	19.4777	11.3338	0.0586	3810.47	0.0080	0.7238	0.3
Test 8	20.5714	12.4509	0.0525	3413.81	0.0062	0.7944	0.35

Test 9	21.6942	13.5743	0.0472	3069.18	0.0048	0.8443	0.4
Test 10	**21.7601**	**13.6567**	**0.0469**	**3049.67**	**0.0047**	**0.8513**	**0.45**
Test 11	21.3706	13.2705	0.0486	3160.22	0.0052	0.8346	0.5
Test 12	21.4548	13.3658	0.0482	3134.21	0.0051	0.8411	0.55
Test 13	21.4652	13.3858	0.0482	3134.21	0.0051	0.8426	0.6
Test 14	21.2274	13.1530	0.0494	3212.24	0.0054	0.8328	0.65
Test 15	21.2223	13.1627	0.0494	3212.24	0.0054	0.8357	0.7
Test 16	19.4929	11.4553	0.0580	3771.45	0.0080	0.7587	0.75
Test 17	17.5590	9.5448	0.0704	4577.76	0.0125	0.6300	0.8
Test 18	17.2537	9.2601	0.0729	4740.32	0.0134	0.6073	0.85
Test 19	16.9508	8.9719	0.0755	4909.39	0.0143	0.5875	0.9
Test 20	17.0454	9.0716	0.0748	4863.87	0.0140	0.5971	0.95
Test 21	16.6009	8.6337	0.0788	5123.97	0.0155	0.5597	0.99
« Photo »							
Test 1	26.9868	19.1388	0.0233	1515.08	0.0016	0.8912	0.001
Test 2	**27.4599**	**19.6416**	**0.0221**	**1437.05**	**0.0014**	**0.8965**	**0.05**
Test 3	26.0654	18.2502	0.0243	1580.11	0.0019	0.8789	0.1
Test 4	23.2608	15.4454	0.0323	2100.31	0.0037	0.8154	0.15
Test 5	23.3759	15.5652	0.0320	2080.80	0.0036	0.8199	0.2
Test 6	22.9789	15.1753	0.0334	2171.84	0.0040	0.8100	0.25
Test 7	22.9052	15.1049	0.0337	2191.34	0.0040	0.8080	0.3
Test 8	21.9266	14.1324	0.0374	2431.94	0.0050	0.7788	0.35
Test 9	21.4009	13.6022	0.0394	2561.99	0.0057	0.7583	0.4
Test 10	21.2553	13.4596	0.0401	2607.50	0.0059	0.7530	0.45
Test 11	20.8569	13.0614	0.0419	2724.55	0.0064	0.7369	0.5
Test 12	21.1177	13.3311	0.0410	2666.03	0.0061	0.7475	0.55
Test 13	20.6770	12.8771	0.0425	2763.56	0.0067	0.7278	0.6
Test 14	20.6950	12.8994	0.0424	2757.06	0.0067	0.7290	0.65
Test 15	20.5698	12.7746	0.0431	2802.58	0.0069	0.7244	0.7
Test 16	20.2331	12.4371	0.0447	2906.62	0.0074	0.7098	0.75
Test 17	19.1238	11.3287	0.0505	3283.76	0.0096	0.6599	0.8
Test 18	18.7862	10.9955	0.0531	3452.83	0.0104	0.6395	0.85
Test 19	18.7239	10.9357	0.0536	3485.34	0.0105	0.6363	0.9
Test 20	18.6535	10.8663	0.0541	3517.85	0.0107	0.6323	0.95
Test 21	18.7256	10.9381	0.0538	3498.35	0.0105	0.6342	0.99

Table A10: The effect of the regularization parameter β_{lat} using the PSF of support size 19×19, where $\alpha = 0.001$ and $\beta = 0.003$ are fixed for the image "Bridge" and for the "photo" image $\alpha = 0.05$ and $\beta = 0.002$, while β_{lat} increase by a step size of 0.05

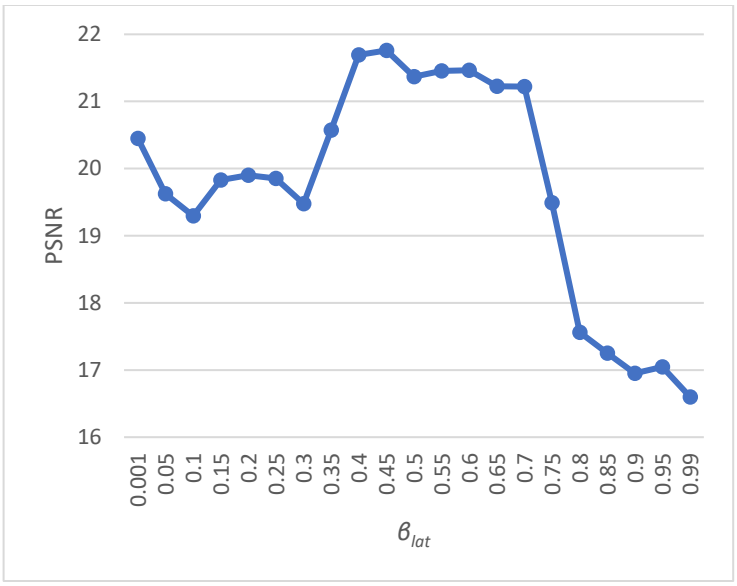

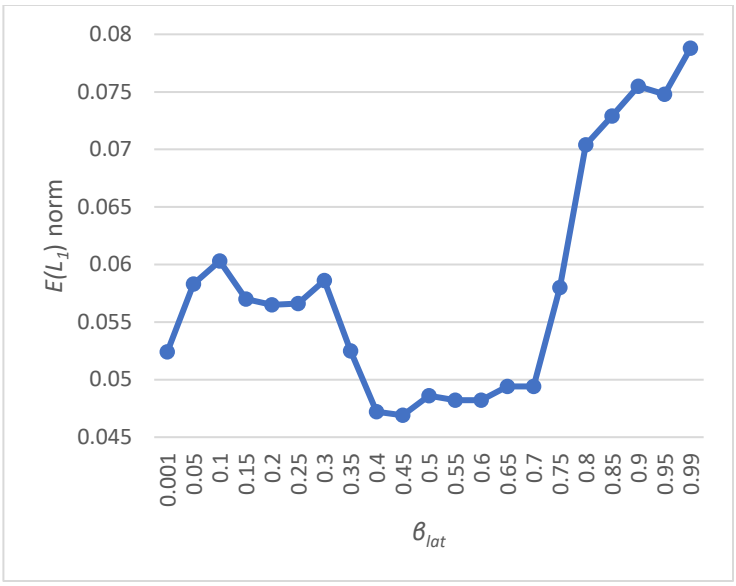

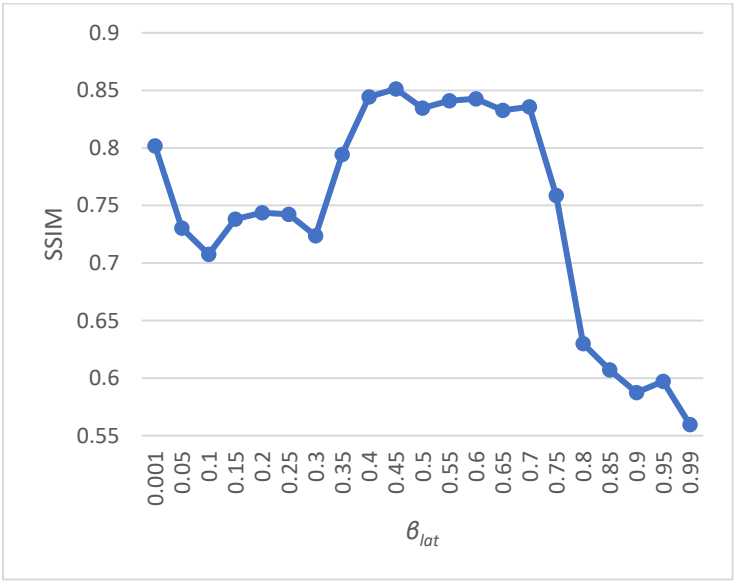

Figure A9: The effect of the regularization parameter β_{lat} over the PSNR (top left), E(L_1) norm (Top right), and SSIM (middle) for the "Bridge" image using a PSF of support size 19x19 and fixing $\alpha = 0.001$ and $\beta = 0.003$

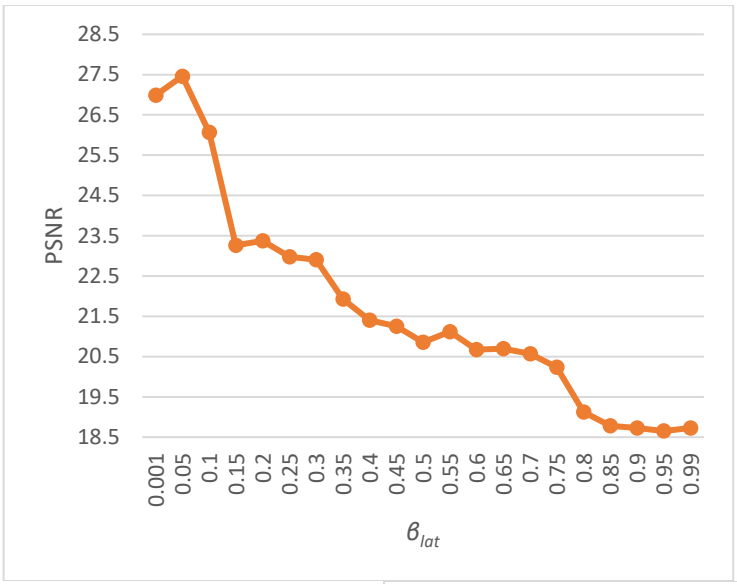

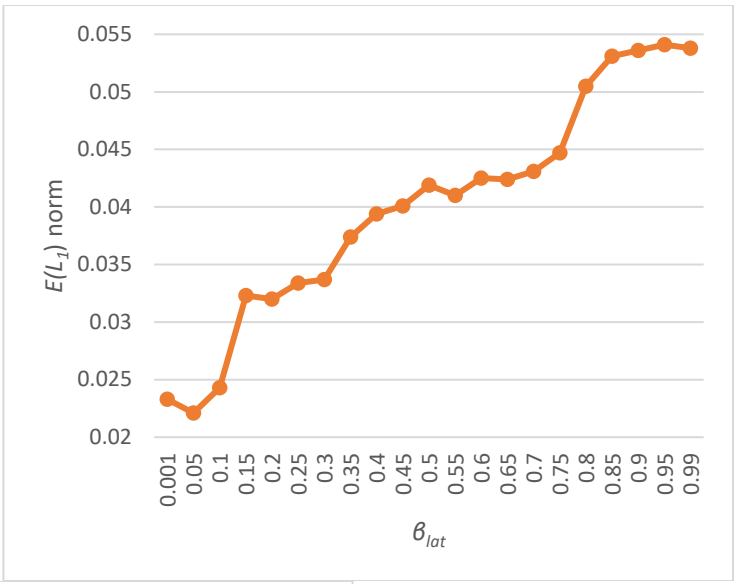

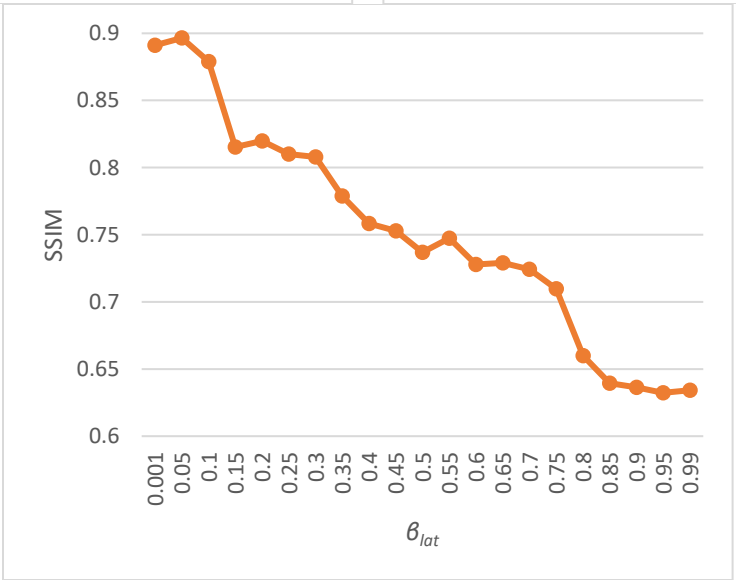

Figure A10: The effect of the regularization parameter β_{lat} over the PSNR (top left), E(L_1) norm (Top right), and SSIM (middle) for the "Photo" image using a PSF of support size 19x19 and fixing $\alpha = 0.05$ and $\beta_{lat} = 0.002$

c) Evaluating the influence of the regularization parameter β over the restoration quality by fixing β_{lat} and α

Test	PSNR	SNR	$E(L_1)$ norm	L_1 norm	MSE	SSIM	$\boldsymbol{\beta}$
« Bridge »							
Test 1	**21.9133**	**13.8435**	**0.0457**	**2971.64**	**0.0046**	**0.8819**	**0.001**
Test 2	21.0529	12.6448	0.0535	3478.84	0.0056	0.7087	0.05
Test 3	20.5311	12.0456	0.0571	3712.93	0.0063	0.6555	0.1
Test 4	20.2560	11.7182	0.0592	3849.48	0.0067	0.6262	0.15
Test 5	20.0668	11.4874	0.0609	3960.02	0.0070	0.6059	0.2
Test 6	19.9194	11.3046	0.0622	4044.56	0.0072	0.5904	0.25
Test 7	19.7967	11.1508	0.0633	4116.08	0.0074	0.5777	0.3
Test 8	19.6906	11.0168	0.0643	4181.11	0.0076	0.5670	0.35

Test 9	19.5968	10.8973	0.0652	4239.63	0.0078	0.5577	0.4
Test 10	19.5126	10.7893	0.0660	4291.65	0.0080	0.5496	0.45
Test 11	19.4364	10.6908	0.0668	4343.67	0.0081	0.5423	0.5
Test 12	19.3665	10.6000	0.0675	4389.19	0.0082	0.5358	0.55
Test 13	19.3021	10.5159	0.0681	4428.20	0.0083	0.5299	0.6
Test 14	19.2421	10.4372	0.0687	4467.22	0.0085	0.5245	0.65
Test 15	19.1859	10.3632	0.0693	4506.23	0.0086	0.5195	0.7
Test 16	19.1330	10.2933	0.0698	4538.75	0.0087	0.5149	0.75
Test 17	19.0830	10.2269	0.0703	4571.26	0.0088	0.5106	0.8
Test 18	19.0354	10.1636	0.0708	4603.77	0.0089	0.5066	0.85
Test 19	18.9900	10.1030	0.0713	4636.28	0.0090	0.5028	0.9
Test 20	18.9465	10.0447	0.0717	4662.29	0.0091	0.4992	0.95
Test 21	18.9130	9.9996	0.0721	4688.30	0.0091	0.4965	0.99
« Photo »							
Test 1	**26.6481**	**18.8275**	**0.0235**	**1528.09**	**0.0017**	**0.8924**	**0.001**
Test 2	25.4181	17.4450	0.0300	1950.75	0.0023	0.7933	0.05
Test 3	24.6015	16.5817	0.0334	2171.84	0.0027	0.7638	0.1
Test 4	24.0911	16.0352	0.0358	2327.90	0.0031	0.7453	0.15
Test 5	23.7000	15.6132	0.0379	2464.45	0.0034	0.7310	0.2
Test 6	23.3745	15.2598	0.0397	2581.49	0.0036	0.7190	0.25
Test 7	23.0922	14.9521	0.0414	2692.04	0.0039	0.7084	0.3
Test 8	22.8415	14.6778	0.0429	2789.57	0.0041	0.6990	0.35
Test 9	22.6149	14.4290	0.0443	2880.61	0.0043	0.6905	0.4
Test 10	22.4078	14.2008	0.0457	2971.64	0.0045	0.6827	0.45
Test 11	22.2173	13.9901	0.0469	3049.67	0.0047	0.6755	0.5
Test 12	22.0413	13.7946	0.0481	3127.70	0.0049	0.6688	0.55
Test 13	21.8779	13.6126	0.0492	3199.23	0.0051	0.6626	0.6
Test 14	21.7255	13.4422	0.0503	3270.76	0.0053	0.6568	0.65
Test 15	21.5827	13.2821	0.0514	3342.29	0.0055	0.6514	0.7
Test 16	21.4482	13.1310	0.0524	3407.31	0.0056	0.6464	0.75
Test 17	21.3208	12.9876	0.0533	3465.83	0.0058	0.6416	0.8
Test 18	21.1997	12.8509	0.0542	3524.36	0.0060	0.6371	0.85
Test 19	21.0842	12.7201	0.0551	3582.88	0.0061	0.6328	0.9
Test 20	20.9736	12.5946	0.0560	3641.40	0.0063	0.6287	0.95
Test 21	20.8884	12.4977	0.0567	3686.92	0.0064	0.6256	0.99

Table A11: The effect of the regularization parameter β using the PSF of support size 19×19, where $\alpha = 0.001$ and $\beta_{lat} = 0.005$ are fixed for the image "Bridge" and for the "photo" image $\alpha = 0.05$ and $\beta_{lat} = 0.004$, while β increase by a step size of 0.05

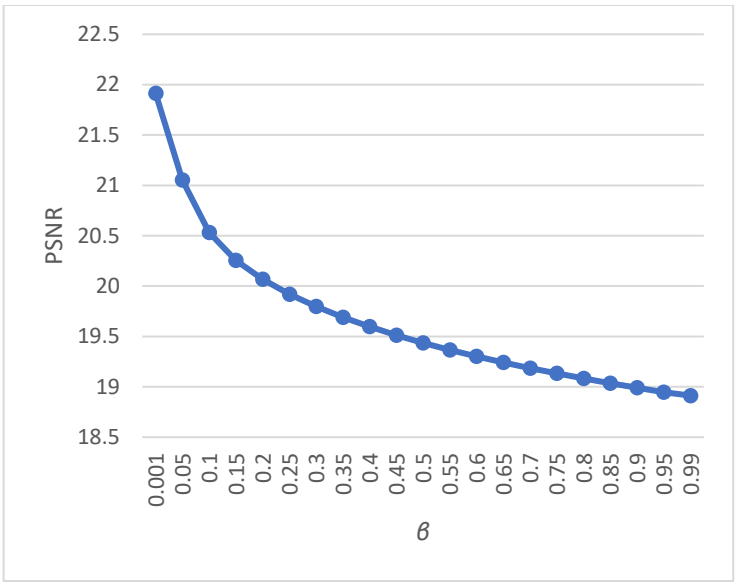

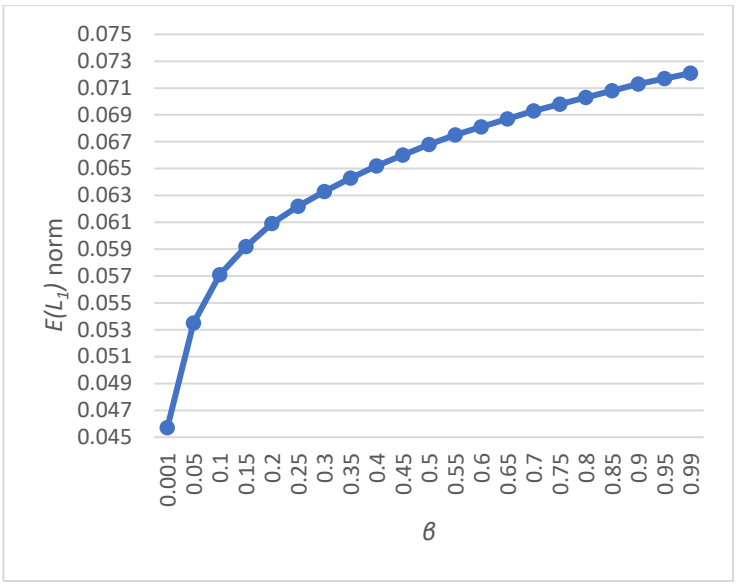

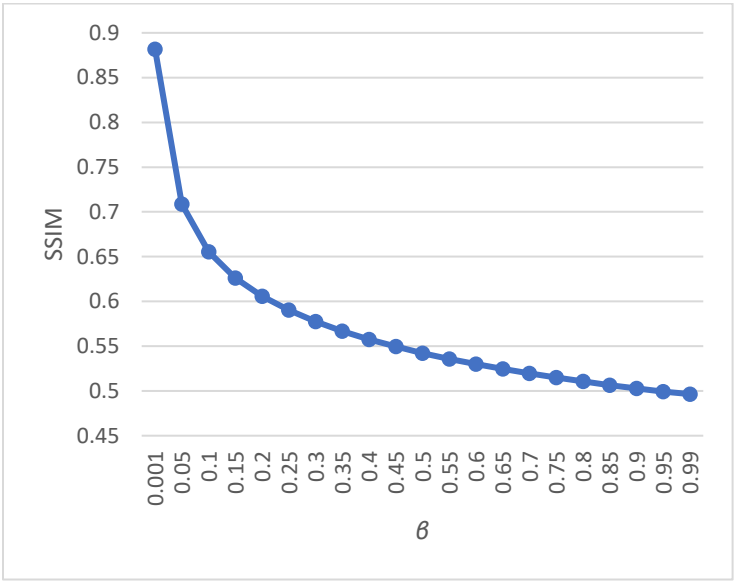

Figure A11: The effect of the regularization parameter β over the PSNR (top left), E(L_1) norm (Top right), and SSIM (middle) for the "Bridge" image using a PSF of support size 19x19 and fixing $\alpha = 0.001$ and $\beta_{lat} = 0.005$

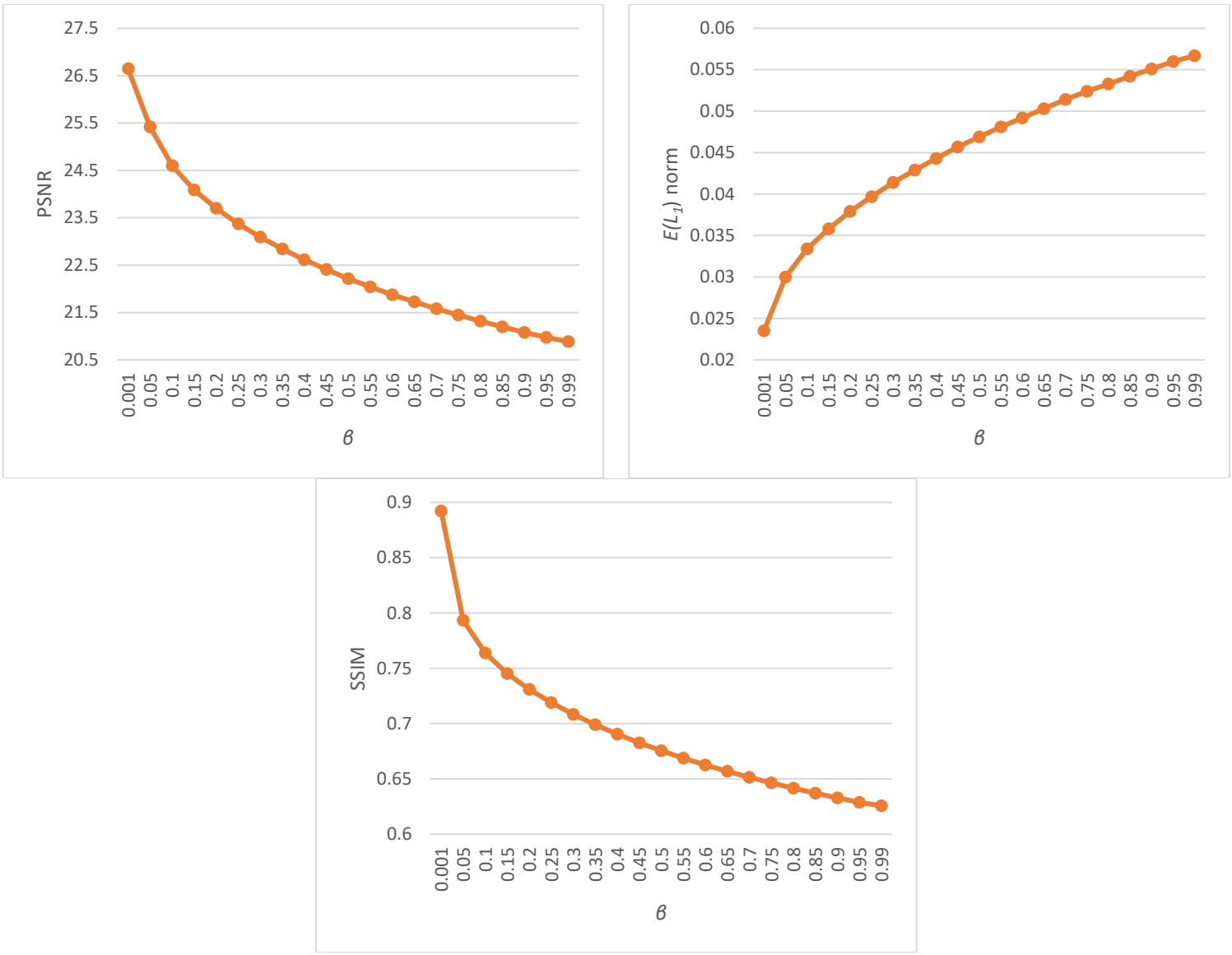

Figure A12: The effect of the regularization parameter β over the PSNR (top left), E(L_1) norm (Top right), and SSIM (middle) for the "Photo" image using a PSF of support size 19x19 and fixing $\alpha = 0.05$ and $\beta_{lat} = 0.004$

iii) Evaluation using PSF of support size 23x23

a) Evaluating the influence of the regularization parameter α over the restoration quality by fixing β_{lat} and β

Test	PSNR	SNR	$E(L_1)$ norm	L_1 norm	MSE	SSIM	α
	« Bridge »						
Test 1	16.3907	7.6206	0.0861	5598.65	0.0163	0.4298	0.001
Test 2	16.5657	7.7184	0.0857	5572.64	0.0157	0.4274	0.05
Test 3	16.8138	7.9200	0.0844	5488.11	0.0148	0.4293	0.1
Test 4	16.9954	8.1236	0.0832	5410.08	0.0142	0.4364	0.15
Test 5	17.1428	8.2228	0.0830	5397.08	0.0137	0.4367	0.2
Test 6	17.2279	8.2853	0.0827	5377.57	0.0135	0.4374	0.25

Test 7	17.3348	8.3580	0.0823	5351.56	0.0131	0.4386	0.3
Test 8	17.4604	8.4523	0.0817	5312.54	0.0128	0.4414	0.35
Test 9	17.4686	**8.4584**	**0.0817**	**5312.54**	**0.0127**	**0.4415**	**0.4**
Test 10	17.4688	8.4576	0.0817	5312.54	0.0127	0.4415	0.45
Test 11	17.4678	8.4562	0.0817	5312.54	0.0127	0.4415	0.5
Test 12	**17.4696**	8.4559	0.0818	5319.05	0.0127	0.4414	0.55
Test 13	17.4677	8.4553	0.0817	5312.54	0.0127	0.4415	0.6
Test 14	17.4686	8.4555	0.0817	5312.54	0.0127	0.4414	0.65
Test 15	17.4669	8.4535	0.0817	5312.54	0.0127	0.4415	0.7
Test 16	17.4670	8.4534	0.0817	5312.54	0.0127	0.4415	0.75
Test 17	17.4654	8.4507	0.0817	5312.54	0.0127	0.4415	0.8
Test 18	17.4558	8.4377	0.0817	5312.54	0.0128	0.4411	0.85
Test 19	17.4117	8.3865	0.0817	5312.54	0.0129	0.4388	0.9
Test 20	17.4099	8.3842	0.0817	5312.54	0.0129	0.4387	0.95
Test 21	17.4624	8.4512	0.0818	5319.05	0.0128	0.4413	0.99
	« Photo »						
Test 1	**20.9303**	**12.7403**	**0.0524**	**3407.31**	**0.0063**	**0.6457**	**0.001**
Test 2	20.4731	12.2604	0.0547	3556.87	0.0070	0.6338	0.05
Test 3	20.2151	11.9975	0.0560	3641.40	0.0075	0.6263	0.1
Test 4	20.0129	11.7892	0.0570	3706.43	0.0078	0.6207	0.15
Test 5	20.5478	12.3200	0.0546	3550.37	0.0069	0.6354	0.2
Test 6	20.7325	12.5017	0.0538	3498.35	0.0066	0.6405	0.25
Test 7	20.1939	11.9555	0.0564	3667.41	0.0075	0.6252	0.3
Test 8	20.0143	11.7716	0.0574	3732.44	0.0078	0.6196	0.35
Test 9	20.2468	12.0020	0.0563	3660.91	0.0074	0.6258	0.4
Test 10	20.8172	12.5758	0.0537	3491.84	0.0065	0.6418	0.45
Test 11	20.8352	12.5895	0.0538	3498.35	0.0065	0.6416	0.5
Test 12	20.5665	12.3104	0.0552	3589.38	0.0069	0.6330	0.55
Test 13	20.8067	12.5501	0.0543	3530.86	0.0065	0.6402	0.6
Test 14	20.7906	12.5276	0.0545	3543.86	0.0065	0.6397	0.65
Test 15	20.5895	12.3116	0.0560	3641.40	0.0069	0.6346	0.7
Test 16	20.5432	12.2573	0.0564	3667.41	0.0069	0.6336	0.75
Test 17	20.3741	12.0760	0.0576	3745.44	0.0072	0.6296	0.8
Test 18	20.2765	11.9703	0.0583	3790.96	0.0074	0.6282	0.85
Test 19	20.0812	11.7623	0.0597	3881.99	0.0077	0.6228	0.9
Test 20	19.8442	11.5108	0.0613	3986.03	0.0081	0.6170	0.95
Test 21	19.7021	11.3600	0.0623	4051.06	0.0084	0.6137	0.99

Table A12: The effect of the regularization parameter α using the PSF of support size 23×23, where $\beta_{lat} = 0.001$ and $\beta = 0.4$ are fixed for the image "Bridge" and for the "photo" image $\beta_{lat} = 0.4$ and $\beta = 0.25$, while α increase by a step size of 0.05

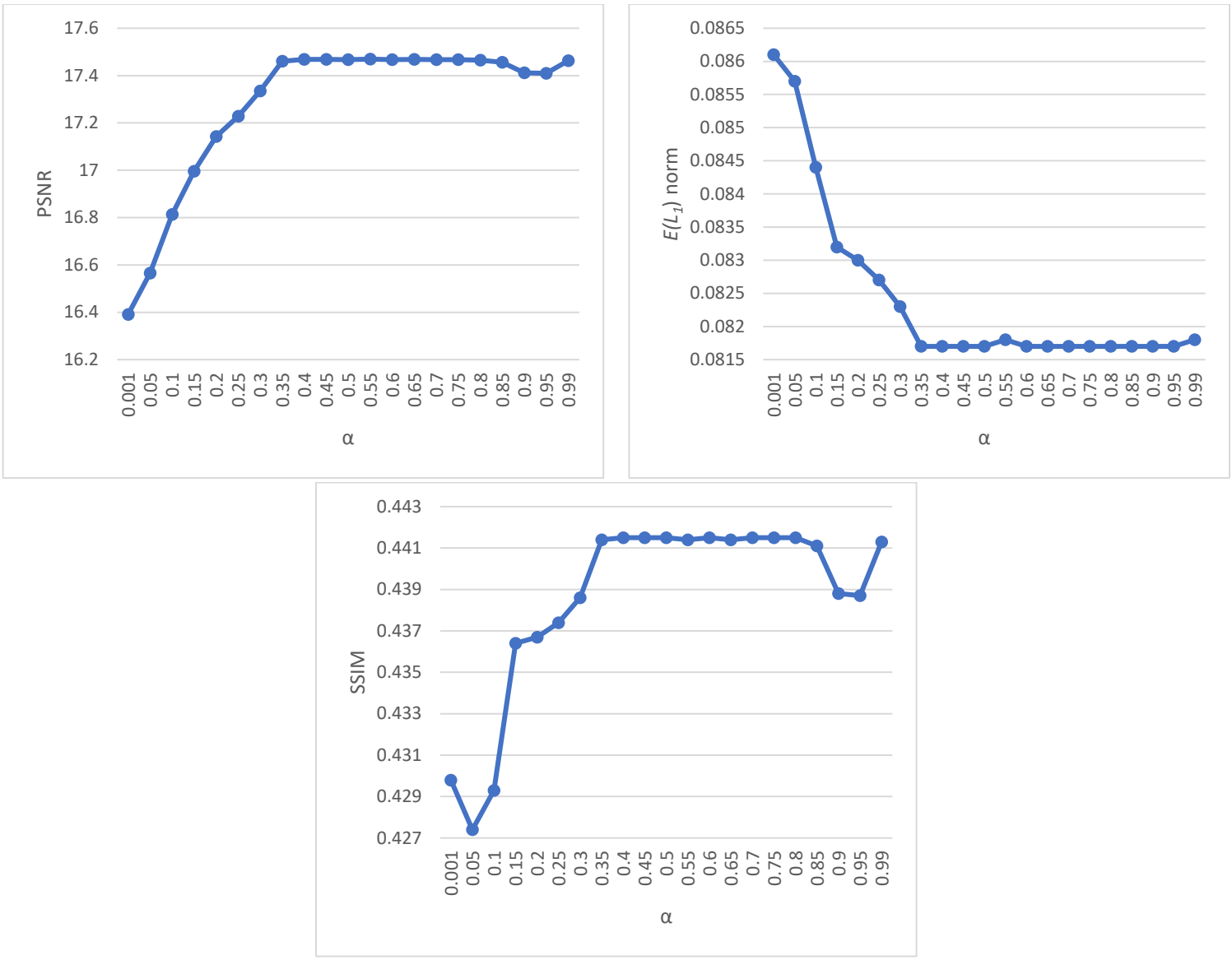

Figure A13: The effect of the regularization parameter α over the PSNR (top left), E(L_1) norm (Top right), and SSIM (middle) for the "Bridge" image using a PSF of support size 23x23 and fixing $\beta_{lat} = 0.001$ *and* $\beta = 0.4$

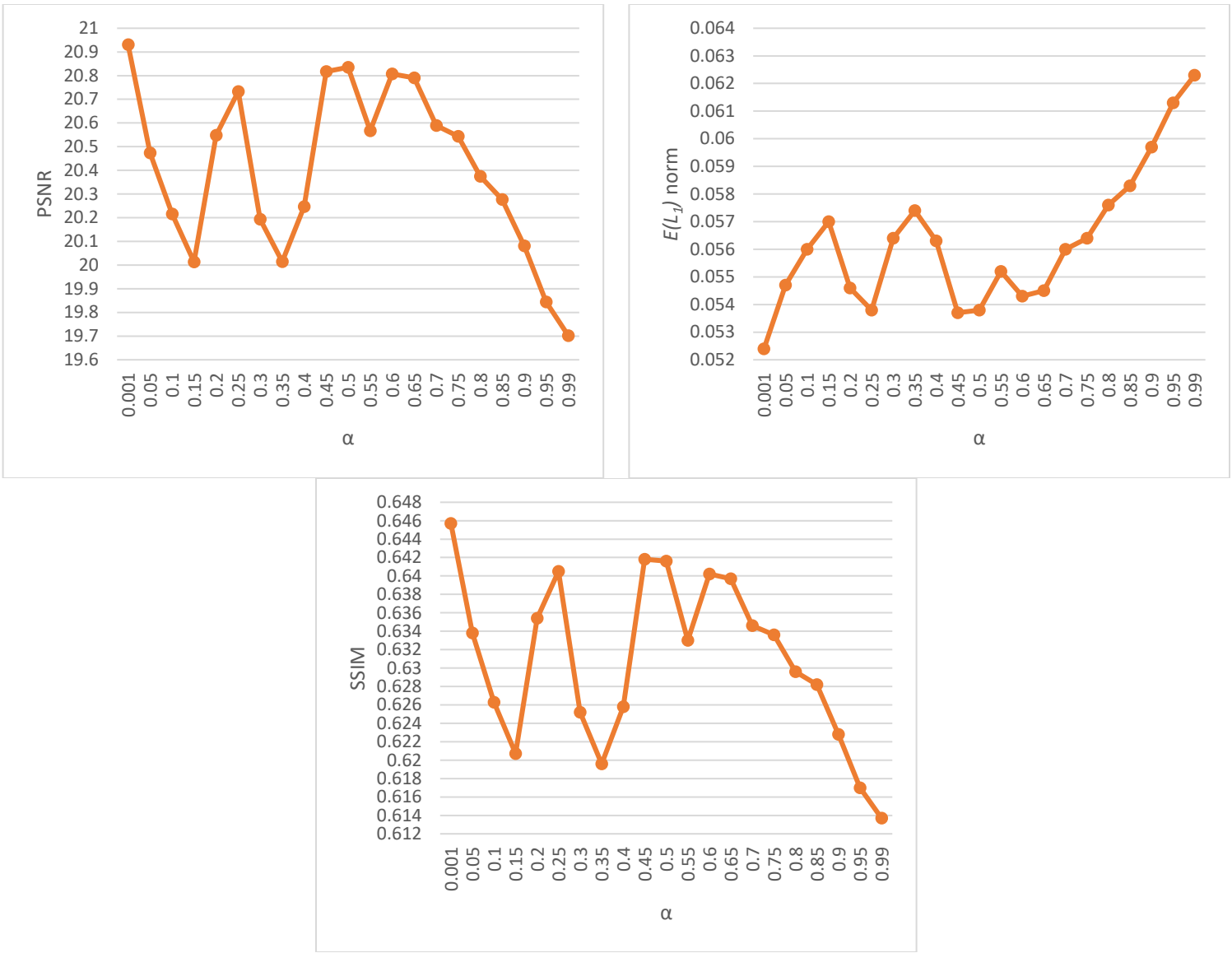

Figure A14: The effect of the regularization parameter α over the PSNR (top left), E(L_1) norm (Top right), and SSIM (middle) for the "Photo" image using a PSF of support size 23x23 and fixing $\beta_{lat} = 0.4$ and $\beta = 0.25$

b) Evaluating the influence of the regularization parameter β_{lat} over the restoration quality by fixing α and β

Test	PSNR	SNR	$E(L_1)$ norm	L_1 norm	MSE	SSIM	β_{lat}
	« Bridge »						
Test 1	17.4686	8.4584	0.0817	5312.54	0.0127	0.4415	0.001
Test 2	17.3757	8.3944	0.0824	5358.06	0.0130	0.4386	0.05
Test 3	**17.6798**	**8.6968**	**0.0800**	**5202.00**	**0.0121**	**0.4415**	**0.1**
Test 4	16.7706	7.8300	0.0882	5735.21	0.0150	0.4080	0.15
Test 5	16.4818	7.5483	0.0910	5917.28	0.0160	0.3949	0.2
Test 6	16.3652	7.4437	0.0921	5988.80	0.0164	0.3897	0.25
Test 7	16.3101	7.3920	0.0926	6021.32	0.0166	0.3874	0.3
Test 8	16.0360	7.1226	0.0955	6209.89	0.0177	0.3780	0.35

Test 9	16.0605	7.1458	0.0952	6190.38	0.0176	0.3779	0.4
Test 10	16.0279	7.1163	0.0955	6209.89	0.0177	0.3766	0.45
Test 11	15.8416	6.9356	0.0975	6339.94	0.0185	0.3697	0.5
Test 12	15.7880	6.8801	0.0981	6378.95	0.0187	0.3677	0.55
Test 13	15.3258	6.4424	0.1029	6691.07	0.0209	0.3487	0.6
Test 14	15.2660	6.3865	0.1036	6736.59	0.0211	0.3473	0.65
Test 15	15.2186	6.3426	0.1041	6769.10	0.0214	0.3456	0.7
Test 16	15.2152	6.3439	0.1041	6769.10	0.0214	0.3457	0.75
Test 17	15.1899	6.3269	0.1043	6782.11	0.0215	0.3450	0.8
Test 18	15.1919	6.3340	0.1042	6775.61	0.0215	0.3455	0.85
Test 19	15.1301	6.2746	0.1049	6821.12	0.0218	0.3436	0.9
Test 20	15.1075	6.2539	0.1051	6834.13	0.0219	0.3430	0.95
Test 21	15.0435	6.1942	0.1059	6886.15	0.0223	0.3414	0.99
	« Photo »						
Test 1	19.1983	11.0234	0.0613	3986.03	0.0094	0.5955	0.001
Test 2	19.5722	11.3968	0.0592	3849.48	0.0087	0.6070	0.05
Test 3	19.9835	11.8035	0.0570	3706.43	0.0079	0.6197	0.1
Test 4	19.9916	11.8142	0.0569	3699.92	0.0079	0.6198	0.15
Test 5	19.8931	11.7069	0.0574	3732.44	0.0081	0.6170	0.2
Test 6	20.4444	12.2587	0.0546	3550.37	0.0071	0.6329	0.25
Test 7	20.0550	11.8648	0.0565	3673.91	0.0078	0.6221	0.3
Test 8	20.3978	12.2103	0.0548	3563.37	0.0072	0.6315	0.35
Test 9	**20.9303**	**12.7403**	**0.0524**	**3407.31**	**0.0063**	**0.6457**	**0.4**
Test 10	20.6740	12.4815	0.0536	3485.34	0.0067	0.6391	0.45
Test 11	20.7206	12.5263	0.0534	3472.34	0.0067	0.6405	0.5
Test 12	20.5383	12.3417	0.0543	3530.86	0.0069	0.6356	0.55
Test 13	20.4707	12.2735	0.0546	3550.37	0.0070	0.6337	0.6
Test 14	20.4736	12.2775	0.0546	3550.37	0.0070	0.6337	0.65
Test 15	20.2867	12.0892	0.0554	3602.39	0.0074	0.6284	0.7
Test 16	20.5728	12.3763	0.0541	3517.85	0.0069	0.6363	0.75
Test 17	20.2462	12.0494	0.0556	3615.39	0.0074	0.6273	0.8
Test 18	20.0549	11.8574	0.0566	3680.42	0.0078	0.6219	0.85
Test 19	20.0407	11.8425	0.0567	3686.92	0.0078	0.6214	0.9
Test 20	19.8194	11.6188	0.0578	3758.45	0.0082	0.6156	0.95
Test 21	19.7255	11.5255	0.0582	3784.46	0.0084	0.6130	0.99

Table A13: The effect of the regularization parameter β_{lat} using the PSF of support size 23×23, where $\alpha = 0.4$ and $\beta = 0.4$ are fixed for the image "Bridge" and for the "photo" image $\alpha = 0.001$ and $\beta = 0.25$, while β_{lat} increase by a step size of 0.05

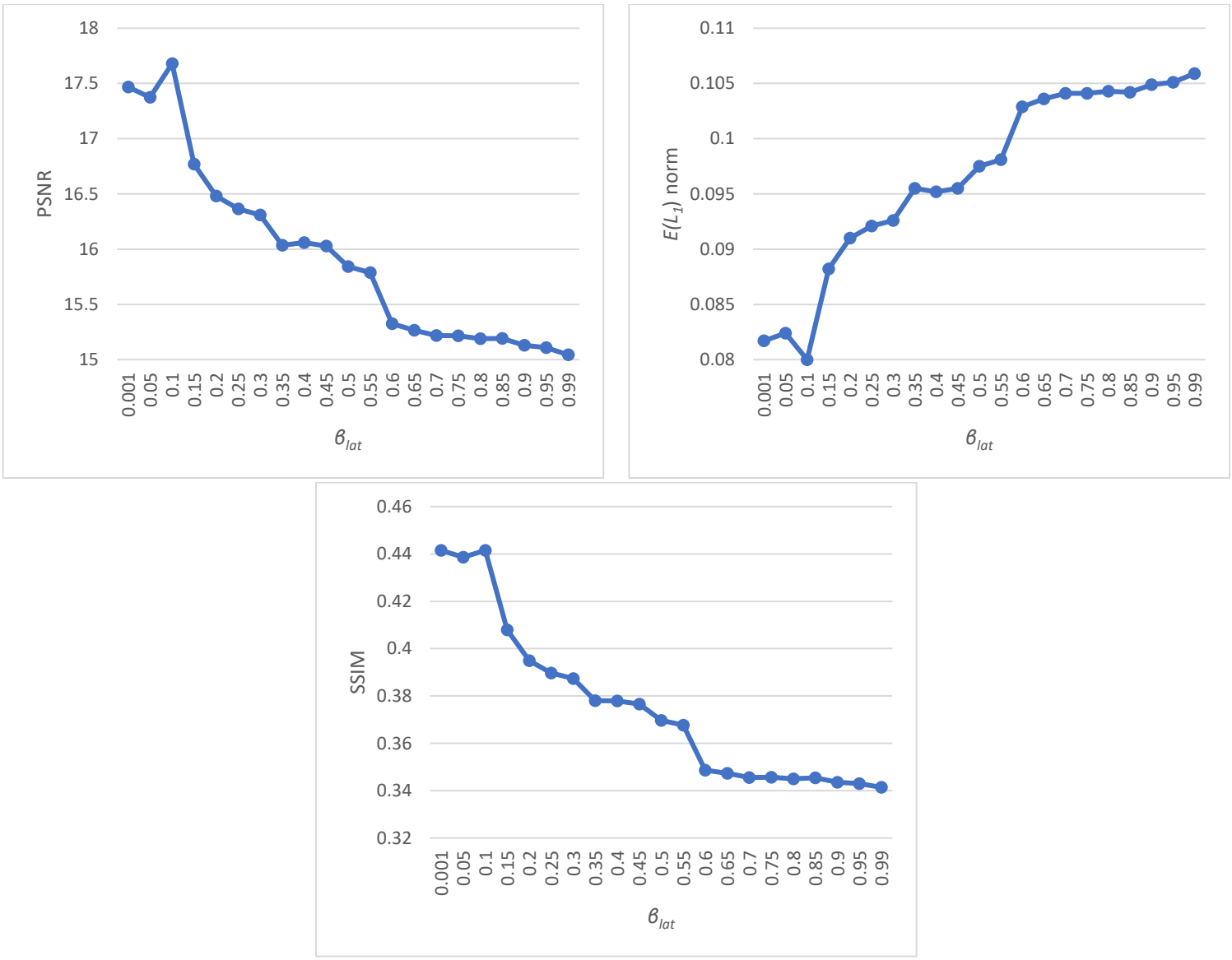

Figure A15: The effect of the regularization parameter β_{lat} over the PSNR (top left), E(L_1) norm (Top right), and SSIM (middle) for the "Bridge" image using a PSF of support size 23x23 and fixing $\alpha = 0.4$ and $\beta = 0.4$

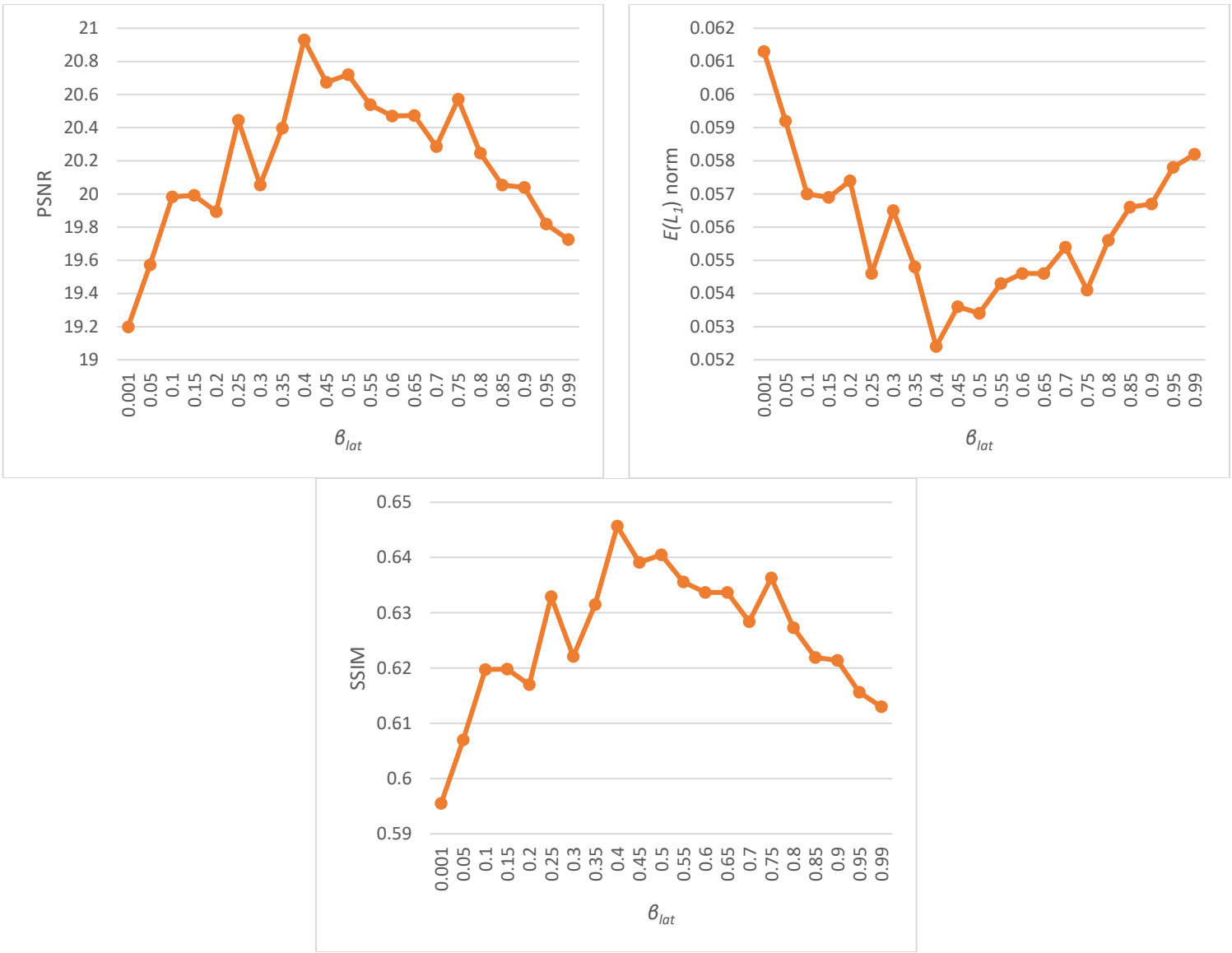

Figure A16: The effect of the regularization parameter β_{lat} over the PSNR (top left), E(L_1) norm (Top right), and SSIM (middle) for the "Photo" image using a PSF of support size 23x23 and fixing $\alpha = 0.001$ and $\beta = 0.25$

c) Evaluating the influence of the regularization parameter β over the restoration quality by fixing β_{lat} and α

Test	PSNR	SNR	$E(L_1)$ norm	L_1 norm	MSE	SSIM	$\boldsymbol{\beta}$
	« Bridge »						
Test 1	16.4545	7.7447	0.0866	5631.17	0.0161	0.3560	0.001
Test 2	17.1848	8.3651	0.0811	5273.53	0.0136	0.4226	0.05
Test 3	17.3774	8.5198	0.0801	5208.50	0.0130	0.4342	0.1
Test 4	17.4882	8.6023	0.0797	5182.49	0.0127	0.4391	0.15
Test 5	17.5601	8.6508	0.0797	5182.49	0.0125	0.4414	0.2
Test 6	17.6087	8.6783	0.0798	5189.00	0.0123	0.4423	0.25
Test 7	17.6423	8.6930	0.0797	5182.49	0.0122	0.4424	0.3
Test 8	17.6851	**8.6984**	**0.0796**	**5175.99**	**0.0121**	**0.4424**	**0.35**

Test 9	17.6798	8.6968	0.0800	5202.00	0.0121	0.4415	0.4
Test 10	17.6885	8.6902	0.0802	5215.01	0.0121	0.4407	0.45
Test 11	17.6928	8.6797	0.0804	5228.01	0.0121	0.4398	0.5
Test 12	**17.6934**	8.6662	0.0806	5241.02	0.0121	0.4388	0.55
Test 13	17.6912	8.6505	0.0809	5260.52	0.0121	0.4378	0.6
Test 14	17.6866	8.6329	0.0811	5273.53	0.0121	0.4366	0.65
Test 15	17.6801	8.6138	0.0813	5286.53	0.0121	0.4355	0.7
Test 16	17.6721	8.5937	0.0816	5306.04	0.0122	0.4344	0.75
Test 17	17.6628	8.5727	0.0818	5319.05	0.0122	0.4332	0.8
Test 18	17.6524	8.5510	0.0821	5338.55	0.0122	0.4321	0.85
Test 19	17.6412	8.5288	0.0823	5351.56	0.0122	0.4310	0.9
Test 20	17.6293	8.5062	0.0826	5371.07	0.0123	0.4299	0.95
Test 21	17.6193	8.4879	0.0828	5384.07	0.0123	0.4290	0.99
	« Photo »						
Test 1	19.7322	11.9807	0.0499	3244.75	0.0084	0.6617	0.001
Test 2	**21.6381**	**13.8188**	**0.0424**	**2757.06**	**0.053**	**0.7111**	**0.05**
Test 3	21.6014	13.5681	0.0457	2971.64	0.0054	0.6932	0.1
Test 4	21.3758	13.2615	0.0484	3147.21	0.0057	0.6735	0.15
Test 5	21.1392	12.9843	0.0506	3290.27	0.0060	0.6581	0.2
Test 6	20.9303	12.7403	0.0524	3407.31	0.0063	0.6457	0.25
Test 7	20.7452	12.5240	0.0541	3517.85	0.0066	0.6354	0.3
Test 8	20.5788	12.3294	0.0556	3615.39	0.0069	0.6266	**0.35**
Test 9	20.4273	12.1518	0.0569	3699.92	0.0071	0.6189	0.4
Test 10	20.2875	11.9875	0.0582	3784.46	0.0074	0.6121	0.45
Test 11	20.1581	11.8349	0.0594	3862.49	0.0076	0.6060	0.5
Test 12	20.0377	11.6923	0.0605	3934.01	0.0078	0.6004	0.55
Test 13	19.9251	11.5586	0.0616	4005.54	0.0080	0.5953	0.6
Test 14	19.8194	11.4327	0.0626	4070.57	0.0082	0.5906	0.65
Test 15	19.7195	11.3136	0.0636	4135.59	0.0084	0.5862	0.7
Test 16	19.6249	11.2005	0.0646	4200.62	0.0086	0.5821	0.75
Test 17	19.5349	11.0928	0.0655	4259.14	0.0087	0.5783	0.8
Test 18	19.4491	10.9900	0.0663	4311.16	0.0089	0.5747	0.85
Test 19	19.3671	10.8915	0.0672	4369.68	0.0091	0.5712	0.9
Test 20	19.2881	10.7966	0.0680	4421.70	0.0093	0.5680	0.95
Test 21	19.2271	10.7231	0.0686	4460.72	0.0094	0.5655	0.99

Table A14: The effect of the regularization parameter β using the PSF of support size 23×23, where $\alpha = 0.4$ and $\beta_{lat} = 0.1$ are fixed for the image "Bridge" and for the "photo" image $\alpha = 0.001$ and $\beta_{lat} = 0.4$, while β increase by a step size of 0.05

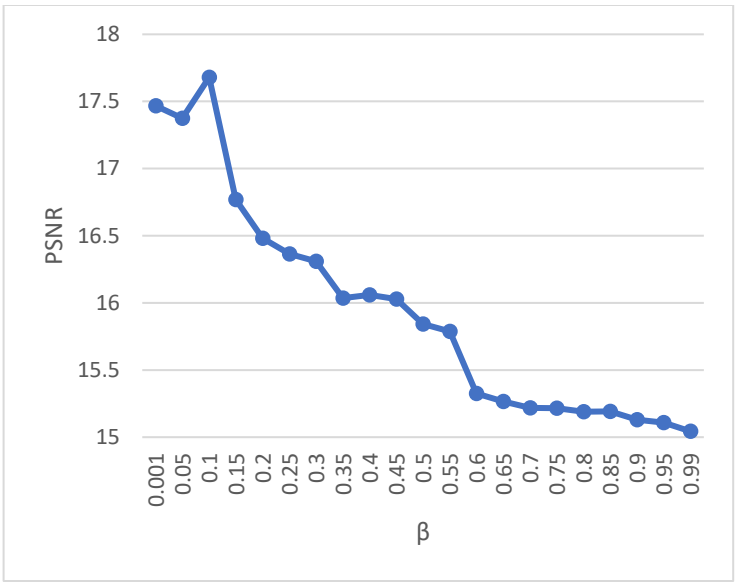

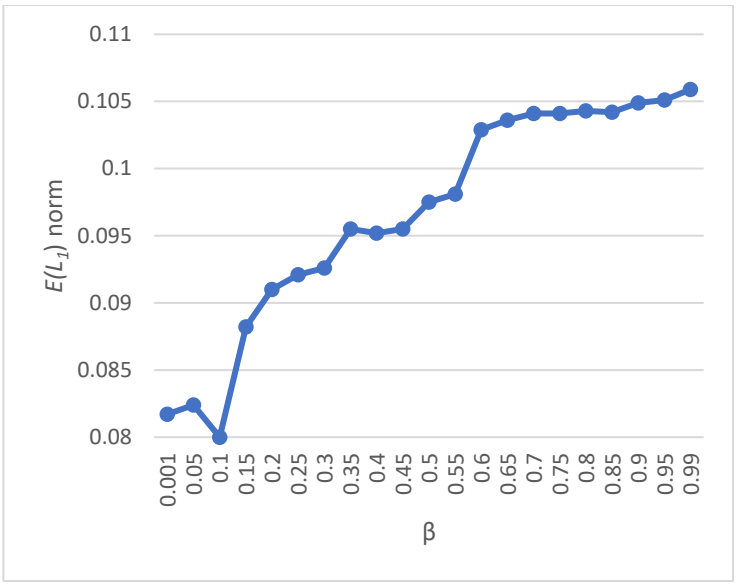

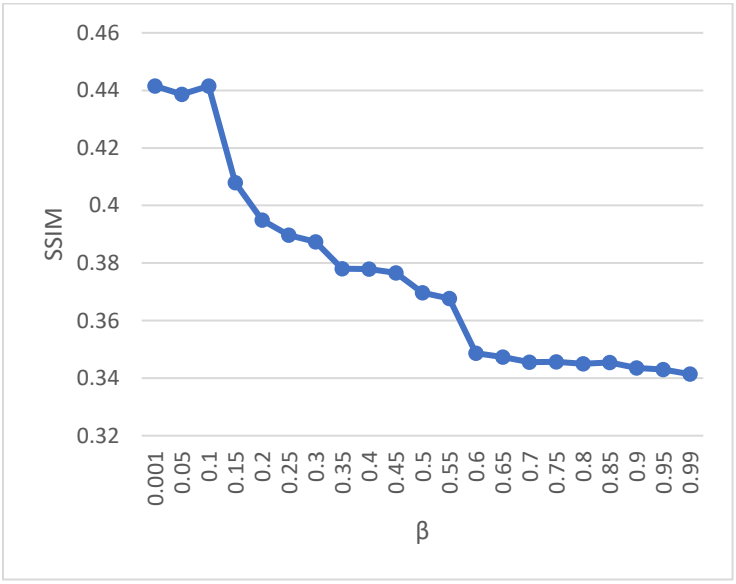

Figure A17: The effect of the regularization parameter β over the PSNR (top left), E(L_1) norm (Top right), and SSIM (middle) for the "Bridge" image using a PSF of support size 23x23 and fixing $\alpha = 0.4$ and $\beta_{lat} = 0.1$

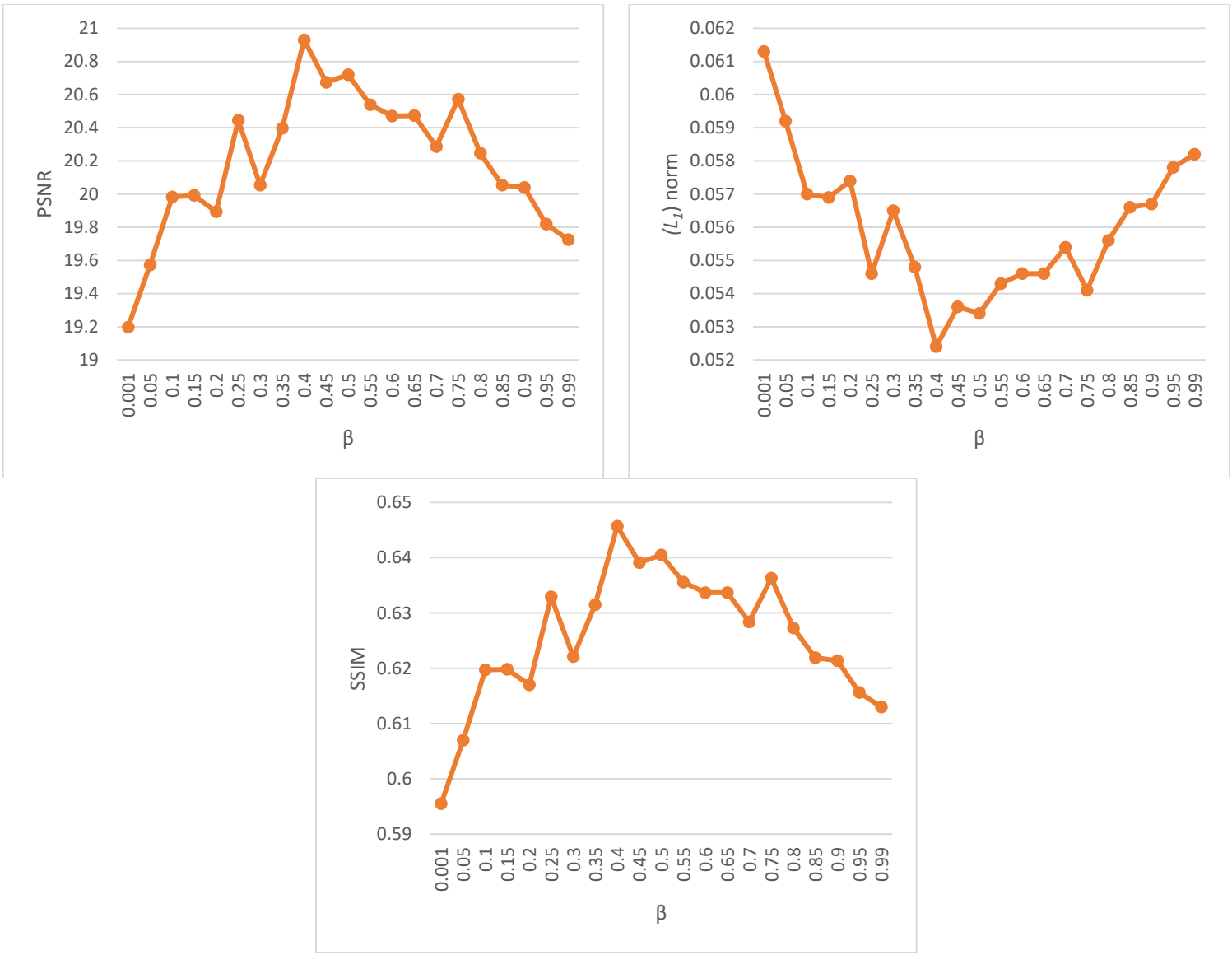

Figure A18: The effect of the regularization parameter β over the PSNR (top left), E(L_1) norm (Top right), and SSIM (middle) for the "Photo" image using a PSF of support size 23x23 and fixing $\alpha = 0.001$ and $\beta_{lat} = 0.4$

Titre : Restoration adaptative aveugle d'images monochrome et hyperspectrale

Mots clés : Restauration aveugle, estimation de paramètres de régularisation, PSF, imagerie hyperspectral, réglage automatique

Résumé : La restauration d'images représente un défi important lorsque les valeurs des paramètres de régularisation, la PSF et d'autres connaissances a priori ne sont pas disponibles. L'objectif de cette thèse est de développer une méthode de restauration facilement applicable en éliminant la nécessité d'informations préalables et d'un réglage empirique des paramètres. Pour atteindre cet objectif, nous avons développé une méthode adaptative de restauration d'images aveugle qui fonctionne sans nécessiter d'informations a priori. Cette méthode peut être appliquée pour restaurer des images monochromes, multispectrales et hyperspectrale, tout en optimisant les résultats de traitement sans nécessiter de réglage empirique des paramètres de régularisation. La supériorité de notre méthode de restauration aveugle adaptative est démontrée grâce à des évaluations sur diverses bases de données d'images, surpassant onze méthodes non-neuronales et neuronales supervisées/ semi-supervisées de l'état de l'art. En conclusion, la méthode proposée peut être facilement appliquée pour restaurer des images dégradées en raison de sa nature aveugle.

Title : Adaptive blind image restoration for monochrome and hyperspectral images

Key words : Blind restoration, regularization parameters estimation, PSF, hyperspectral image, automatic tuning.

Abstract: Image restoration presents a significant challenge when regularization parameter values, PSF, and other a priori knowledge are not available. The objective of this thesis is to develop an easily applicable restoration method by eliminating the necessity for prior information and empirical parameter tuning. To achieve this objective, we have developed an adaptive blind image restoration method that operates without requiring prior information. This method can be applied to restore monochrome, multispectral, and hyperspectral images, while optimizing restoration results without the need for empirical parameter tuning. The superiority of our proposed adaptive blind restoration method is demonstrated through evaluations on diverse image databases, outperforming eleven existing non-neural network and supervised/semi-supervised neural network methods from the state-of-the-art. In conclusion, the proposed method can be easily applied to restore degraded images due to its blind nature.